SIMULATION AND EXAMINATION OF DIRECTIONAL SOLIDIFICATION CHARACTERISTICS OF HYPER-EUTECTIC AL-38WT%CU ALLOYS

BY

TREVOR SAWATZKY

A Thesis Submitted to the Faculty of Graduate Studies
in Partial Fulfillment of the Requirements
for the Degree of

MASTERS OF SCIENCE

Department of Mechanical & Industrial Engineering
University of Manitoba
Winnipeg, Manitoba, Canada

THE UNIVERSITY OF MANITOBA

FACULTY OF GRADUATE STUDIES

*****

COPYRIGHT PERMISSION PAGE

Simulation and Examination of Directional Solidification Characteristics of Hyper-Eutectic Al-38WT%CU Alloys

BY

Trevor Sawatzky

A Thesis/Practicum submitted to the Faculty of Graduate Studies of The University of Manitoba in partial fulfillment of the requirements of the degree

of

Masters of Science

ACKNOWLEDGEMENTS

I would like to express my gratitude to Dr. J.R. Cahoon for providing me the opportunity to work on such an exciting and interesting topic of research, along with all the help and supervision he has provided over the course of this work. Warm thanks go out to Mr. John Van Dorp, Mr. Don Mardis, and Mr. Kim Majury for their technical assistance throughout this project. Special thanks go out to all the graduate students in the Metallurgy lab for their friendship and encouragement. I would also like to thank Dr. L. Shafai, of the University of Manitoba for allowing me to use his numerous resources. I would also like to thank my parents for their support throughout the years. Finally, I would like to thank Leili Shafai for her understanding, and sacrifice throughout this thesis project. Without her support, this thesis would not have been possible.

ABSTRACT

The present work deals with the solidification behavior of hyper-eutectic Al-38wt%Cu alloy. Various aspects of solidification in the Al-Cu system are studied. The formation of channel segregates or freckles during vertical solidification of Al-38wt%Cu alloy is simulated. The simulation is based on a mathematical model of dendritic solidification, in which the solid plus liquid zone is modeled as an anisotropic porous medium of variable porosity. The alloy solidifies from an initial melt and proceeds until the alloy is completely solidified. The final macrosegregation can be predicted.

A three zone gradient-freeze QUESTS (Queen's University Experiment on the Shuttle Transportation System) furnace was designed to carry out unidirectional solidification experiments. The experiments were carried out under different cooling conditions. The temperature gradients ranged from 1000 to 3500 (K/m) with a constant cooling rate of 3.5 (K/min), producing growth rates between 6 - 21 (cm/hr). The faceting behavior of primary Al_2Cu (θ) phase has been examined as a function of growth rate. The morphology of the Al_2Cu primaries showed a transition from non-faceted to faceted crystals with decreasing growth rate. The response in both appearance and location of freckles to changes in cooling conditions is in good agreement at low growth rates (6 cm/hr) only. The preference of channel formation on the outer surface and interior of the

casting is greater than that normally observed in hyper-eutectic Al-Cu alloys. It has been concluded that viscous stress due to natural convection disturbs the atoms, not allowing them to incorporate into crystals. The physical motion of nucleation sites into the bulk liquid due to natural convection may restrict channel growth and allow more θ phase to grow.

The segregation phenomena in the hyper-eutectic Al-Cu alloy was examined for both simulation and experiment. In both cases, severity of longitudinal segregation decreased with increasing growth rate. Simulated and experimental results were in agreement at low to intermediate growth rates, with the addition of lateral temperature gradients producing more accurate results on a local scale.

TABLE OF CONTENTS

LIST OF FIGURES

LIST OF TABLES

NOMENCLATURE

A_E	eutectic contraction coefficient
C_e	eutectic composition
C_l	liquid concentration
C_L	interdendritic solute concentration from the liquidus line in the phase diagram
C_{LE}	concentration of liquid eutectic at the eutectic temperature
C_0	initial alloy concentration
$\overline{C}$	average total concentration of solute
$\overline{C}_0$	mole fraction of solute
$\overline{C}_S$	local solute concentration in the solid
C_s	solid concentration
C_{SE}	concentration of primary dendrites at the eutectic temperature
C_t	solute concentration at the dendrite tips
C_∞	reference solute concentration (concentration in the liquid before solidification)
$\hat{c}$	specific heat capacity
Da_x, Da_z	Darcy number in the x and z direction, respectively
D_L	diffusion coefficient in the liquid
F_d	force acting on a dendrite arm due to fluid flow
f_l	volume fraction of liquid
f_e	volume fraction of eutectic phase
f_s	volume fraction of solid
g	acceleration due to gravity
g'	interface diffuseness
G	temperature gradient
G_0	normalized temperature gradient
G_L	applied temperature gradient

Gr	Grashof number
H	reference length
H_T	z-coordinate for the top of the container
I	nucleation rate
k	equilibrium distribution coefficient
k_B	Boltzmann's constant
k_{ef}	effective distribution coefficient
K	permeability
$K_{r,c}$	constants
L	system size, length
$\overline{L}$, $\hat{L}$	first and second non-dimensional latent heat, respectively
m	liquidus slope
M_{LE}	mass of liquid eutectic at the eutectic temperature
M_{SE}	mass of primary dendrites at the eutectic temperature
N_l	number of atoms in the liquid state
n	unit outward normal vector
P	pressure
Pr	Prandtl number
q	prescribed boundary heat flux
r	prescribed cooling rate
r	radius of cluster formation
r_f	radius of facet
r_{cap}	radius of a hemispherical cap
r^*	critical nucleation radius
R	rate of interface movement, solidification velocity
R'	radius of fully liquid region
R_a	Raleigh number
Ra_S, Ra_T	solutal and thermal Raleigh number, respectively
Sc	Schmidt number
t	time

t_f	local solidification time
T	temperature
T_f	melting temperature of pure solvent
T_i	initial temperature
T_l	liquidus temperature
T_m	equilibrium melting temperature
T_0	equilibrium temperature
T_R	reference temperature
u_L	x-component of the superficial velocity
U	reference velocity
V	interdendritic flow velocity
V^*	mean interdendritic flow velocity
w_L	z-component of the superficial velocity
z	coordinate perpendicular to a planar solid/liquid interface
α	thermal diffusivity
β	shrinkage factor
β_s	coefficient of solutal expansion
β_t	coefficient of thermal expansion
ΔG	total Gibbs free energy
ΔG_d	activation free energy for diffusion across a solid/liquid interface
ΔG_v	difference in free energy between liquid and solid phases
ΔH_f	heat of fusion
ΔS_m	entropy of fusion
ΔT	undercooling
ΔT^*	critical undercooling
ΔT_0	liquidus — solidus range at C_0
Δz	mushy zone height
δ_c	solute boundary layer thickness
ε	surface tension scalar factor
ϕ	volume fraction of interdendritic liquid

λ	spacing
λ_1	primary dendrite arm spacing
λ_2	secondary dendrite arm spacing
μ	viscosity
ν	kinematic viscosity
ν_0	atomic vibration frequency
ν_s	specific volume of solid
ν_{LE}	specific volume of liquid eutectic
ν_{SE}	specific volume of solid eutectic
θ	wetting angle
ρ	density
ρ_0	reference density
ρ_l	density of liquid
Σ	rate of temperature change
σ	solid/liquid interface energy
σ_c	stress acting on a cylinder
τ	reference time

CHAPTER I

INTRODUCTION

1.1 Background

The use of alloys is common practice in most foundry processes since alloy additions allow a significant increase in performance over pure metals. Grain refinement, a phenomena producing a fine equiaxed grain structure with characteristic high strength at low temperatures, is also attributed to alloy additions. A number of important factors influence the performance of as-cast alloys. Such factors include micro- and macro-segregation, diffusion of solute at the advancing solid/liquid interface, gravity-driven convective flow in the liquid, and cooling conditions of the casting process. These conditions incorporate such parameters as the imposed temperature gradient, cooling rate, and casting technique.

Natural convection and thermosolutal convection are consequences of local temperature differences and concentration and density differences set up at the solid/liquid interface due to rejection of solute into the liquid. These mechanisms can result in long range compositional inhomogeneities in the cast structure. Segregation effects resulting from these mechanisms play a large role in the casting industry since compositional variations throughout the cast, produce undesirable anisotropic properties, affecting performance. To remedy this situation, induced fluid motion by means of electromagnetic stirring, or cast agitation have been applied to induce convective currents in the molten liquid during solidification. Such fluid motion results in a stabilizing effect in terms of the solid/liquid interface advancement of dendritic arrays. In the presence of

strong convection, these forces may cause dendrite detachment in the mushy zone which will carry broken dendrite tips into the liquid providing more sites for nucleation and grain growth resulting in a more homogeneous cast structure.

1.2 Recent Advancements

Computer modeling has been used extensively in the casting industry to predict solidification defects due to geometrical considerations of the part being cast, with the emphasis on such aspects as castability and internal stress concentrations. Finite element algorithms have been more recently used to predict the morphology of cast structures, as well as segregation phenomena arising from thermosolutal convection. One such investigation performed by Felicelli [1] on Pb-Sn alloys was to determine the occurrence of channels and freckles in binary alloys, resulting from micro- and macro-segregation. More recently, tertiary alloys modeled in two dimensions [2], and three dimensions [3] have been carried out. The accuracy of such solidification models is under severe scrutiny since an accurate portrayal of fluid flow during solidification conditions is difficult to predict. Radioactive tracer material and transparent fluids have been used to observe actual fluid motion during solidification, but these methods, like numerical simulations, must be correlated with experiments of binary alloys.

To better understand the influence of convective effects as stand alone phenomena, convective forces due to buoyancy-driven forces can be minimized by performing solidification experiments in microgravity. One way in which this is possible is by performing microgravity experiments aboard a NASA KC-135 research aircraft.

This aircraft is capable of producing 20 second periods of microgravity conditions (0.01g) followed by approximately 90 seconds of 1.8g[4]. A 20 second limit, limits the amount of continuously solidified material that may be produced under such conditions. In order to maximize the amount of material, a growth rate must be determined by conducting numerical analyses and unit gravity experiments. This optimum growth rate is accompanied by a large change in longitudinal segregation at slight deviations from cooling conditions. A large amount of continuously solidified material coupled with a significant degree of segregation is desired. Once this has been determined, microgravity experiments will produce longer microgravity samples allowing a more accurate determination of the effect of gravity-free convection and fluid flow on the solid/liquid interface stability, and degree of segregation throughout a continuous cast structure.

1.3 Purpose/Scope

The main focus of this study was to gain a better understanding of how gravity-driven convective flow and thermosolutal convection, influence the microstructure and segregation during directional solidification in unit gravity. A further goal was to determine the most appropriate solidification conditions to obtain the maximum amount of information concerning the effect of the absence of gravity on solidification in a microgravity environment during future KC-135 flights or space station experiments. By comparing the size, distribution, and morphology of microstructures at different cooling conditions, it is hoped that the influence of gravity or the lack thereof on these mechanisms may be better understood.

In the present study, a three-zone gradient freeze furnace was used to carry out ground based, unidirectional solidification experiments. Al-38wt%Cu alloy was chosen for the study and numerical simulations of experimental conditions were performed to determine longitudinal segregation. From these simulations a critical growth velocity was determined where segregation remains significant.

The directional solidification experiments were performed at cooling conditions identical to numerical simulations. Longitudinal macrosegregation of the experimental samples were measured and compared with numerical results. The microstructure and morphology of the primary theta-phase resulting from equilibrium solidification conditions in hyper-eutectic Al-38wt%Cu alloys was compared on a qualitative level. These comparisons were used to determine the effects of varying process parameters during directional solidification of a two-phase alloy.

CHAPTER II

LITERATURE REVIEW

2.1 Solidification Process

The solidification process is an important function of many manufacturing industries. This process allows high viscous materials to be shaped at elevated temperatures where the material is molten and exhibits low viscosity. Once shaped, the processes require a phase transformation from liquid to solid. Advantages include near-net shape forming, reduced energy costs, improved as-cast properties, reduced waste from machining, and increased production. The underlying phenomenon of solidification as an atomic process has been documented over the last 50 years. Vast improvements in the understanding of this process have been achieved, allowing researchers to improve cast structures by reducing defects during the solidification process.

2.1.1 Nucleation and Thermodynamics of Solidification

In order for solidification to take place, the material in question must be raised above its liquidus temperature. In the liquid phase, the material is very non-viscous, and may be poured into a mold. To initiate solidification, heat extraction from the melt must

occur. By extracting heat from both the liquid phase and solid phase during solidification, there is a decrease in the enthalpy of the liquid or solid due to cooling, and there is a corresponding decrease in enthalpy due to the transformation from liquid to solid [5]

For a pure metal, solid can form when the liquid is cooled below its equilibrium temperature, due to the difference in free energy, ΔG_v, between the liquid and solid phase. The difference in free energy increases with degree of undercooling, ΔT, and is given by [6],

$$\Delta G_v = \frac{\Delta H_f}{T_m} \Delta T \tag{2.1}$$

where ΔH_f is the heat of fusion, and T_m is the equilibrium melting temperature.

Equilibrium conditions for alloys under similar solidification conditions are influenced by the presence of solute atoms in the melt. For alloys, when the criteria for equilibrium at T_l is satisfied (i.e. the free energy of the solid and liquid phases are equal), the composition of the phases are different. Equilibrium phase diagrams are used to determine these solutal differences. The Al-Cu alloy system is shown in Figure 2.1.

The non-equilibrium condition of undercooling allows nucleation to occur. Undercooling is required since atoms tend to leave rather than join clusters of solid spheres because of the small surface energy relative to the bulk liquid. Hence, the free energy, ΔG, associated with homogeneous nucleation is a function of the change in volume, as well as the coupling between the liquid/solid surface energy [5],

$$\Delta G = \frac{4\pi r^3}{3}\frac{\Delta T}{T_f}\Delta H_f + 4\pi r^2\sigma \qquad (2.2)$$

where r is the radius of cluster formation, T_f is the melting point of the pure solvent, and σ is the solid/liquid interface energy. The rate of formation of nuclei, I, may be found from,

$$I = I_0 \exp\left[\frac{\Delta G_d + \Delta G}{k_B T}\right] \qquad (2.3)$$

where ΔG_d is the free energy for diffusion, k_B is Boltzmann's constant, T is the temperature, and I_0 is a pre-exponential factor represented by,

$$I_0 = N_l \cdot \nu_0 \qquad (2.4)$$

where N_l is the number of atoms in the liquid state, and ν_0 is the atomic vibration frequency. According to equation 2.3, the nucleation rate is very sensitive to values within the exponential. In order for growth to take place, the nucleation rate must be larger than the cooling rate. A critical nucleus, r^*, is achieved when undercooling is great enough for cluster growth. This occurs when,

$$r^* = \frac{\sigma T_m}{\Delta T \Delta H_f} \qquad (2.5)$$

During heterogeneous nucleation, the formation of a nucleus of critical radius may

be catalyzed by a number of physical features such as; the surface of the mold wall, an impurity particle suspended in the bulk liquid, or the presence of an oxide film on the surface of the liquid. For homogeneous nucleation to occur, large undercoolings are required, of the order of 100 degrees, while heterogeneous nucleation requires very little undercooling due to the catalysts mentioned above. For heterogeneous nucleation, the surface energy of the embryo to the liquid must be considered. Thus the Gibbs free energy term in equation 2.3 becomes,

$$\Delta G = \frac{16\pi\sigma^3}{3\Delta G_v^2}\left[\frac{(2+\cos\theta)(1-\cos\theta)^2}{4}\right] \tag{2.6}$$

The corresponding nucleation rate in equation 2.3 becomes influenced by the wetting angle, θ, as well as the diffusion term.

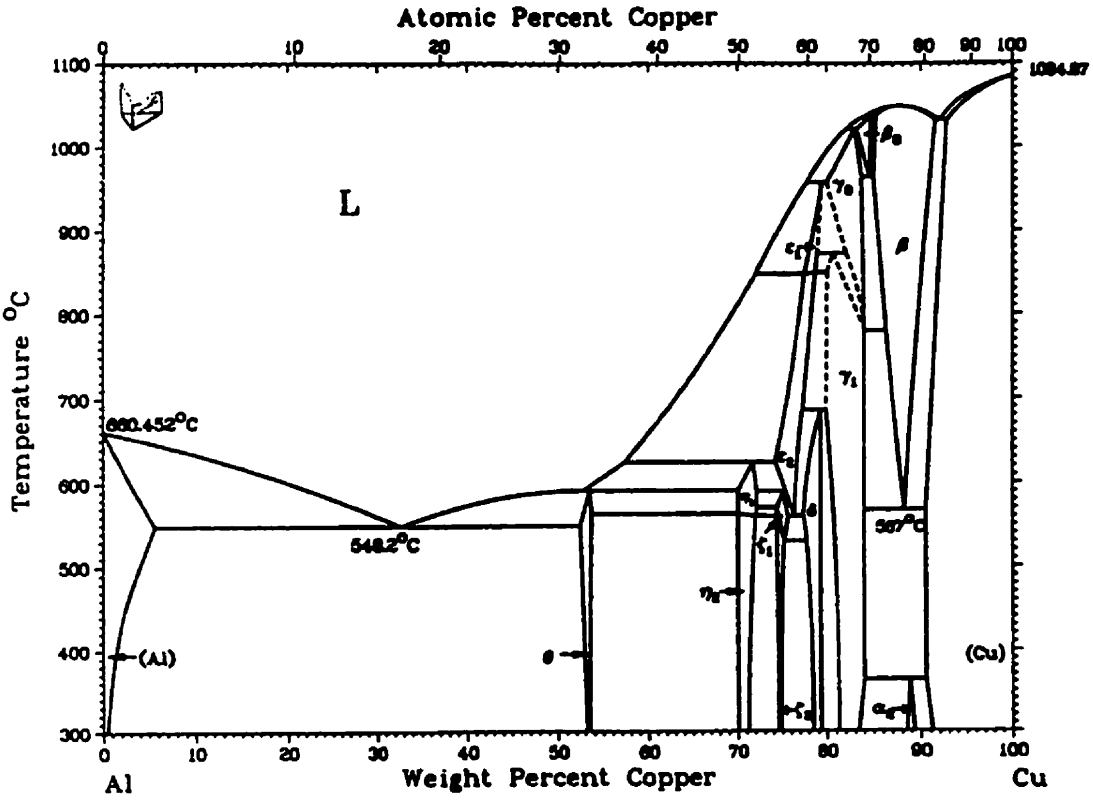

Figure 2.1 Al-Cu Phase Diagram [7]

2.1.2 Interface Stability / Heat Flow Considerations

2.1.2.1 Constitutional Supercooling Criterion

The stability or instability of a moving solid/liquid interface depends highly on the solute-rich boundary layer that builds up in front of the solidifying interface, as well as the direction of heat flow. Figure 2.2 shows a solute rich layer built up in front of a growing interface, with the liquid composition being a maximum at C_0/k. The composition in front of the interface decreases with increasing distance and is given by,

$$C(x) = C_0 + \left(\frac{C_0}{k} - C_0\right)e^{-Rz/D_L} \tag{2.7}$$

where C_0 is the initial alloy concentration, k is the equilibrium distribution coefficient, R is the rate of interface movement, z is the distance in front of the interface, and D_L is the diffusion coefficient in the liquid. The corresponding thickness of the solute rich layer, δ_c, may be taken as the equivalent boundary layer given by,

$$\delta_c = \frac{2D_L}{R} \tag{2.8}$$

As the interface advances, solute is rejected if the solubility of the solute in the solid is lower than that in the liquid. After a significant period of time, the concentration distribution becomes time dependent. In general, the rate of rejection of solute is

proportional to the growth rate, and as indicated in Figure 2.2. As the growth rate increases, the boundary layer becomes less prominent. The rejected solute must be transferred away from the interface, producing a steeper concentration gradient leading to phenomena such as segregation.

For alloys, the change in concentration gradient ahead of the interface will affect the liquidus temperature, T_l , in the following manner [5],

$$T_o - T_l = m(C_o - C_l) \tag{2.9}$$

where T_0 is the equilibrium temperature, m is the liquidus slope, and C_l is the liquid concentration. Figure 2.3 represents a solute boundary build-up, and shows how constitutional supercooling determines interface stability. The liquidus temperature increases with increasing distance from the interface as indicated by equation 2.9. This temperature profile represents the local equilibrium temperature for solidification. The applied temperature gradient, G_L, causes a heat flux at varying volume elements in front of the interface, and the corresponding temperature, T_q, must also be determined and compared with the equilibrium temperature. T_q must be less than T_s at the solid/liquid interface to drive solidification. If the gradient of T_q is less than the gradient of T_l, an undercooled region will occur, leading to perturbations on the solid/liquid interface as shown in Figure 2.3 (d). Therefore, for alloys, the interface is constitutionally supercooled when [5],

$$\frac{G_L}{R} \leq \frac{m\, C_0(1-k)}{k D_L} \tag{2.10}$$

Higher temperature gradients given by equation 2.10 result in a planar interface, while lower temperature gradients result in a perturbed interface. Stable, plane front solidification occurs when the interface is exactly at the equilibrium liquidus temperature, and where every point ahead of the interface is at a temperature above the liquidus temperature.

Upon the introduction of a perturbation at the solid/liquid interface, the local temperature gradient in the melt increases. For alloys, the local concentration gradient will subsequently become steeper and therefore the liquidus temperature gradient will increase. All these factors help preserve the supercooling criterion.

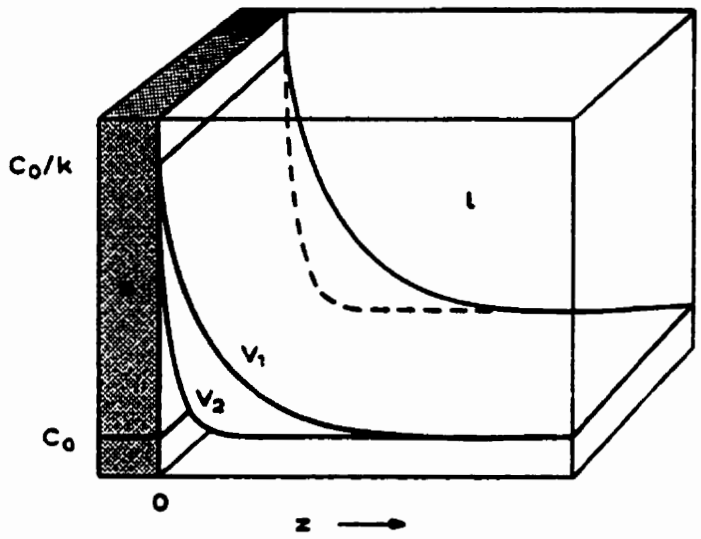

Figure 2.2 Steady-State Boundary Layer at a Planar Solid/Liquid Interface [5]

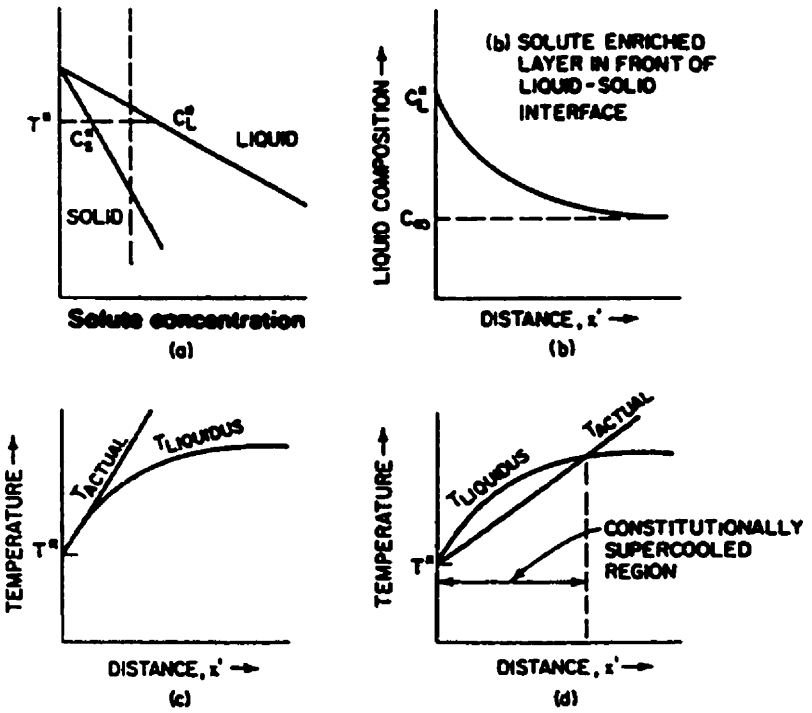

Figure 2.3 Constitutional Supercooling in alloy solidification. (a) Phase Diagram, (b) solute-enriched layer in front of liquid-solid interface, (c) stable interface, (d) unstable interface. [8]

2.2 Solidification Growth Morphologies

2.2.1 Dendritic Growth

The formation of dendritic crystals during directional solidification of alloys is a common occurrence. For aligned dendritic growth to occur, the heat flow out of the melt and the corresponding isotherms must be constrained in a single direction. This allows dendritic trunks to grow in the opposite direction to heat flow. When heat flows from the crystal to the melt, the dendrites may grow as quickly as the imposed undercooling permits. This morphology is known as equiaxed dendritic. The cellular to dendritic transition occurs when the growth rate of the solid/liquid interface increases, and cellular formation leads to the appearance of side branching as is indicated in Figure 2.4. Cells first form when a planar solid/liquid interface initially breaks down due to such causes as grain boundaries, impurities, or a fluctuation in growth rate. As the rate of dendritic growth increases, crystallographic limitations influence the direction of growth along a specific crystallographic direction, while cellular growth is controlled solely by the direction of heat removal.

A number of theories to describe dendritic growth have been developed to yield growth velocity/ supercooling relationships in an attempt to predict dendrite morphology. Most theories differ in dendrite geometry assumptions. For example, Kurz and Fisher [5] use a hemispherical cap to represent the tip of a growing dendrite, leading to the

following relationship,

$$r_{cap}^2 R = \frac{4\pi^2 D_L \sigma}{\Delta T_0 k \Delta S_m} \qquad (2.11)$$

where r_{cap} is the radius of the hemispherical cap, ΔT_0 is the liquidus - solidus range at C_0, and ΔS_m is the entropy of fusion. Other theories proposed by Horvay and Cahn [9] use a parabolic dendrite tip with elliptical cross section. Nash and Glicksman [10] developed a non-linear analysis which eliminated the need for a defined geometry since the flux conditions and capillarity were applied to every point on the face yielding a non-constrained dendrite shape as part of the solution. Approximations made by these theories neglect the overlapping of diffusion fields around closely spaced dendrites during growth. More recent developments have been made by Hunt & Lu [11], who used numerical simulations to predict cell and dendrite spacings, undercoolings, and the transition between structures, given specific cooling conditions. Predictions were compared with experimental results, indicating good agreement, although spacing predictions at high Peclet values indicate deviations from experiment.

Dendrite arm spacings control mechanical properties of cast structures. Generally speaking, fine dendritic structures produce superior properties in terms of tensile strength and ductility [12]. Unsteady-state heat flow predictions are important since most industrial solidification processes occur in this manner. A number of equations have been proposed to relate dendrite spacings to growth conditions. Kurz and Fisher [5] proposed

that the primary dendrite spacing, λ_1 be given by,

$$\lambda_1 = \frac{4.3(\Delta T_0 D_L \sigma)^{0.25}}{k^{0.25} R^{0.25} G^{0.5} \Delta S_m^{0.25}} \tag{2.12}$$

indicating that a change in temperature gradient, G, has a greater effect on primary spacing, than a change in growth rate, R. This result has been recently modified by Bouchard & Kirkaldy [13] who proposed a change in primary spacing after formation (ripening), leading to the relation,

$$\lambda_1 = 120\left[\frac{16\overline{C}_0^{1/2} G_0 \varepsilon \sigma T_m D_L}{(1-k)m\Delta H_f GR}\right]^{1/2} \tag{2.13}$$

where G_0 is a normalized temperature gradient with a value of 600 K/cm, ε is a surface tension scalar value equal to 6, and $\overline{C}_0$ is the mole fraction of solute. The primary spacing is now equally dependent upon growth velocity and temperature gradient, yielding a better approximation to unsteady-state heat flow conditions.

Secondary dendrite arm spacings are also an important parameter in dendritic growth, since they reflect local solidification conditions. Kattamis and Flemings [14] proposed that the secondary dendrite spacing, λ_2, is given by

$$\lambda_2 = 5.5(Mt_f)^{1/3} \tag{2.14}$$

where M is given by,

$$M = \frac{\sigma D_L \ln\left(\frac{1}{k}\right) T_f}{\Delta H_f m(1-k)(C_0 - C_e)} \tag{2.15}$$

and t_f is the local solidification time, and C_e is the eutectic composition. Bouchard and Kirkaldy [13] confirmed that equation 2.14 provided accurate measurements of secondary dendrite spacings for a number of materials, and therefore, in calibrated form similar to equation 2.13, the equation becomes,

$$\lambda_2 = 12\pi \left[\frac{4\sigma D_L^2}{(1-k)^2 \Delta H_f C_0 R^2} \right]^{1/3} \tag{2.16}$$

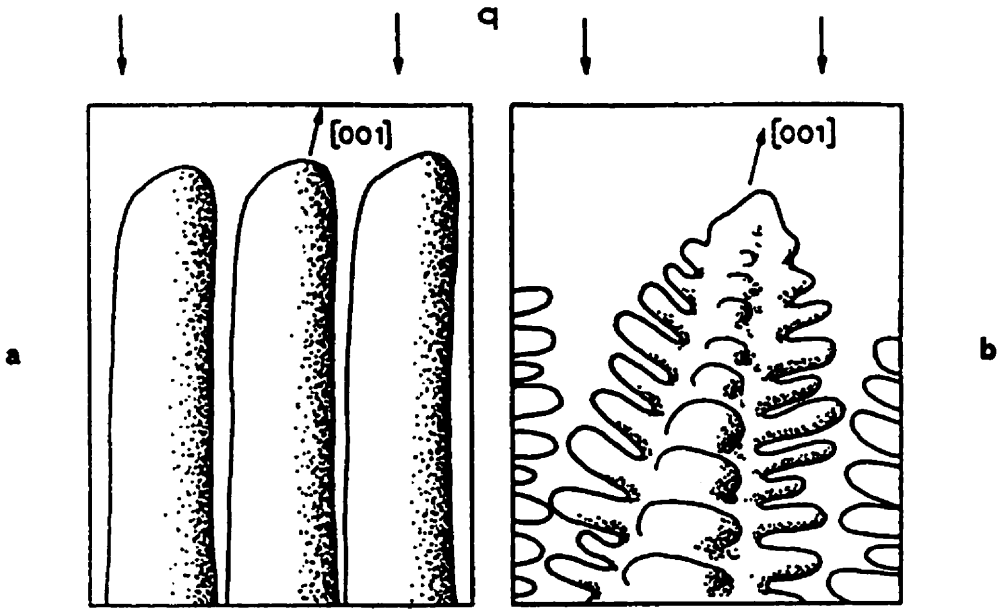

Figure 2.4 Morphology and growth direction of, (a) Cells, and (b) Dendrites. [5]

2.2.2 Faceted Growth

The growth rate of a crystal is determined by three main factors, specifically; the kinetics of atom attachment to the interface, capillarity effects, and the diffusion of heat and mass. Faceted growth occurs by the formation and spreading of lateral planes. High index planes accept atoms readily and therefore grow quickly, as opposed to the slow growth of low-index planes. The high index planes will disappear leaving the growth of the crystal bounded by the low-index planes.

Faceted structures are usually formed in materials with a high entropy of fusion, or in the case of alloys, with high entropies of solution. This is a consequence of the difference in structure and bonding between the solid and liquid phases. The large difference in structure restricts bonding to the solid, and therefore growth is more difficult, and requires additional kinetic undercooling. Facet formation is also influenced by crystallography, interface temperature, melt composition, and impurity absorption. The major dendrite direction for faceted materials is generally the axis of a pyramid whose sides are the most closely packed planes (i.e. (111) for BCC, FCC, and (0001) for hexagonal), as in Figure 2.5. Growth directions may be influenced by overlapping diffusion fields or by modest fluid flow. In directional solidification, the most favorable direction for growth is the preferred dendrite direction for two reasons; (1) high tip temperatures encourage main stem growth over side branches, (2) the preferred growth

direction provides the most favorable path for heat extraction through the mushy zone.

If we assume a cubic crystal is growing in an undercooled melt, then the crystal is dissipating heat into the melt. Due to the geometry of the crystal, heat diffuses more readily at the corners than near the center of the crystal. Steps will occur at the corners more readily with a constant velocity, which decreases as the local undercooling decreases. Figure 2.6 indicates the growth of such a facet.

A faceted crystal represents a stabilized interface that deters the breakdown of an advancing interface. A relation for the stability criterion of a growing facet has been proposed by Keith, and Padden [15], such that,

$$\frac{Rr_f}{D_L} \leq \frac{\Delta T}{mC_0(1-k)} \tag{2.17}$$

where r_f is the approximate radius of the facet. Under such conditions, large amounts of undercooling are required to breakdown the interface. Also, a small facet radius indicates a stable interface, but as the relation approaches unity, we expect the corner effect to occur resulting in faceted dendrites.

In order to predict the morphology of metallic systems which are prone to both faceted and non-faceted morphologies, Jackson [16], proposed the following relation based on entropy of fusion values.

$$\alpha = \frac{\Delta S_m}{R} \tag{2.18}$$

Values of $\alpha<2$ indicate a trend toward non-faceted (dendritic) growth, since such values represent less than half of the possible sites being filled, resulting in the growth of high index planes. For $\alpha>2$, a move toward faceted growth occurs since most sites are filled, restricting growth to low-index planes. Jackson s analysis was based on a number of assumptions restricting the analysis to equilibrium conditions at the solid/liquid interface using a nearest neighbor bond model at the eutectic temperature. Cahn [17] extended Jackson's analysis by considering the steady state distribution of all possible interface configurations. Results suggest that temperature as well as the dependence of α on the interface orientation influence the facet to non-facet transition. Cahn's calculation of a critical undercooling for facet / non-facet transition is,

$$\Delta T^{*} = \frac{\pi g' T_0}{\sigma \Delta H_f} \tag{2.19}$$

where g' is the interface diffuseness. Equation 2.19 suggests that all metals facet at small undercoolings. Temkin [18] expanded this model to include multiple atomic layers and found that materials with $\alpha<2$ have much smoother interfaces than materials with $\alpha>2$. Camel et al. [19] developed a model that incorporates the effect of temperature, bulk chemical interactions, and interfacial absorption. His model predicted that Al_2Cu facets grow when present in a Cu-rich liquid, but has non-faceted growth at the eutectic composition. This structural transition highly depends on the volume fraction along with

the kinetic undercooling as shown in Figure 2.7. When the driving force is small, dislocation steps, such as screw dislocations, or twin plane re-entrant edges (TPRE) as shown in Figure 2.8, may aid growth.

Al-Cu alloys may exhibit many different microstructures depending on; the growth mechanisms of the phases, the temperature gradient in the liquid, alloy composition, and degree of convection in the melt. Faceting only occurs when the interface curvature of the facet phase is convex with respect to the solid, and when the interface is tangent to the faceting phase [6]. Macrofacets may form parallel to the interface when growth exhibits a non faceted / non faceted morphology extending out several spacings. When large volume fraction of primary phase is present, growth restrictions due to faceting lead to the formation of a compositional boundary layer ahead of the solid/liquid interface. With further reduction in the faceting phase, cells will not form, and the alloy will grow in a non-faceted morphology.

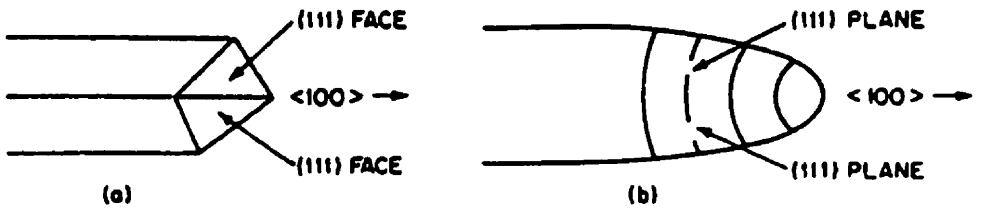

Figure 2.5 Schematic diagram of dendrite tip for growth of cubic materials in the <100> direction. (a) Faceted, (b) Non-Faceted. [8]

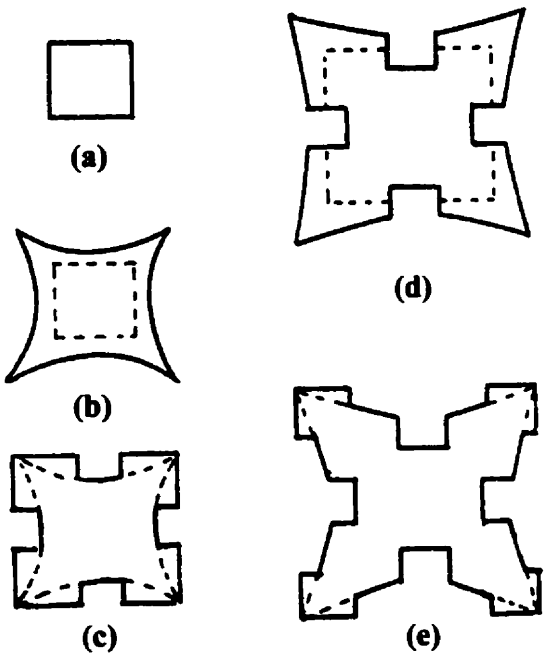

Figure 2.6 Schematic representation of the growth of a faceted dendrite [6].

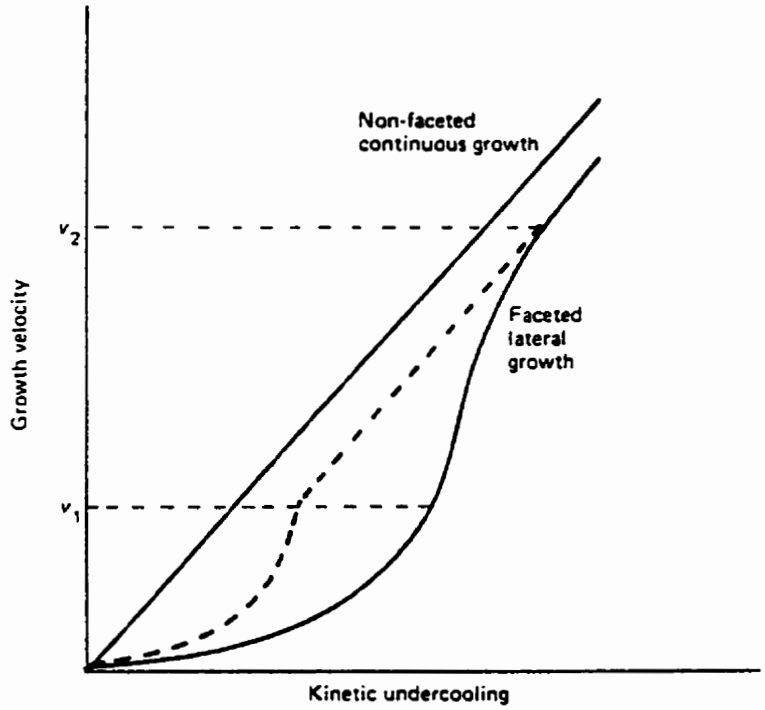

Figure 2.7 The variation of growth velocity with undercooling for continuous growth (non-facet material) and lateral growth (facet material). [6].

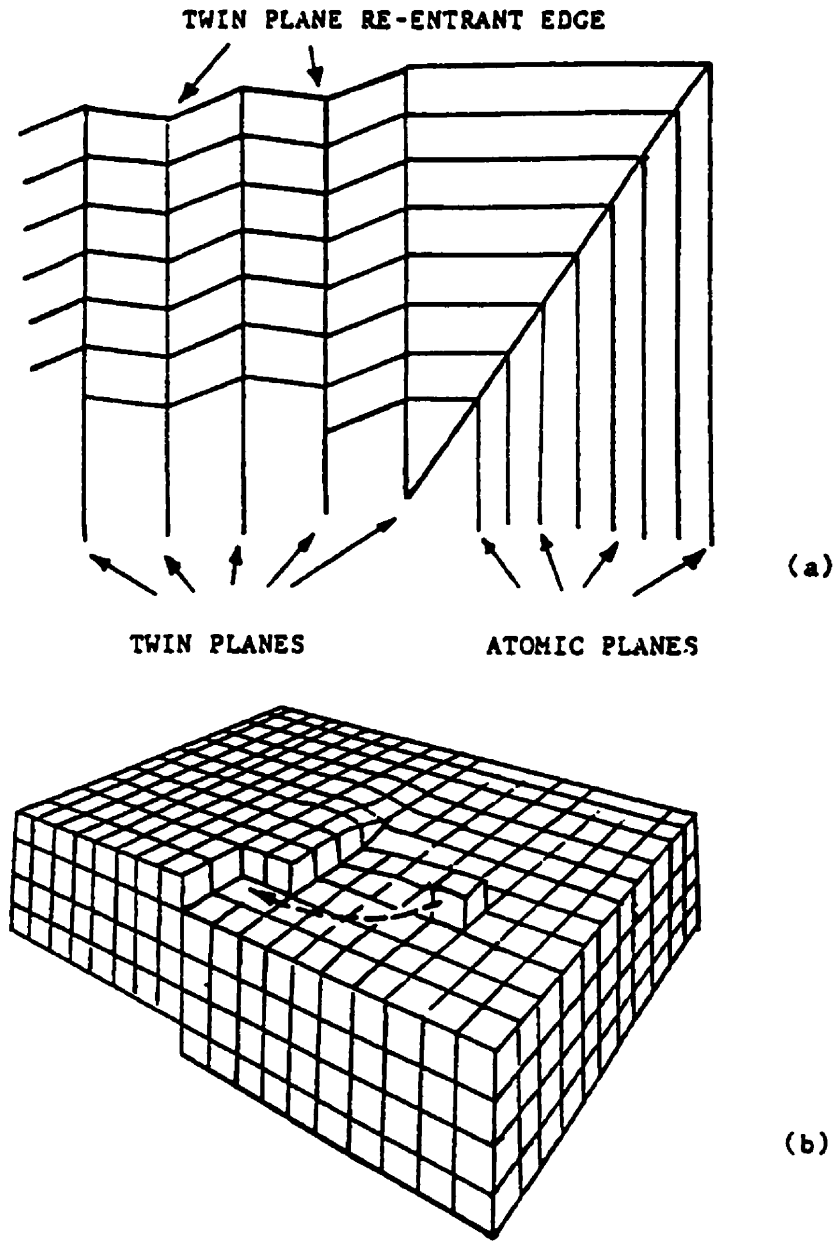

Figure 2.8 The presence of defect structure increases the mobility of a faceted plane by energetically favoring the deposition of atoms at the defect sites; (a) twin plane re-entrant edges; (b) screw dislocation. [4].

2.3 Eutectic Solidification

Eutectic solidification occurs when two or more phases grow simultaneously from a bulk liquid. To classify eutectic microstructures, one must analyze such factors as the solidification conditions, and the volume fraction of phases present.

2.3.1 Regular Eutectics

Regular eutectic solidification occurs in alloys where both phases have low entropy of fusion, such as in most metallic systems. The volume fraction may also play a role in the final morphology, since alloys with volume fractions ranging between 0 and 21% produce fibrous structures while compositions between 28% and 50% produce lamellar structures. Regular eutectics are therefore associated with non-faceting alloy systems.

For lamellar eutectics, the same lamellar structure may exist for several centimeters with a predictable orientation in relation to each phase. This orientation exists since eutectic alloys exhibit small interphase spacings on the order of one tenth the size of dendrite trunks. A large total interfacial energy exists between phases. To minimize this energy, certain crystallographic relations develop.

If we consider an alloy of exact eutectic composition growing with a plane front

and slightly curved lamellae. When the α phase grows, it rejects B atoms into the liquid. Also, the growing β phase will reject A atoms into the liquid. A lateral diffusion gradient transfers the atoms across the interface to sustain growth of the other phase. As a consequence, this lateral diffusion field decreases the long range solute buildup in front of the interface.

Jackson and Hunt [20] provided a quantitative treatment of regular eutectic growth by considering the steady-state directional growth equation.

$$\nabla^2 C_l + \frac{R}{D_L}\frac{\partial C_l}{\partial z} = 0 \tag{2.20}$$

From equation 2.20, they derived the following relationships for the total solid/liquid interface undercooling,

$$\frac{\Delta T}{\sqrt{R}} = 2(K_r K_c)^{1/2} \tag{2.21}$$

where K_r and K_c are constants dependent on the alloy system. This result allows quantitative microstructural determination based on growth conditions and undercooling.

2.3.2 Irregular Eutectics

Irregular eutectics are characterized by random orientations of primary phase with respect to the growth direction. Irregular growth occurs when $\alpha > 2$ for the primary phase (faceting), and usually occurs under low growth rate conditions with hyper-eutectic compositions. This is due to an increase the local concentration gradient of the faceting phase, ahead of the interface which promote cell formation [6].

The average lamellar spacing of irregular eutectics is much larger than regular eutectics because the anisotropic growth of the faceting phase is much more restricted to crystallographic directions. Any change in growth direction, or a branching of the phase, will be accompanied by large undercooling at the interface causing instability. The branching mechanism in Figure 2.9 is due to depressions at the solid/liquid interface, which become non-isothermal in character.

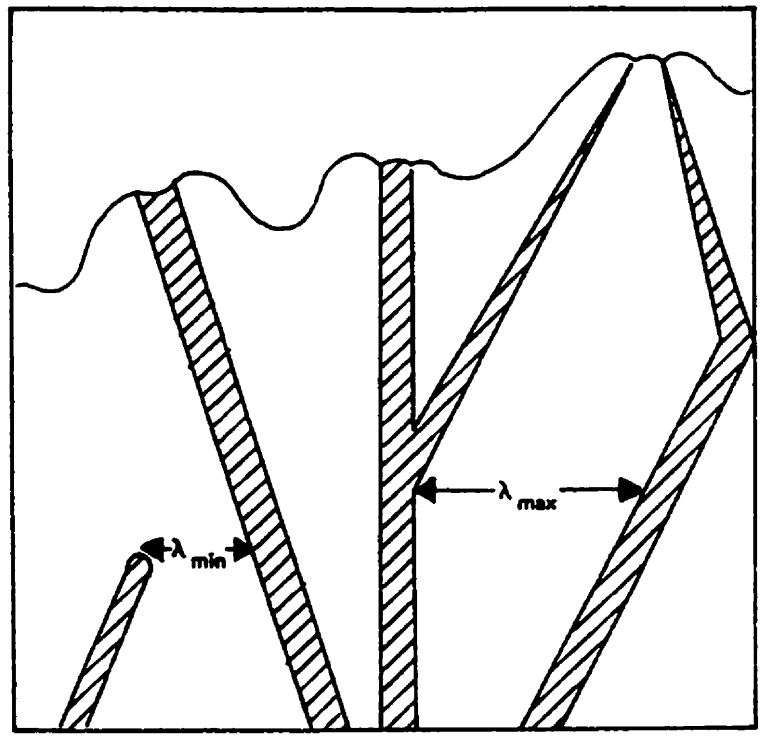

Figure 2.9 A schematic diagram of the growth of an irregular flake structure showing λ_{min} and λ_{max} corresponding to branching. [6].

2.4 Segregation

During the solidification of binary alloys, the solid composition that forms, C_s, is related to the liquid composition by the equilibrium distribution coefficient in the following manner,

$$C_s = kC_l \tag{2.22}$$

and is a characteristic of the alloy system in question. The equilibrium distribution coefficient, k, is determined from the phase diagram of an alloy, and is illustrated in Figure 2.10. This relationship will lead to compositional variations in solidified alloys known as segregation, as well as the appearance of different growth morphologies which depend on the solute distribution in the liquid ahead of the solid/liquid interface, diffusion processes in the solid and liquid, and convection in the liquid.

Quantitative analysis of segregation is determined on two distance scales. Microsegregation refers to the concentration differences over small scale distances such as cells, dendrites, and precipitates. Macrosegregation refers to compositional variations over distances equivalent to the cast limits. Microsegregation is mainly a consequence of solute diffusion in the solid and liquid, while macrosegregation is a result of flow in the interdendritic liquid leading to mass transport over large distances.

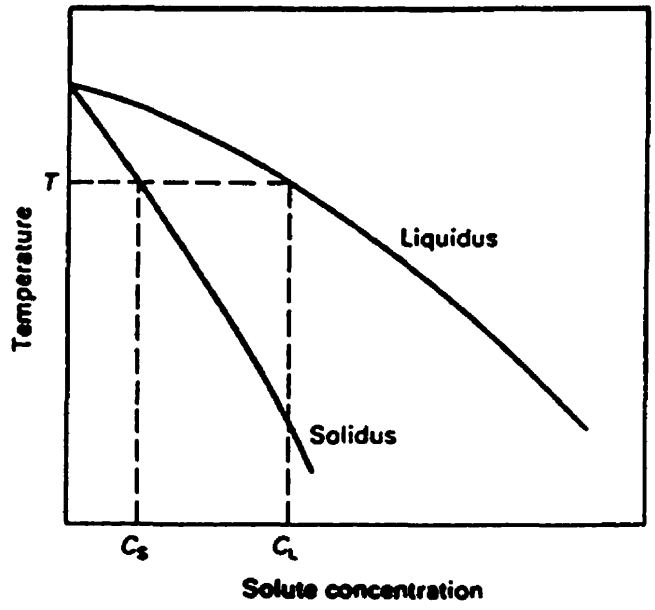

Figure 2.10 Hypo-eutectic region of an equilibrium phase diagram. [21].

2.4.1 Microsegregation

In order to predict microsegregation in alloy systems, a local solute redistribution equation was developed by Bower, Brody, and Flemings [22]. Figure 2.11 depicts a volume element representing the protrusion of cells into the bulk liquid, where the intercellular liquid becomes increasingly enriched in solute with distance from the cell tips. By determining the overall mass balance for solute in the volume element, and assuming solute flow is by diffusion only, along with equal solid and liquid densities, the solute

redistribution equation is,

$$C_s = kC_0\left[\frac{a}{k-1} + \left(1-\frac{ak}{k-1}\right)(1-f_s)^{(k-1)}\right] \tag{2.23}$$

where f_s is the volume fraction of solid, and a is given by,

$$a = \frac{D_L t_f}{L^2} \quad , \tag{2.24}$$

where L is the system size. Figure 2.12 shows microsegregation results for an Al-4.5wt%Cu alloy when equation 2.24 is varied.

By ignoring the a parameter at low thermal gradients, and assuming complete mixing, equation 2.23 reduces to the Scheil equation,

$$C_s^* = kC_0(1-f_s)^{k-1} \tag{2.25}$$

with the assumptions that the partition coefficient, k, is constant, the composition of the liquid is uniform in the volume element, and that diffusion in the solid is negligible [23].

For systems in which a eutectic phase may form, equation 2.25 may be used to predict the volume fraction of eutectic phase, f_e, present by,

$$f_e = \left(\frac{C_e}{C_0}\right)^{\frac{1}{k-1}} \tag{2.26}$$

The maximum composition corresponds to kC_e. Therefore, once this composition is

reached, the remaining intercellular liquid will solidify with a eutectic composition. Such results have been obtained for Al-Cu alloys with very small fractions of second phase in the initial alloy [23].

Since the original Brody-Flemings model did not conserve solute at high "a" values, a modified back diffusion parameter, a', was proposed by Clyne and Kurz [24] to take into account the back diffusion during solidification shrinkage, assuming the interface morphology is a parabolic function of time. The modified a' parameter is,

$$a' = a\left[1 - \exp\left(-\frac{1}{a}\right)\right] - 0.5\exp\left(-\frac{1}{2a}\right) \tag{2.27}$$

and,

$$C_s^* = kC_0(1-uf_s)^{-p/u} \tag{2.28}$$

where;

$$u = 1 - 2\,a\,k\ , \qquad p = 1 - k\ , \qquad C_s = k\,C_l$$

Modified a' parameters range from 0 to 0.5, and equation 2.28 cannot readily predict the final solute distribution profile in the solid because it changes with time when $a>0$. Therefore only the end concentration ($f_s = 1$) represents a measurable value. Kobayashi [25] developed an exact analytical solution to microsegregation problems, resulting in accurate numerical calculations of the solidification microstructure of cast alloys. (see appendix A)

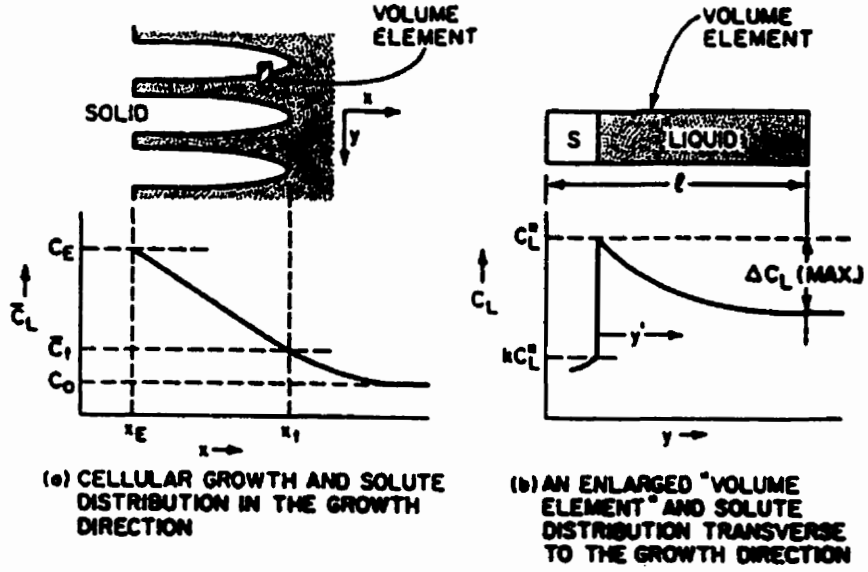

Figure 2.11 Solute redistribution in cellular growth. [8]

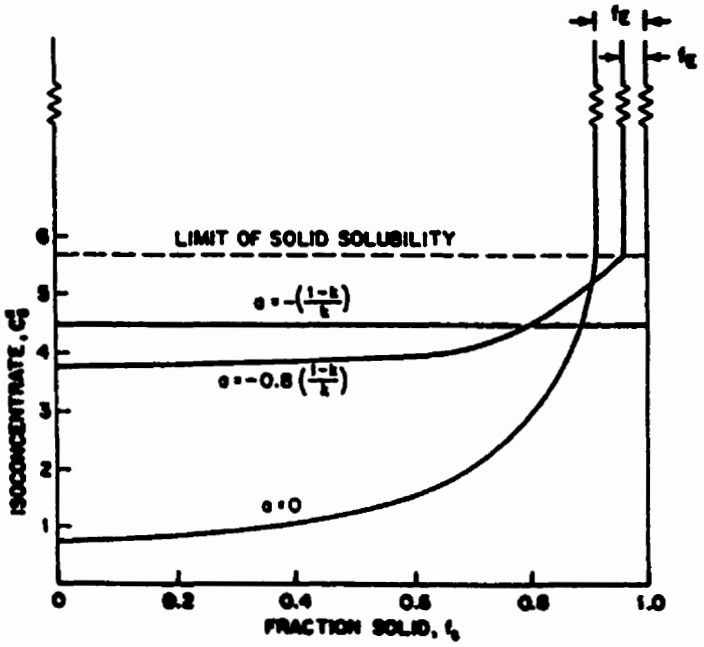

Figure 2.12 Microsegregation in cellular solidification. Plot represents microsegregation for an Al-4.5%Cu alloy. [8]

2.4.2 Macrosegregation

Mass movement of enriched liquid within the mushy zone causes long-range segregation. The mechanisms that drive this movement are [26];

1. solidification contraction;
2. effect of gravity on density differences caused by phase or compositional

changes;

3. external, centrifugal, or electromagnetic forces;

4. formation of gas bubbles;

5. deformation of solid phase due to thermal stress and static pressure;

6. capillary force;

Various types of macrosegregation results have been determined in the literature, yielding a number of quantitative factions of macrosegregation phenomena; namely, normal segregation, inverse segregation, gravity segregation and channel formation.

2.4.2.1 Normal Segregation

Normal segregation is determined by motion of solute parallel to the direction of solidification. The average concentration across an entire cross-section of sample in successive positions is used to determine normal segregation, which results in a single curve relating the distance from the start of solidification, to the concentration of solute, as shown in Figure 2.13. The degree of normal segregation determined from these curves depends on the equilibrium distribution coefficient, k, the rate of solidification, R, the amount of mixing by fluid motion, and the geometry of the cast.

During plane front solidification, the initially solidified portion has an approximate composition kC_o, which increases with time due to diffusion as the solute advances. The degree of normal segregation may be described by [26],

$$C_s = k_{ef} C_o (1 - f_s)^{(k_{ef}-1)} \tag{2.29}$$

where k_{ef} is the effective distribution coefficient given by,

$$k_{ef} = \frac{C_s}{C_o} = \frac{k}{k + (1-k)\exp[-R\delta_c / D_L]} \tag{2.30}$$

From equation 2.30, the degree of normal segregation increases with decreasing growth rate, R, and increases with decreasing boundary layer thickness δ_c. In turn, the boundary layer thickness is dependent on the liquid flow, where as flow intensity increases, boundary layer thickness decreases.

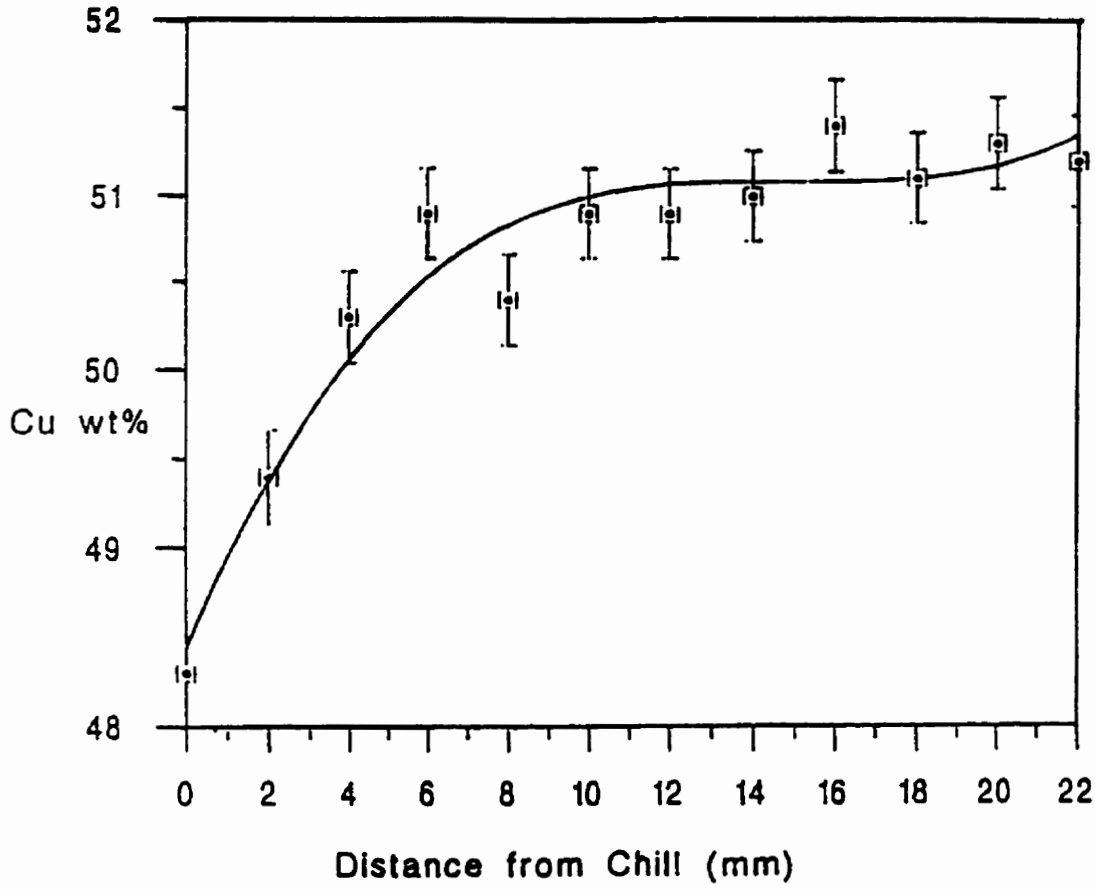

Figure 2.13 Macrosegregation of an Al-50%Cu sample [4].

2.4.2.2 Inverse Segregation

Inverse segregation is caused by the motion of solute enriched liquid in a direction opposite to the movement of the solidification front. This phenomena results from solidification shrinkage and surface exudation. Inverse segregation produces solidification curves where a high concentration of solute is present in regions that solidified earlier rather than later.

Inverse segregation at the chill face was initially developed by Schiel [27] for unidirectional solidified ingots. The theory was further extended by Kirkaldy and Youdelis [28] to include segregation along the length of the ingot, and further extended by Flemings et al [29, 30, 31] to include macrosegregation in ingots solidified with bi-directional heat flow and with non-uniform cross sections. More recent developments have been made by Cahoon [32], to concentration gradient influence in front of the advancing solid/liquid interface, along with numerical simulations by Reddy and Beckermann [33], and Chang and Stephansen [34] to model the influence of shrinkage on resulting convective flow fields. The original Schiel equation used to calculate chill face inverse segregation is [32],

$$\Delta C = \frac{(M_{LE}C_{LE}/A_E) + M_{SE}C_{SE}}{(M_{LE}/A_E) + M_{SE}} - C_0 \qquad (2.31)$$

where M_{SE} is the mass of solute in the primary dendrites, M_{LE} is the mass of liquid eutectic at the eutectic temperature, C_{SE} is the concentration of primary dendrites at the eutectic temperature, C_{LE} is the concentration of liquid eutectic at the eutectic temperature, and A_E is a eutectic contraction coefficient defined as,

$$A_E = \frac{v_{SE}}{v_{LE}} \tag{2.32}$$

where v_{SE} is the specific volume of the solid eutectic and v_{LE} is the specific volume of the liquid eutectic.

Cahoon re-evaluated inverse segregation theory with updated phase diagram data for the Al-Cu system, and specific volume information to conclude that predicted values of chill-face segregation are considerably higher than previous experimental results. By assuming a concentration gradient present in the liquid at the solid/liquid interface of the form,

$$\left.\frac{dC_l}{dz}\right|_{z=0} = \frac{R}{D_L} C_0 \left(\frac{1-k}{k}\right) \tag{2.33}$$

and substituting the equilibrium distribution coefficient with the effective distribution coefficient, experimental and theoretical values agree to a greater extent.

Recent numerical studies have been employed to determine the effect of solidification contraction on inverse segregation using numerical methods. Chang and Stephanescu [34] proposed a two-dimensional model for inverse segregation. They assumed the interdendritic liquid was driven by thermal and solutal buoyancy, and by

solidification contraction. This model has been shown to agree well with theoretical inverse segregation models demonstrated by Kato and Cahoon [35], as well as with experimental values obtained for a Al-4%Cu alloy, shown in Figure 2.14.

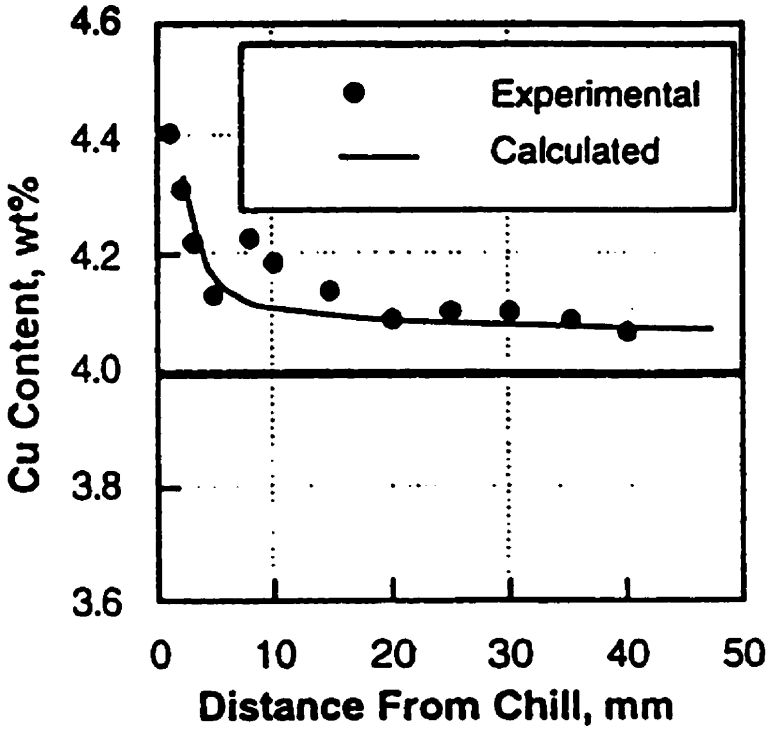

Figure 2.14 Comparison of the calculated solute distribution and experimental data in a directionally solidified Al-4.0%Cu casting. [34]

2.4.3 Channel Segregation / Convective Effects

Segregation due to gravity occurs when solid or liquid phases, float or settle within a cast (also known as sedimentation). The varying chemical compositions of each phase can cause density changes in the liquid, resulting in convection currents. This convection current may transport large amounts of solute, great distances relative to the size of the cast. In cooperation with the gravity force, small temperature gradients within the liquid provide a significant driving force for liquid convection. In order to measure convective mixing in a liquid, the dimensionless Raleigh number, R_a , is used which represents the ratio of buoyancy forces to viscous forces in the liquid [6],

$$R_a = \frac{g\beta_t R'^3 \Delta T}{\alpha \nu} \tag{2.34}$$

where g is the acceleration due to gravity, β_t is the coefficient of thermal expansion, R' is the radius of the fully liquid region, α is the thermal diffusivity, and ν is the kinematic viscosity. When the temperature gradient exceeds a critical value on the order of 10 °C/cm, significant thermal pulses at the interface resulting in non-steady state interface movement leading to an increase in mean effective partition ratio along the length of the sample. Thermal convection will enhance mass transfer at the solid/liquid interface, reducing the stagnant boundary layer. Another effect is to cause a vertical temperature

gradient in horizontal crystal growth that alters the interface position (i.e. not exactly vertical). Other phenomena such as inverse segregation are a result of relatively low velocity fluid flow within the interdendritic liquid.

A general macrosegregation equation was first proposed by Flemings [8],

$$\frac{\partial f_l}{\partial C_l} = -\frac{(1-\beta)}{(1-k)}\left(1+\frac{VG}{\Sigma}\right)\frac{f_l}{C_l} \tag{2.35}$$

where f_l is the volume fraction of liquid, β is the shrinkage factor, V is the interdendritic flow velocity, and Σ is the rate of temperature change. Under the assumption that solid densities remain constant (liquid densities may vary, negligible diffusion with no pore formation), the interdendritic flow velocity is given by,

$$V = \frac{K}{\mu g}\frac{\Delta P}{\Delta z} \tag{2.36}$$

where K is the permeability, P is the pressure, μ is the viscosity, and Δz is the mushy zone height. Assuming a binary alloy with partition coefficient, $k < 1$, interdendritic flow will change the fraction of liquid at a given liquid composition. Flow from cold to hot regions increases the liquid fraction and therefore increases the average composition, yielding positive segregation. While, flow from hot to cold regions decreases the liquid fraction, decreasing the average composition, yielding negative segregation.

Density differences arise from solute rejection during solidification known as natural convection. Even in the most stabilized solidification configuration (i.e. vertical

solidification upward, positive temperature gradient, no stirring), convection can occur if the solute rich liquid rejected at the interface is sufficiently buoyant. A condition for liquid stability is that the liquid at all times contains a negative density gradient such that,

$$\frac{\partial \rho_l}{\partial z} = \rho_l\left(\beta_t G + \beta_s \frac{\partial C_l}{\partial z}\right) \tag{2.37}$$

where ρ_l is the density of the liquid, and β_s is the coefficient of solutal expansion. Instability may still occur when equation 2.37 is met if the solute gradient is de-stabilizing and the thermal gradient is stabilizing. In such a case, a small amount of fluid is displaced upward so that it maintains its solute concentration, but increases in temperature, and therefore may become more buoyant.

Gravity driven convective flow has been studied extensively for the Al-Cu system, where liquid density differences present within a dendritic array provide an additional driving force for fluid flow. In Al-Cu alloys, the colder, solute rich liquid is denser, causing flow lines shown in Figure 2.15. As the component of fluid flow in the growth direction increases beyond the isotherm velocity, each element of metal interacts with hotter regions as it flows. These elements will change in temperature and thus composition, which may melt channels into the interdendritic region. Irregular melting will decrease the resistance to flow, producing increased flow, along with increased re-melting. Added re-melting leads to flow instability and thus highly segregates channels in the mushy zone. In order for channel formation to occur, the following relation must be

met [6],

$$\frac{VG}{\Sigma} < -1 \tag{2.38}$$

High flow rates within the channels may force solute rich liquid into the bulk liquid region leading to severe macrosegregation. Solute that decreases the liquid density during solidification will promote channel formation, while a solute that increases liquid density will suppress channel formation.

Recent research into channel segregation caused by natural convection has been conducted by a number of researchers. DuPouy et al [36] conducted directional solidification experiments on a number of Al-Cu alloys under varying solidification conditions in both unit gravity and microgravity. Initial results indicate that three different types of macrosegregation correspond to three different convective modes controlled by the orientation of the solutal density gradient in the interdendritic liquid relative to the gravity vector, independent of the density gradient in the bulk liquid. From the above, DuPouy developed a general criterion for the transition from diffusive to convective transport conditions,

$$\Gamma = \frac{V^*}{R} \tag{2.39}$$

where V^* is the mean interdendritic flow velocity. The dimensionless parameter, Γ, gives a measure of the effect of interdendritic flow on segregation. When the flow is parallel to the isotherms, no segregation will occur.

Hong et al [37] and Cahoon et al [38] performed further microstructural and segregation comparisons. For the hyper-eutectic Al-Cu system, macrosegregation results similar to those of DuPuoy et al [36] were found, where samples solidified in unit gravity exhibited maximum segregation amounts on the order of 4 to 6 wt%Cu. Such results were attributed to convective transport, although in some cases, segregation was due to sedimentation during melting. Macrosegregation studies made by Ojha et al [39] on Pb-Sb alloys indicate that thermosolutal convection caused by the buildup of low density solute at the tips of the dendritic array produced longitudinal segregation. A parameter to indicate the intensity of this convection was developed,

$$[g(C_t - C_0) D_L / R C_0]^{1/2} \tag{2.40}$$

where C_t is the solute concentration at the dendrite tips. Comparing this parameter to the effective partition coefficient, the effective partition coefficient was found to decrease with increasing convection, and remain at unity in the absence of convection. Ojha et al [39] concluded that convection is caused by the density inversion ahead of the dendritic array, in the overlying melt. Mixing of the interdendritic and bulk melt during directional solidification was responsible for the observed longitudinal macrosegregation.

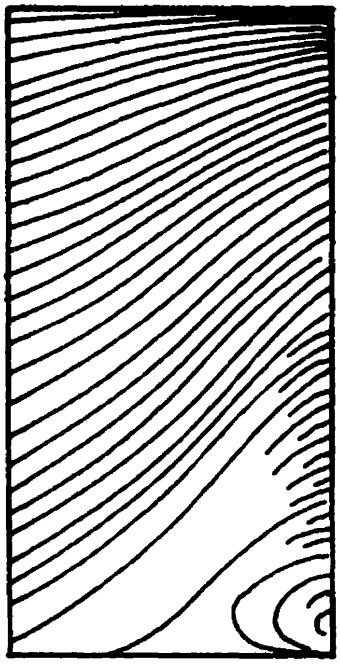

Figure 2.15 Influence of fluid flow on horizontal directional solidification, calculated flow lines for an Al-4.35%Cu alloy. [6]

CHAPTER III

NUMERICAL METHOD AND PRELIMINARY RESULTS

3.1 Introduction

Over the past few years, a computer program has been developed by Felicelli et al [1-3,40] that simulates the dendritic solidification process of a binary alloy. The algorithms are based on a mathematical model for freckle formation and macrosegregation due to convection phenomena. The solid/liquid zone is simulated as an anisotropic medium of variable porosity, where the permeability of the porous medium depends on the dendrite arm spacing and fraction of solid in the mushy zone.

In the present work, modeling of hyper-eutectic Al-38wt%Cu alloy was performed using the model as developed by Felicelli. An IBM RS-6000 computer was used for the computations located at the University of Manitoba academic computing network. In order to determine the conditions under which convective effects lead to decreased macrosegregation, initial simulations were performed with varying thermal parameters. The numerical simulations were compared with data obtained from physical experiments performed at the University of Manitoba's metallurgical laboratory in the Department of Mechanical and Industrial Engineering. The following review summarizes the numerical model written by Felicelli et al [1-3,40], and is meant to be a theoretical overview of the computer code along with its limitations and benefits. The review is followed by preliminary

simulation results, along with detailed examinations of those simulations.

3.2 Mathematical Model

The mathematical model developed by Felicelli and employed in this study is 2-dimensional and may be used for any binary-alloy melt undergoing directional solidification. Initially, a liquid binary alloy is contained in a rectangular mold, where H_T is the height of the container, and w is the width of the container, as shown in Figure 3.1. The sample is cooled at the base with a specific cooling rate. Convection is induced by prescribing a random maximum perturbation of 0.5wt% in the concentration field at the initiation of solidification. The system evolves undisturbed thereafter. The perturbation has the following form,

$$C_l = C_0 (1 + 0.005 r) \tag{3.1}$$

where $-1 \le r \le 1$ and r is chosen using a random number generator.

A chill face is induced at the bottom of the domain, and the prescribed gravity vector may take on any orientation or magnitude desired. The alloy solidifies, forming a dendritic zone that advanced upwards until the initial melt is completely solid. The dendritic zone is free to form with no predetermined size or shape since the governing equations are valid throughout the entire domain, and no internal boundary conditions are necessary. The growth process is calculated by solving the fully coupled equations of momentum, energy, and solute transport indicated in Appendix B.

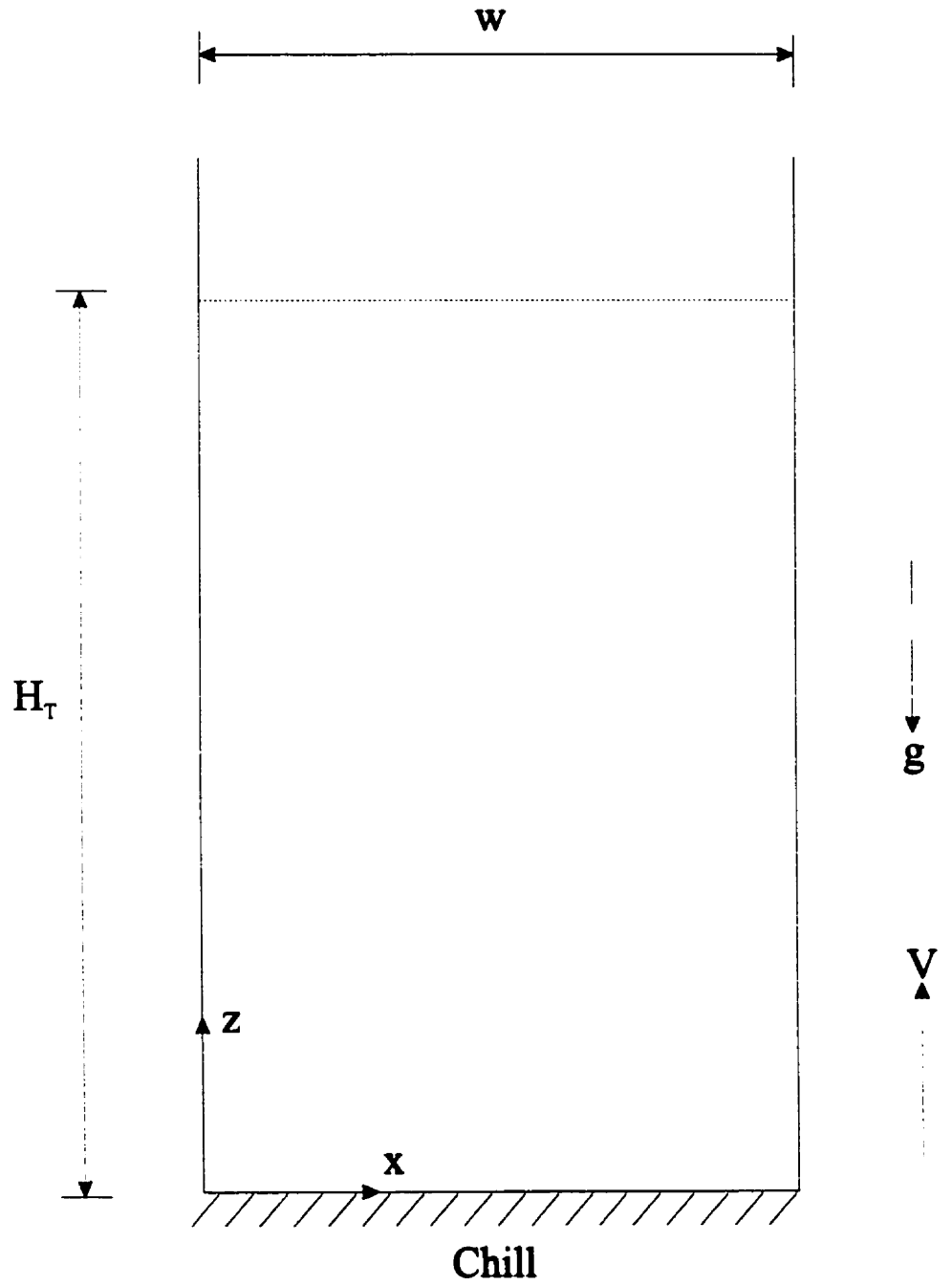

Figure 3.1 Domain definition for the finite element analysis simulations

The numerical model must maintain thermodynamic constraints dictated by the phase diagram of the alloy, with the following assumptions:

1. Only solid and liquid phases may be present; i.e., no formation of pores;
2. the flow is two-dimensional and laminar and the solid phase remains stationary;
3. the solid and liquid phases have equal thermal properties and densities;
4. there is no diffusion of solute in the solid phase;
5. the density is constant except in the buoyancy term of the momentum equations; and
6. the mushy zone is treated as a porous medium with anisotropic permeability.

The fluid velocities are the superficial velocity components, defined as,

$$u = \phi u_l \quad , \quad w = \phi w_l \tag{3.2}$$

where ϕ is the volume fraction of interdendritic liquid, and u_l and w_l are the components of interdendritic fluid velocities.

A number of other relations are needed to define the continuum model for the solidification process. Implicit in the two momentum equations (B.1,B.2) of Appendix B is an expression of the form

$$\rho = \rho_0 \left[1 - \beta_t (T - T_R) - \beta_s (C - C_\infty) \right] \tag{3.3}$$

present in the body force terms where ρ is the resulting density, ρ_0 is the reference density, T_R is the reference temperature, and C_∞ is the reference solute concentration. A further relation

between the average total solute concentration, $\overline{C}$, and the solute concentration in the liquid is required,

$$\overline{C} = \phi C_l + (1-\phi)\overline{C_s} \tag{3.4}$$

where $\overline{C_s}$ is the local solute concentration in the solid. Since the model allows for microsegregation in the solid, $\overline{C_s}$ is not uniform, and is given by:

$$\overline{C_s} = \frac{1}{1-\phi}\int_{\phi}^{1} kC_l d\phi \tag{3.5}$$

Using equation 3.5, equation 3.4 can be rewritten as

$$\overline{C} = \phi C_l + \bar{I} \tag{3.6}$$

where,

$$\bar{I} = \int_{\phi}^{1} kC_l d\phi \tag{3.7}$$

3.3 Numerical Scheme

The solution scheme is based on the rectangular bilinear Lagrangian element. The computational algorithm makes use of standard Petrov-Galerkinpenalty function formulation to eliminate the pressure variable from the differential equations [1]. All variables are interpolated using bilinear isoparametric shape functions, with time integration of these equations performed in a backward implicit scheme.

3.3.1 Boundary Conditions

The boundary conditions implemented by the program consist of temperature and velocity constraints. The following two conditions or combination for temperature, or combination thereof may be implemented at any boundary:

1. a prescribed heat flux, q,

$$-\rho_o \hat{c} \alpha \frac{\partial T}{\partial n} = q \tag{3.8}$$

where $\hat{c}$ is the specific heat capacity, and n is the unit outward normal vector.

2. a prescribed temperature, T, with corresponding temperature loss dependent on the cooling rate, r,

$$T = T_i - r\,t \tag{3.9}$$

where T_i is the initial prescribed temperature at the given node. Implied velocity boundary conditions associated with the momentum equations are no-slip at solid boundaries; i.e., $u = w = 0$, which also includes solidified regions in the domain. Additional convective and mass transport limitations may be implemented depending on the velocity boundary conditions. The following two velocity boundary conditions may be applied to the domain:

1. assuming a very tall (open) container, the normal stress along the top boundary is zero, yielding:

$$\frac{\partial u}{\partial z} + \frac{\partial w}{\partial x} = 0 \quad , \quad 2\,Pr\,\frac{\partial w}{\partial z} = \phi\,P \quad , \quad at\ z = H_T \tag{3.10}$$

where Pr is the Prandtl number, and H_T is the top of the container

2. Assuming the top boundary to be an undeformable free surface, the boundary

$$\frac{\partial u}{\partial z} = w = 0 \quad , \quad at\ z = H_T \tag{3.11}$$

conditions are:

A consequence of the tall container assumption is that a balance of diffusive and convective transport along the boundary must occur so that the following equation is satisfied at the top boundary.

$$D_L\,\frac{\partial C_l}{\partial x} + w\,(C_l - C_\infty) = 0 \tag{3.12}$$

A consequence of the free surface condition is that no transfer of solute mass is allowed at an undeformable free surface and thus:

$$\phi \frac{\partial C_l}{\partial n} = 0 \tag{3.13}$$

For all simulations, a closed top boundary situation is implemented since results must match real-life experimental data as closely as possible. Interactions with the container top are inevitable once the mushy zone has progressed to a point where there is no fully liquid region remaining in the domain.

3.3.2 Mesh Size Determination

There are two specific conditions that must be met when determining the computational grid for this program. These conditions are:

1. To properly resolve the formation and evolution of channels, Felicelli et al. [3] have determined that during the simulation of freckles, the mesh resolution must be 1mm or less. For slowly solidifying conditions, the length scale is of the order 500 μm and therefore a fine mesh spacing is required in the vertical direction, an important factor if proper resolution of the channels is desired. Studies [40,41] have

also found that channels will develop under similar thermal conditions irrespective of the size of the domain. Calculations in large domains with coarse meshes are possible, but the occurrence of channels could be missed, and the macrosegregation computed in this way could exhibit a large error.

2. There must be enough nodes to adequately resolve the distribution of the volume fraction of liquid in the mushy zone.

3.3.3 Time Step Determination

Calculations are performed using a constant time step, where the following stability conditions must be met:

1. Convection terms are treated explicitly; therefore,

$$\Delta t \leq \left(\frac{|u|}{\Delta x} + \frac{|w|}{\Delta z} \right)^{-1} \tag{3.14}$$

2. the body force term is treated explicitly; thus,

$$\Delta t \leq \left(Ra_T + \frac{Ra_s}{Sc} \right)^{-1} \tag{3.15}$$

where Ra_T is the thermal Raleigh number, Ra_S is the solutal Raleigh number, and Sc is the Schmidt number.

3. to keep computation time to a minimum, Δt should be chosen where no more than three iterations are needed for convergence within a time step.

3.4 Solution Algorithm

Once all boundary conditions, domain size, mesh resolution, and time step size have been determined, the solidification model, as defined by equations in Appendix B, is solved sequentially, and iterations are performed to reach convergence at each time step.

The following steps are performed at each node in the mesh [40]:

1. $n = 0$; u_0, w_0, T_0, etc. are known (initial conditions).
2. Time step n+1; $t_{n+1} = t_n + \Delta t$
3. $i = 0$; $u_{n+1}^{i=0} = u_n$, $w_{n+1}^{i=0} = w_n$, $T_{n+1}^{i=0} = T_n$, *etc.*
4. Iteration i+1
5. Compute u_{n+1}^{i+1} , and w_{n+1}^{i+1} .
6. Compute T_{n+1}^{i+1} .
7. Set

$$C_{l_{n+1}}^{i+1} = \begin{cases} C_L(T_{n+1}^{i+1}) & , \text{ if } C_{l_{n+1}}^{i} \le C_L(T_{n+1}^{i+1}) \\ \overline{C}_{n+1}^{i} & , \text{ if } C_{l_{n+1}}^{i} > C_L(T_{n+1}^{i+1}) \end{cases}$$

where $C_L(T_{n+1}^{i+1})$ is obtained from the liquidus line in the phase diagram.

8. Calculate ϕ_{n+1}^{i+1} from equation 3.16 in the form;

$$\phi_{n+1}^{i+1} = \frac{\overline{C}_{n+1}^{i} - \overline{I}_{n+1}^{i}}{C_{l_{n+1}}^{i+1}} \tag{3.16}$$

For nodes in which $0 < \phi_{n+1}^{i+1} < 1$, compute $\overline{I}_{n+1}^{i+1}$ from equation 3.7.

9. Compute $\overline{C}_{n+1}^{i+1}$.

10. Recalculate ϕ_{n+1}^{i+1} from equation 3.16.

11. If $|\phi_{n+1}^{i+1} - \phi_{n+1}^{i}| < \varepsilon$ (tolerance) then

$u_{n+1} = u_{n+1}^{i+1}$, $w_{n+1} = w_{n+1}^{i+1}$, *etc.*

n = n + 1

go to step 2.

Else

i = i +1

go to step 3.

End if

During each time increment, steps 3 to 11 are solved iteratively until convergence in ϕ is achieved. Note that the velocities are calculated only once per time step because they have negligible sensitivity to small changes in the rest of the dependent variables [1]. At the end of each time step, the concentration in the solid is calculated using equation (3.5). This

integral can be positive or negative depending on whether the element undergoes solidification or remelting. For solidification, the calculation is performed using (3.5), but if remelting occurs, $\bar{I}$, must be calculated from the solidification history which consists of saved values for ϕ, and $\bar{I}$. Because it is impossible to predict where or when remelting occurs, the microsegregation curve must be saved for every node in the mesh. Other phenomena such as shrinkage of the cast, or the movement of newly formed dendrites within the liquid are not taken into account. These phenomena have been addressed in other solidification models [42,43]. Recently, the present solidification model has been expanded by Felicelli to include three-dimensional modeling of ternary alloys, but will not be implemented due to the large computation times that would be required for the domain size implemented in this study.

3.5 Initial Simulation Conditions

Initial simulations involving changes in velocity were implemented to determine the effects on segregation. Random perturbations initiated convection, with a constant solidification rate, and variable temperature gradients to produce variable solidification speeds. The Al-38wt%Cu alloy was selected since considerable research has been conducted and thus experimental data is readily available for comparison. Also, significant in this alloy selection is the primary θ phase formation (Al_2Cu) with a composition of about 53wt%Cu. The liquid at the solid/liquid interface is enriched in Al, and is less dense than the bulk liquid. This liquid will tend to rise during solidification and enhance the amount of thermosolutal convection.

The Al-38wt%Cu alloy was modeled as a A-15.48wt%B alloy by shifting the θ phase portion of the phase diagram to zero. This alteration is required since the program was developed for alloys in the hypo-eutectic range where the composition of one element is zero. The thermodynamic and transport properties used in the calculations are given in Table 3.1. Figure 3.2 represents the modified phase diagram used for thermal values pertaining to the phase diagram of the alloy.

Table 3.1 Thermodynamic and Transport Properties used for simulations (all properties taken from DuPouy et. al. [44] unless otherwise noted)

Property [units]	**Value**
Average Thermal Diffusivity [m^2/s]	3.17×10^{-5}
Latent Heat of Fusion [Kg/KJ]	320.3
Average Specific Heat of Solid [KJ/Kg K]	0.959
Thermal Expansion Coefficient [1/K]	10.7×10^{-5}
Solutal Expansion Coefficient [1/wt%]	8.9×10^{-3}
Solutal Diffusivity [m^2/s] [32]	1.5×10^{-9}
Kinematic Viscosity [m^2/s] [45]	7.15×10^{-6}
Equilibrium Partition Ratio	0.0183
Alloy Concentration [wt%]	15.48
Eutectic Temperature [K]	821
Eutectic Concentration [wt%]	20.67
Slope for Liquidus Line [K/wt%]	-3.34
Prandtl Number	2.26×10^{-1}
Schmidt Number	4767
Solutal Raleigh Number	1.58×10^{4}
Thermal Raleigh Number	2.89×10^{-4}

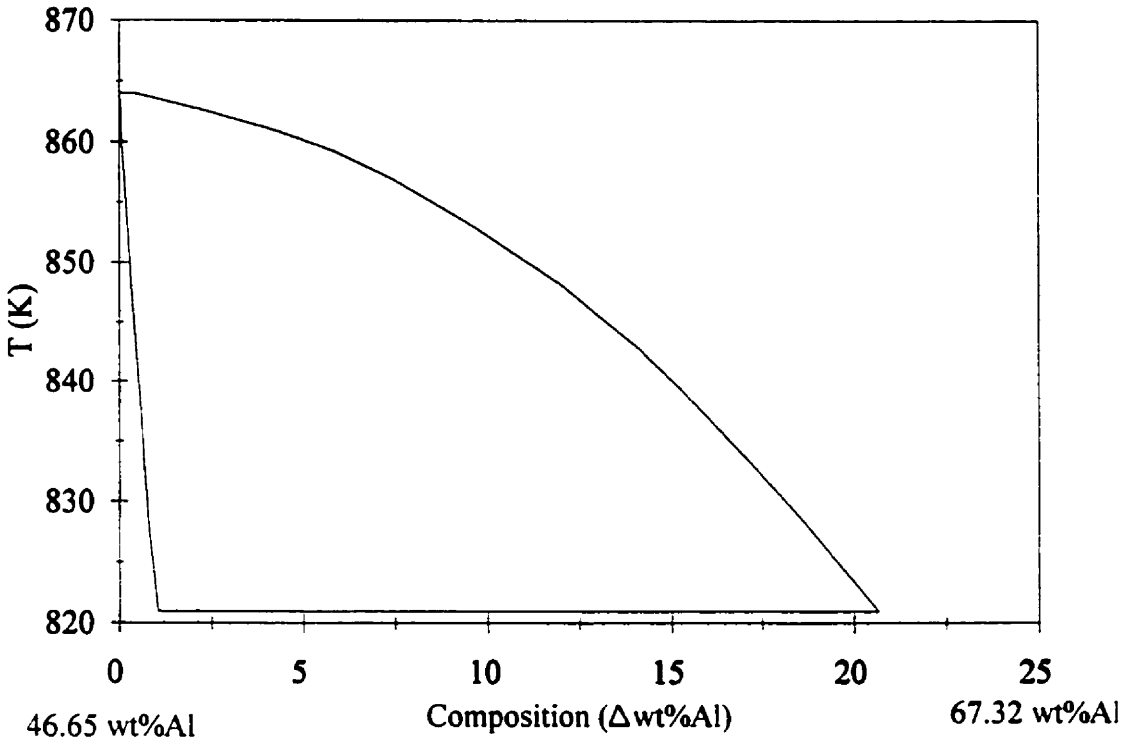

Figure 3.2 Hyper-eutectic region of the Al-Cu phase diagram modeled as a hypo-eutectic region.

Vertical solidification is considered in a two-dimensional rectangular mold of dimensions 0.6 cm wide by 8.9 cm tall, discretized with a mesh of 30 elements in the x (horizontal) direction and 80 elements in the z (vertical) direction. The solid rejects solute at the interface with a decay scale on the order of D/R, where the reference length scale, H, is 500 μm. The reference time τ, is 0.035 sec., and is based on the kinematic viscosity of the fluid and the height of the domain. The reference velocity, U, is 5.12×10^{-4} m/s, the reference

concentration is C_0 = 15.48wt%ΔAl, and the reference temperature was taken as the freezing point of the alloy (T_0 = 838.33 K).

A container described as above with zero tangential stress and zero vertical velocity imposed on the top boundary ($z = H_T$), and no-slip at the other three boundaries was considered in all numerical simulations. The alloy was initially entirely liquid, and has a linear temperature distribution varying from T_0 at the bottom boundary to $T_0 + GH_T$ at the top boundary, with G varying from 1000 K/m to 3500 K/m depending on the desired solidification speed. A time dependent boundary condition was imposed at the bottom and top of the domain where,

$$T_{bot} = T_0 - r\,t \tag{3.17}$$

$$T_{top} = (T_0 + G\,H_T) - r\,t \tag{3.18}$$

and r, is the cooling rate (3.5 K/min).

3.6 Code Verification

The numerical algorithm was initially tested by Felicelli [40] by comparing simulated output against a number of theoretical cases with known outcomes. One such test for the local solute redistribution equation given by (2.23) in section 2.4.1, a one-dimensional case

for a Pb-10wt%Sn alloy with constant temperature gradient and no convection. The calculated fraction liquid profile was shown to follow the exact solution given by (2.23). Another case involved the simulation of a Pb-61.9wt%Sn eutectic alloy in one-dimension with no convection. The simulated position of the interface during solidification advancement was shown to be in agreement with theoretical results. Thus, while the numerical model was designed for dendritic alloys with an existing mushy zone, it is also capable of managing high fraction of liquid values near the eutectic point.

Further studies [46] of the numerical code have revealed a few difficulties under certain solidification conditions. When high thermal gradients are present, the mushy zone may become extremely small. As a consequence, only one node in the mushy zone would have a fraction of liquid between zero and unity, regardless of the mesh resolution. Also, unacceptable negative values of the total solute concentration would occur near the bottom of the domain. These results are due to solidification conditions approaching plane front growth. However, numerical problems associated with high temperature gradients were not encountered in this research since all simulations performed fall within the dendritic regime.

Additional code validation was performed at the University of Manitoba in order to ensure that the numerical code would not diverge due to the initial parameters given to the algorithm. A number of parameters in the calculations may or may not influence the final morphology of the cast structure, or the final amount of segregation.

3.6.1 Random Number Generation

As mentioned in section 3.2, a random number generator was used to perturb the concentration field at the start of solidification to induce convection. Two identical simulations were performed using the initial conditions described in section 3.5, with a temperature gradient corresponding to 1000 K/m, producing an initial velocity of 6 cm/hr. The random number generator was supplied with two different seeds in order to determine if the initial random perturbations would have an effect on the final cast structure. Figure 3.3 represents the concentration differences due to the initial random number generation near the bottom of the domain at time equal to 0.03 seconds (1 iteration). It is evident that small perturbations are made in the 3rd decimal place for each case, with peaks and nulls occurring at different points along the width of the cast, with different magnitudes. Figure 3.4 represents the final longitudinal macrosegregation in the solid for both cases at the end of solidification (time = 5590 seconds). It is evident from this figure that the final longitudinal macrosegregation remains comparable along the cast, and thus the initial seed value does not significantly affect the final outcome. For all subsequent cases, identical seeds were chosen.

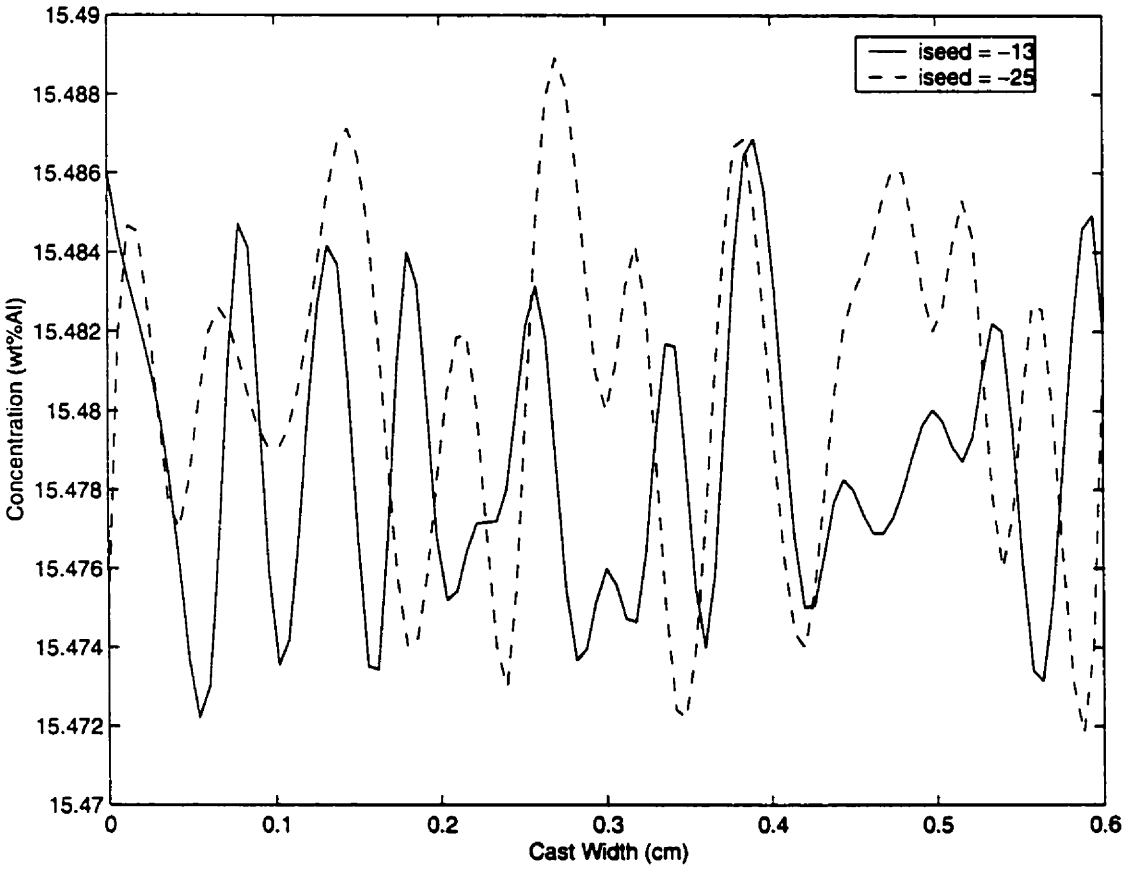

Figure 3.3 Initial random perturbations in concentration (wt%Al) with different initial seeds

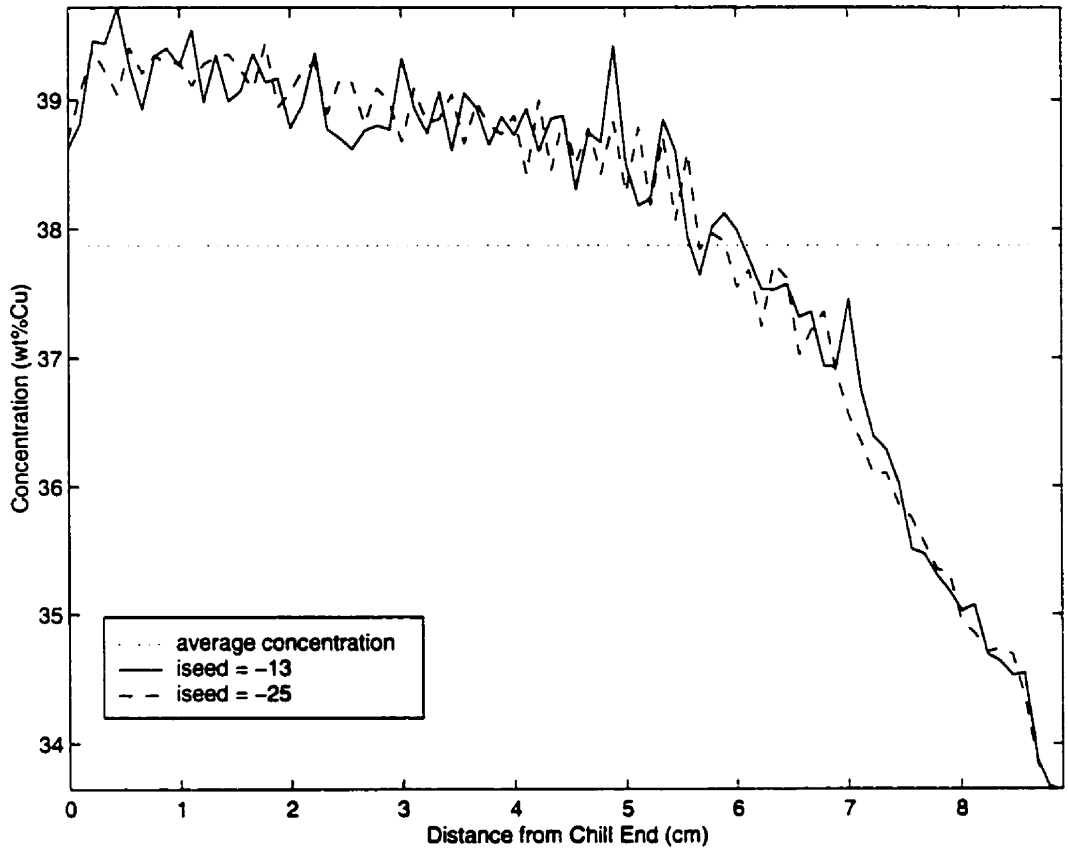

Figure 3.4 Longitudinal segregation comparison between two identical simulations with different initial seeds

3.6.2 Mesh Size Comparison

Three simulations were performed using different mesh sizes in order to determine the influence of mesh resolution on the development of channels, and hence segregation. Comparisons were made by holding all initial conditions constant, and varying the number of nodes in the mesh. To ensure proper resolution in the domain, the element size must remain near 1 mm. With increasing mesh resolution, the overall computational efficiency decreases due to the greater number of node calculations required. However, the time step may also increase with mesh size, thereby reducing the number of iterations in the simulation.

The first case consists of a temperature gradient, G, of 1900 K/m yielding an initial solidification speed of 11cm/hr. The corresponding reference length for this calculation would be on the order of 50 microns. Thus for a domain size of 6cm x 89cm, the resulting mesh would require 120x1780 nodes which is computationally expensive. To overcome this problem, a preliminary case consisting of 31 elements in the x-direction (31 Δx) by 81 elements in the z-direction (81 Δz) was computed, yielding a mesh resolution on the order of 200 microns by 1000 microns respectively. The comparison case had an increased mesh size of 31 Δx x 101 Δz. Figure 3.5 represents a longitudinal segregation plot of the final concentration of each cast structure. It is evident that both cases exhibit the same differences in segregation along the cast. Hence, the 31 Δx x 81 Δz mesh size is adequate to resolve

channels in this case, and given the CPU compilation time of 19 hours as opposed to 24 hours (performed on an IBM RS 6000/590), computationally speaking, the smaller mesh size is less time consuming by 25%. For slowly solidifying simulations in the range of 5 cm/hr, a 25% increase in solidification time amounts to a significant savings in CPU time. An additional test was performed by increasing the mesh resolution to $31\Delta x$ x $121\Delta z$ with little effect on the resulting segregation values and channel growth. Increased computation times do not produce more meaningful results, and therefore a mesh size of $31\Delta x$ x $81\Delta z$ is sufficient.

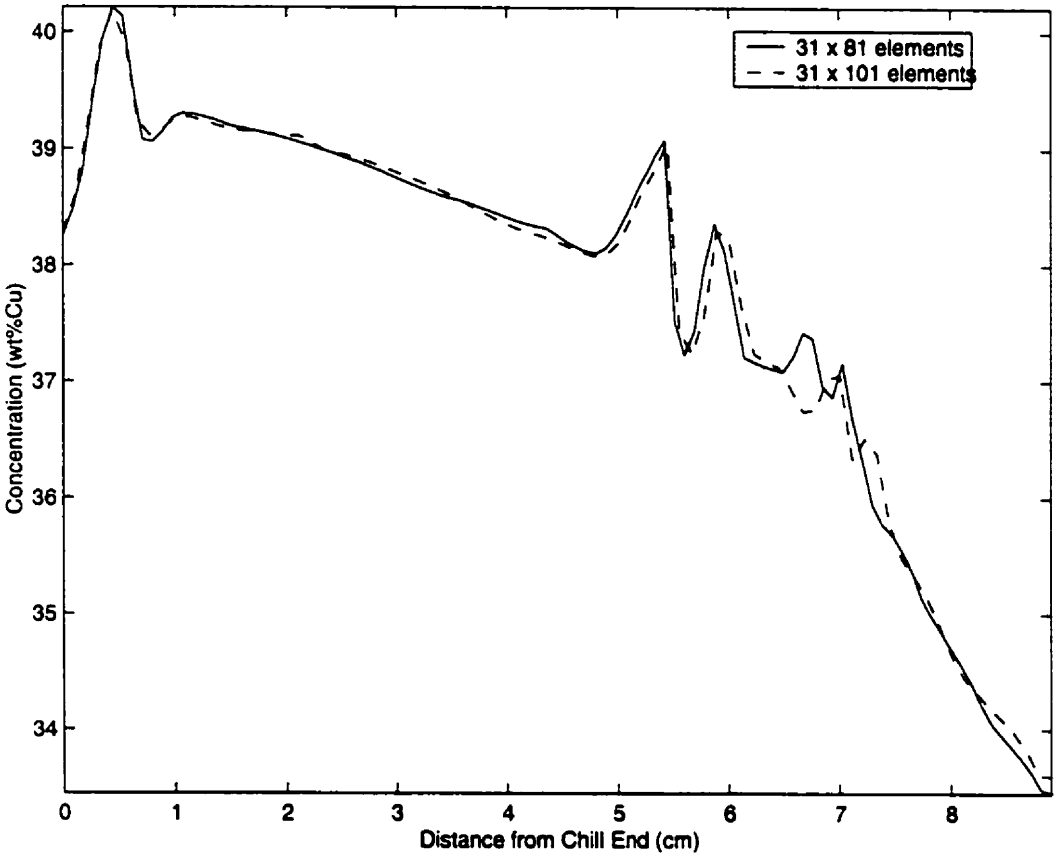

Figure 3.5 Longitudinal segregation for two identical simulations with different mesh sizes

3.7 Preliminary Simulation Results

Solidification parameters used for initial macrosegregation simulations, along with the maximum concentration differences are listed in Table 3.2. The concentration distributions along the ingot lengths are included in Appendix C. In all cases, the cooling rate was held constant while the temperature gradients were altered to produce the desired solidification speed. Variable cooling conditions have been tested [2] with similar results irrespective of fixed thermal gradient and varied cooling rate, or varied thermal gradient and fixed cooling rate. The patterns and strengths of segregation are more influenced by the growth velocity rather than either the temperature gradient or cooling rate alone. The temperature gradient has a stabilizing effect since in the absence of solute, the colder fluid resides near the interface [47]. When cooling from below, strong convection may develop even though the temperature profile is gravitationally stable, especially when a solute that is lighter than the solvent is rejected to the liquid. The temperature field can be expected to limit the height of each convection cell, and will not influence convection if the artificial boundary is far enough from the interface.

Table 3.2: Solidification Conditions and Maximum Concentration Difference values from FEM analysis.

Solidification Velocity, R [cm/hr]	Cooling Rate, r [K/min]	Temperature Gradient, G [K/m]	Maximum Concentration Difference, ΔC [wt%]
6.00	3.50	3500	4.23
11.00	3.50	1900	4.28
12.46	3.50	1685	4.33
16.15	3.50	1300	4.35
16.28	3.50	1290	4.36
16.34	3.50	1285	4.33
16.41	3.50	1280	0.18
16.60	3.50	1265	0.17
17.07	3.50	1230	0.14
18.10	3.50	1160	0.13
20.29	3.50	1035	0.12
21.00	3.50	1000	0.12

Macrosegregation results were summarized by computing the longitudinal segregation of each case. The nodes were averaged along a single horizontal direction for compositional values in the solid. The maximum segregation values along the domain were found for each case and were plotted as a function of solidification speed in Figure 3.6. As the solidification speed increases, maximum segregation values remain constant near 4wt%Cu until the solidification speed reaches a critical velocity of 16.41cm/hr. At this speed, the maximum segregation values drop below 1wt%Cu and remain near these values as the solidification speed continues to increase.

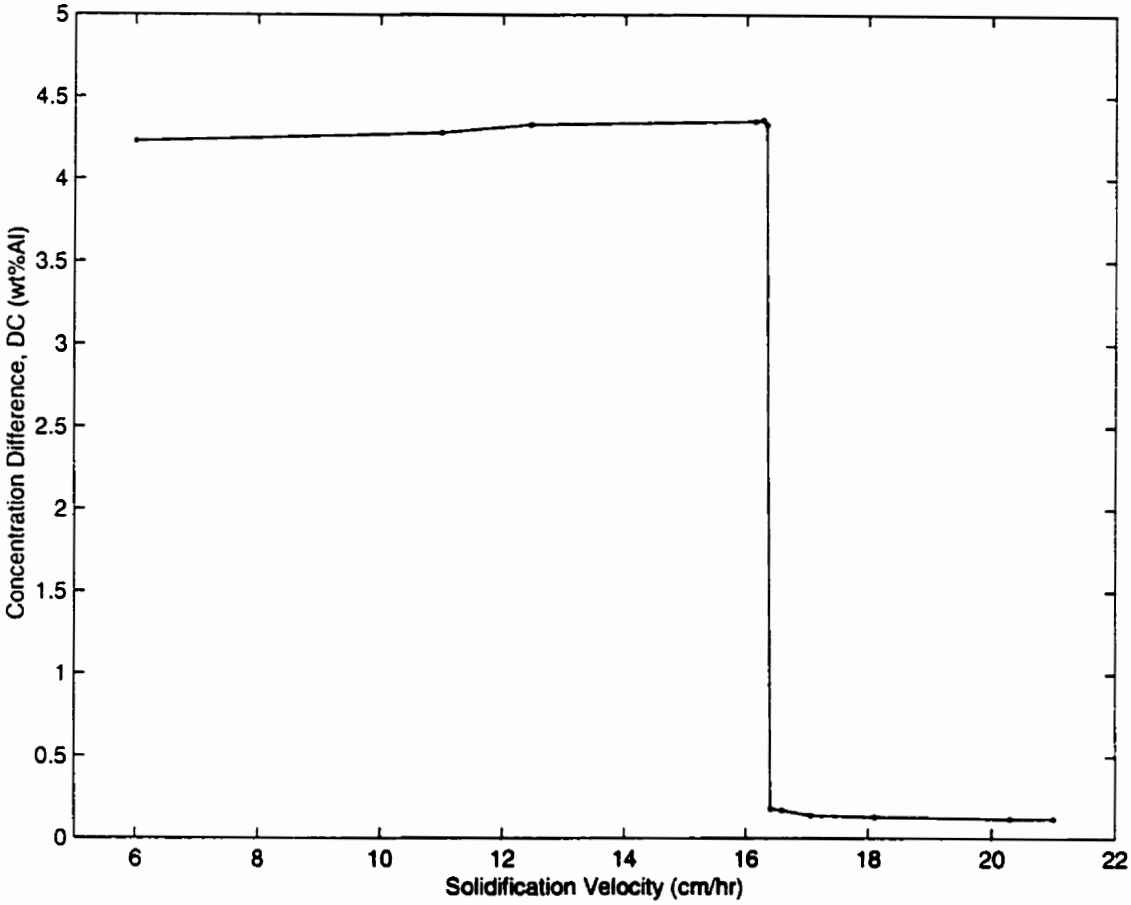

Figure 3.6 Maximum segregation versus solidification speed from FEM analysis

3.8 Simulation Experiments

From the data in Figure 3.6, the cooling rate, temperature gradient, and solidification velocity parameters were selected to determine if actual experimental results reveal the same critical velocity in terms of severity of segregation. Three experiments were performed with the values of each chosen parameter listed in Table 3.3 for each case. These parameters were selected since they span the full range of segregation, and also offer relatively even increments of solidification velocity.

Table 3.3 Cooling conditions for Vertical Solidification Experiments

Test	Cooling Rate (K/s)	Temperature Gradient (K/m)	Solidification Velocity (cm/hr)
Experiment 1	3.50	3500	6.00
Experiment 2	3.50	1900	11.00
Experiment 3	3.50	1000	21.00

3.8.1 Case #1: R=6cm/hr

As shown in Table 3.3, the alloy in Experiment #1 is subjected to a temperature gradient of 3500 K/m with a linear temperature distribution varying from 890 K at the

bottom to 1201 K at the top. With the time dependent boundary conditions prescribed, and employing the initial conditions, an initial solidification rate of 6 cm/hr is realized.

The simulated results in Figure 3.7(a), (b), and (c) represent contour plots of the fraction of liquid, concentration of solid, and fluid flow, respectively after 24 minutes of solidification. Figure 3.7(a) and 3.7(b) clearly display channel-shape penetrations of liquid into the mushy zone along the walls of the container at 24 minutes into solidification, along with a more diffuse pocket of liquid forming near the center of the cast. Figure 3.7(a) indicates a mushy zone of approximately 0.4 cm wide, which is adequate for a channel to form. These pockets are channels that form as a result of remelting, caused by the flow of solute rich fluid within the mushy zone. Figure 3.7(b) shows that the bottom portion of the cast has already produced a number of channel segregates. The alternating bands of channel penetrations are low in copper content (34wt%Cu), with overlaying bands of enriched copper content (44wt%Cu) occurring in an almost stepwise trend towards the sides of the domain. At 24 minutes into solidification, the flow velocities have not yet been influenced by the closed top boundary constraints.

The fraction of liquid, concentration of solid, and fluid flow after 47 minutes of solidification are shown in Figure 3.8(a), (b), and (c). The high initial temperature gradient is overcome by perturbations in the solid/liquid interface, and hence significant concentration differences produce strong fluid circulation throughout the bulk liquid with magnitudes reaching 16×10^{-4} m/s along the side walls, and within the interior channel. Two significant convective cells are set up with strong upward flow occurring along the walls of the domain,

as well as strong lateral flow in the center of the domain near the channel formation. This strong lateral flow causes the channels to adopt their bent morphology towards the side of the cast instead of remaining vertical. Figure 3.8(a) details the mushy-zone advancing half-way up the cast, with its height remaining near 0.4 cm. Visible side channels penetrate the solid, with strong channel formation near the right side of the cast, and a significant depression on the left side indicating the start of another channel. Figure 3.8(b) shows the results of the side channels at compositions near 34wt%Cu. Because the resulting freckles remain high in copper content, the bulk liquid is depleted to approximately 37wt%Cu. It is also evident that the strong upward fluid motion is causing the depletion of a slight difference in bulk concentration near the sides and top of the domain. Figure 3.8(c) indicates that the two convective cells have maintained their magnitude. However, interactions with the top have begun to influence the fluid flow patterns, as the main upper circulation progresses to 3.5cm from the mushy zone, compared with a distance of 4.6 cm observed at 24 minutes into solidification.

The fraction of liquid after 70 minutes of solidification detailed in Figure 3.9(a), shows a significant reduction in mushy zone width, shrinking to approximately 0.2cm from 0.4 cm observed after 47 minutes. While the side channels still remain, they are only about half the depth. The central portion of the mushy zone is now more perturbed, with multiple channel formations occurring simultaneously. The mixture concentration given in Figure 3.9(b) shows how over the past few minutes of solidification, the morphology of the channels has been altered, producing a less ordered observance of freckles. This is due in part

to a number of contributing factors:

1.The bulk liquid has been reduced in composition to 35wt%Cu, thus approaching the eutectic composition. We expect much smaller local solidification times at the interface, resulting in a reduced development time for the formation of channels.

2. Because the flow is interacting with the top boundary causing compressed fluid patterns, the two convective cells are not as well defined as before, as shown in Figure 3.9(a). The flow magnitude has dropped slightly to 12 x 10^{-4} m/s, but a strong upward flow still remains at the side walls, as well as strong lateral flow in the center of the domain.

The fluid flow magnitude remains constant until the initiation of interactions between the solid/liquid interface and the container top. As the solid forms, the cooler Al-rich liquid is rejected from the mushy region, and flow patterns force this liquid up into the cavity. During solidification, the bulk liquid becomes enriched in aluminum and results in positive segregation due to a positive buoyancy force. As the permeability increases with increasing liquid fraction, there is less resistance to flow. This is the cause of the formation of strong plumes form the channels to the bulk liquid. Since we are dealing with a relatively small mushy zone, the channels from the interior of the cast manifest themselves as freckles. The liquid near the walls is flowing upward (Figure 3.7(c), 3.8(c), 3.9(c)) and is enriched in aluminum (Figure 3.7(b), 3.8(b), 3.9(b)). Over time, it is evident that the concentration of

the liquid in the channels decreases with time since a lower concentration lowers the freezing point. These regions will solidify last and produce localized solute depleted channels.

Figure 3.10 shows a completely solidified ingot of the 6 cm/hr case. The alloy completely solidified in 94 minutes. Strong radial segregation is observed along the walls where the composition dropped to 34wt%Cu. Longitudinal macrosegregationis also evident from Figure 3.10, and is shown in Figure 3.11 where the average composition varies from 40wt%Cu at the bottom of the cast to 34wt% near the top. The pocket like freckles have solidified with a lower concentration than the surrounding material. The strong positive segregation at the top of the mold is due to the accumulation of buoyant solute-depleted liquid, produced from a continuous discharge of interdendritic fluid from the channels in the mushy zone. The solute depletion in these regions occurs at the expense of solute-rich regions in the bottom and middle of the cast, and is associated with large scale fluid circulation throughout the mushy zone, driven by solutal buoyancy. The alternating fingers of compositionally lighter and heavier fluids are ascending and descending to the liquid interface. This characterization is a result of double-diffusive convection, where the channels are fed by dendritic entrainment, producing stable convective plumes.

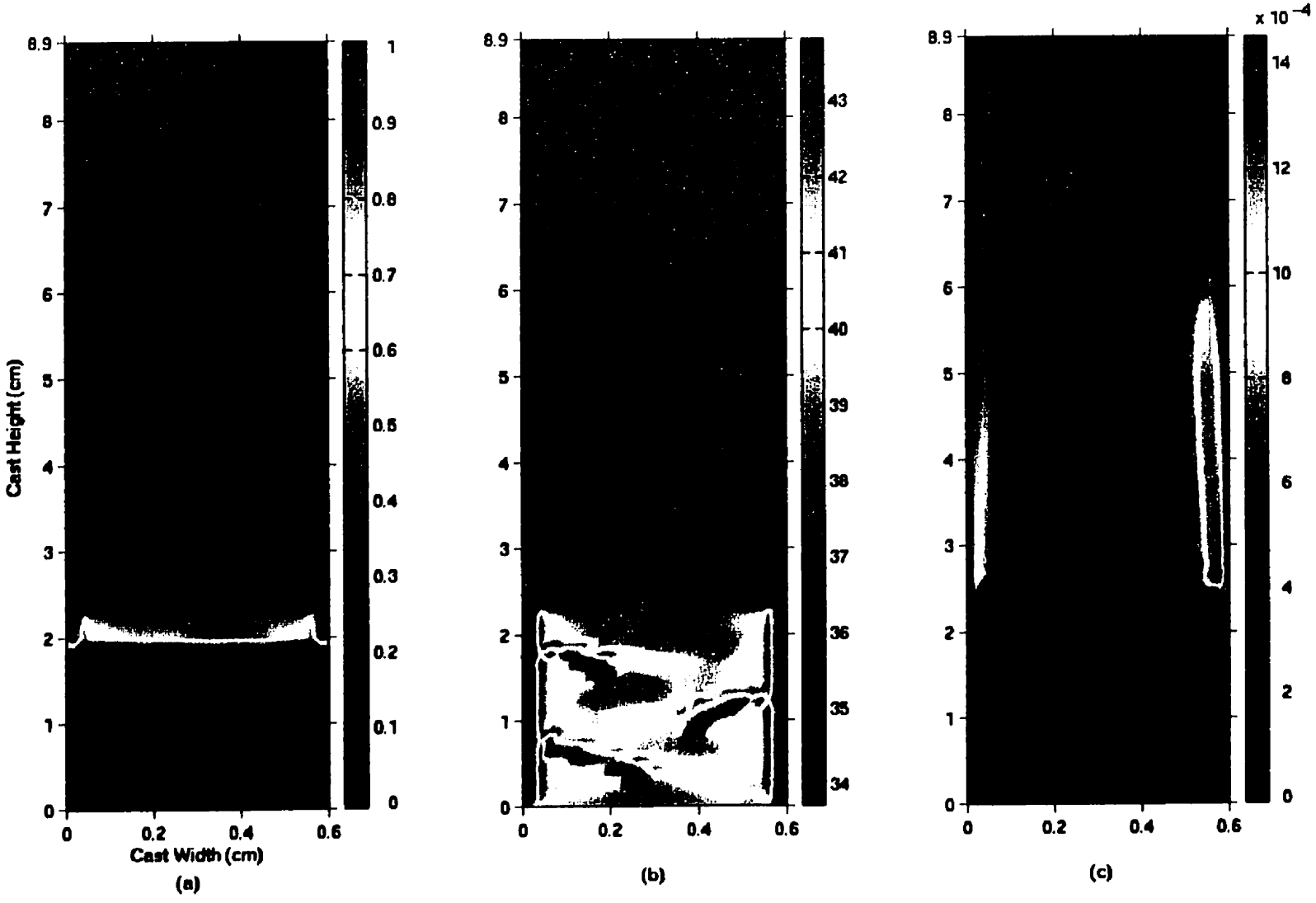

Figure 3.7 Solidification of the Al-38wt%Cu alloy at R = 6 cm/hr, time = 24 minutes. (a) Fraction liquid. (b) Concentration of mixture (wt%Cu). (c) Velocity vectors overtop streamlines (m/s)

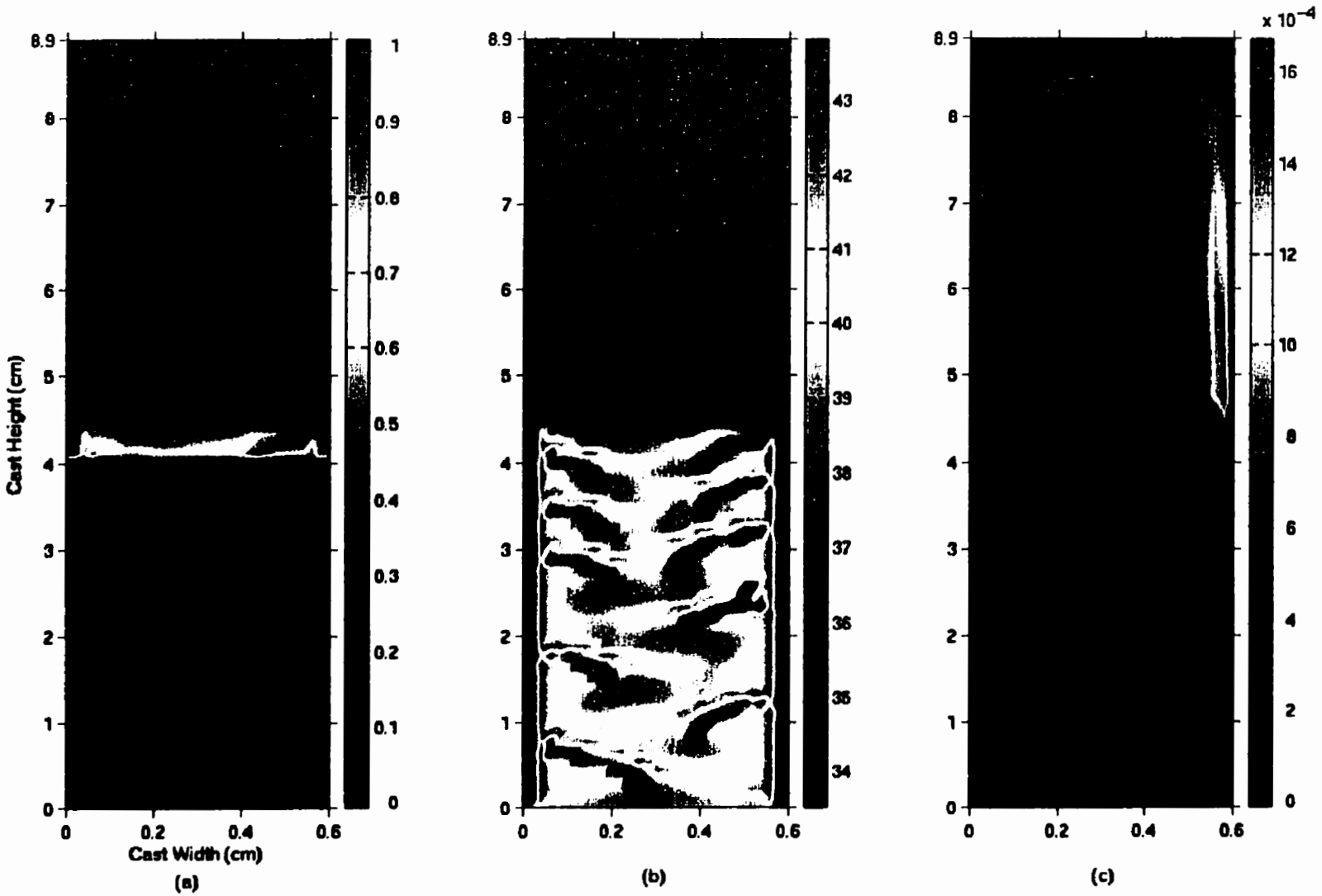

Figure 3.8 Solidification of the Al-38wt%Cu alloy at R = 6 cm/hr, time = 47 minutes. (a) Fraction liquid. (b) Concentration of mixture (wt%Cu). (c) Velocity vectors overtop streamlines (m/s)

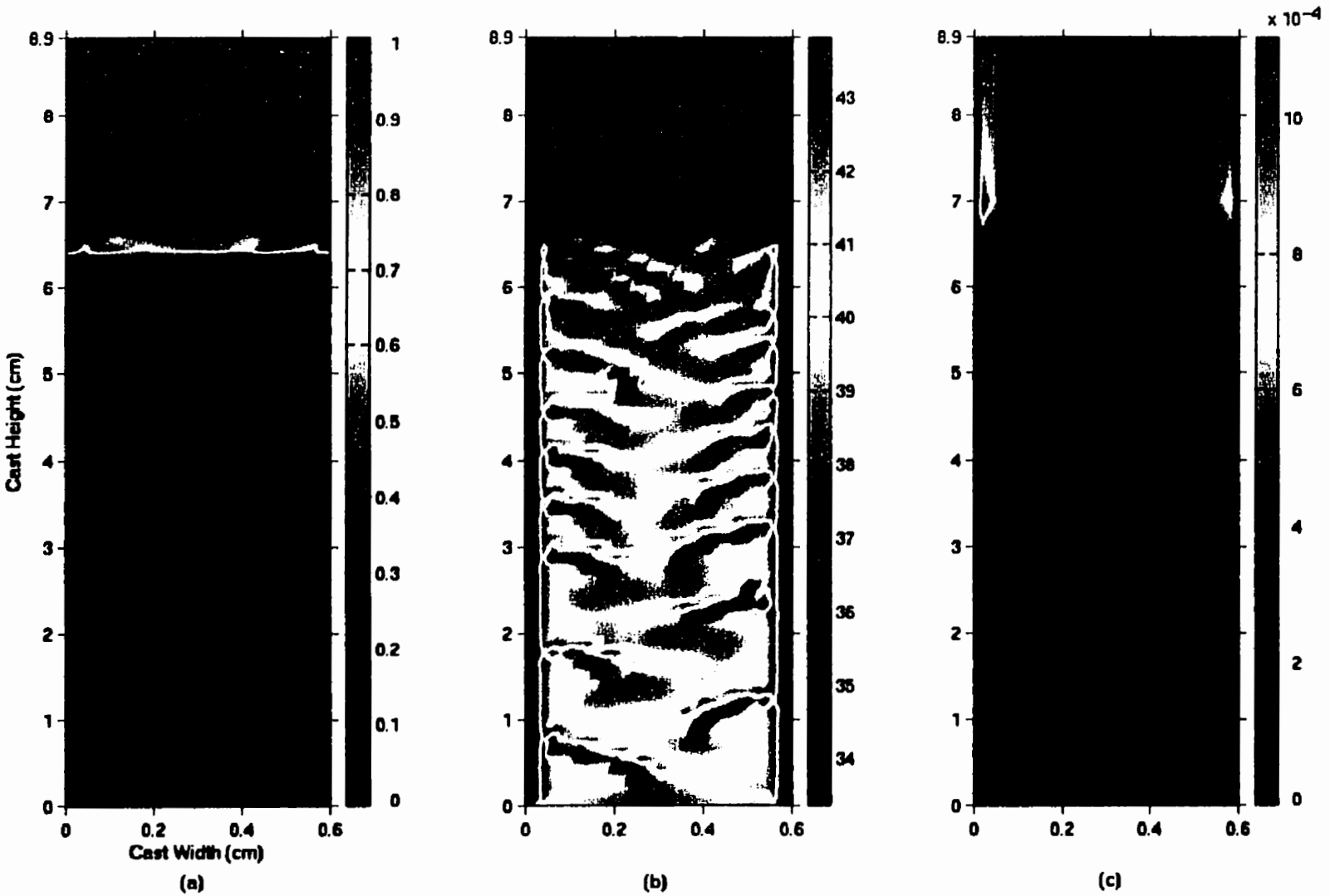

Figure 3.9 Solidification of the Al-38wt%Cu alloy at R = 6 cm/hr, time = 70 minutes. (a) Fraction liquid. (b) Concentration of mixture (wt%Cu). (c) Velocity vectors overtop streamlines (m/s)

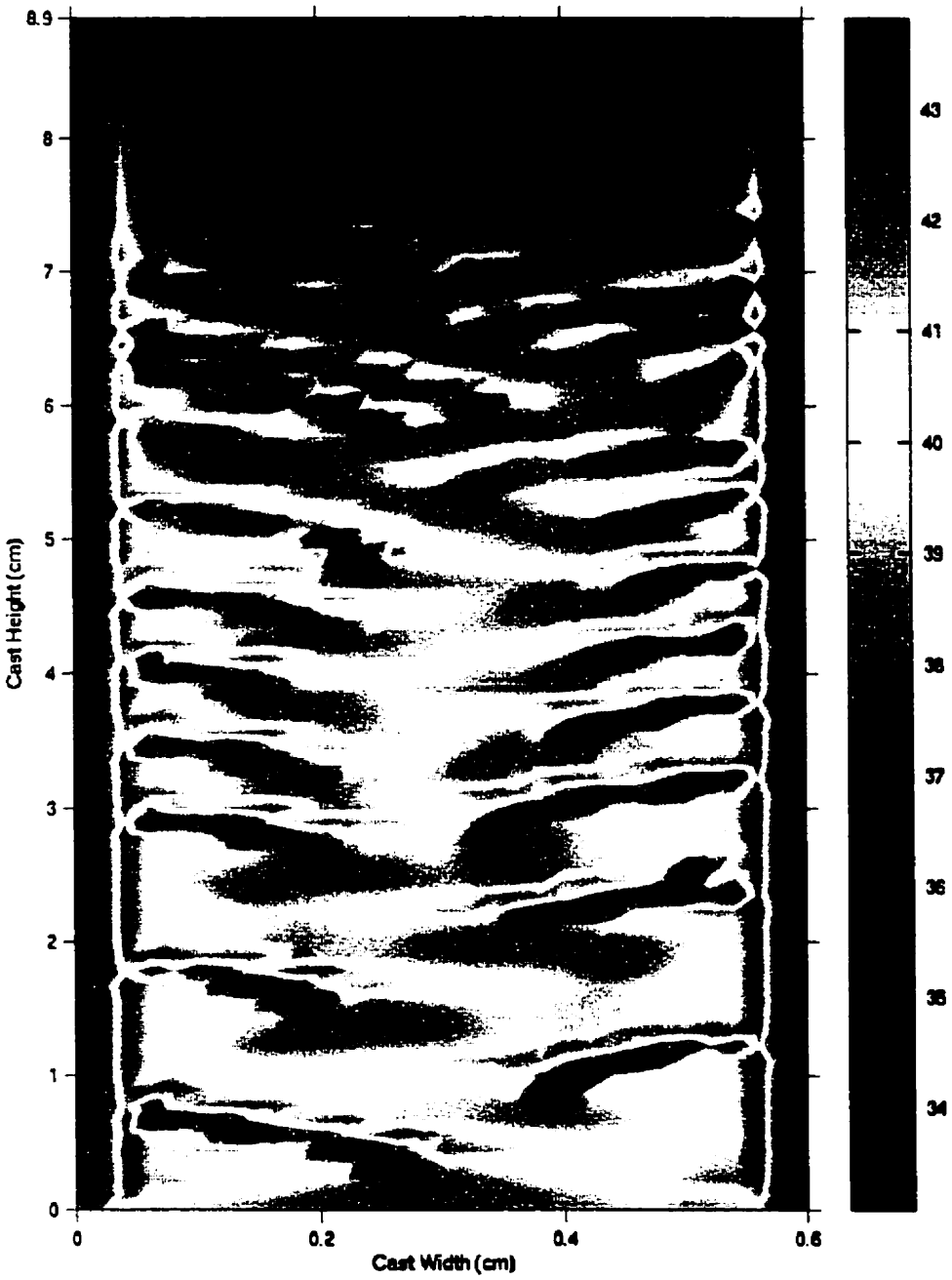

Figure 3.10 Fully solidified Al-38wt%Cu alloy at R = 6 cm/hr, time = 94 minutes, concentration of solid (wt%Cu)

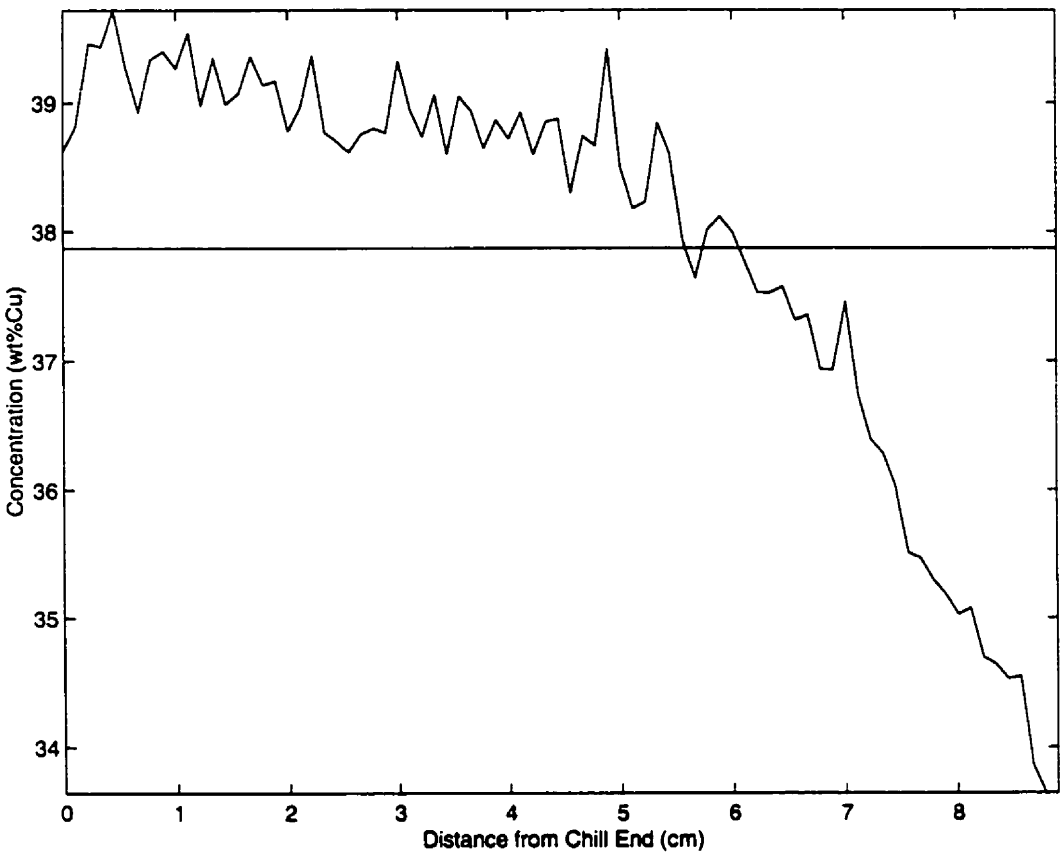

Figure 3.11 Longitudinal segregation of Al-38wt%Cu alloy solidified at R=6 cm/hr

3.8.2 Case#2: R= 11cm/hr

The second experiment implements a temperature gradient of 1900 K/m, yielding an initial growth rate of 11 cm/hr. The initial solutal perturbations remain adequate to set up two fluid circulations in the bulk liquid of the same magnitude as case #1 in section 3.8.1. Figure 3.12 represents the solidification results after 13 minutes have elapsed. Figure 3.12(a) reveals that the mushy zone has increased in height in comparison to case#1, to 0.9cm. The morphology of the interface exhibits two channels along the side walls that penetrate into the solid, while the remainder of the interface takes on a diffuse concave form. This is due to the flow characteristics that first turn inward toward the center of the cast at the solid/liquid interface. The flow penetrates the mushy zone and interacts with the higher fraction of solid. As a result, the difference in permeability of horizontal interactions forces the flow pattern to the side walls. Vertical interactions, which are less prominent near fully solidified regions, are thus not as influential.

The mixture concentration after 13 minutes shown in Figure 3.12(b) illustrates the influence of interface morphology on channel formation. In this case, no significant freckles or channels have appeared, but a difference in concentration still occurs. The concave interface causes depleted solute content in the center portion of the cast, an attribute that has been observed in a number of experimental studies [41]. A change in bulk concentration towards the eutectic concentration causes channels to broaden until an upper limit is reached

and no channels are observed. A diffuse region of lower solute concentration towards the center of the cast is all that remains. The bulk liquid maintains its composition near 37wt%Cu. However, the strong upward flow influences the composition, since the liquid ahead of the interface along the side walls is slightly more depleted in copper.

After 27 minutes, half of the cast has solidified (Figure 3.13), and a significant pocket of solute depleted liquid has formed in the center of the cast. The solid/liquid interface has become more depressed in the center of the cast, with obvious plumes emanating from the side channels. The mushy zone width has remained constant at 0.9cm. At this point during the solidification process, the bulk liquid now varies from 36wt%Cu at the side walls to 37wt%Cu at the interior of the cast near the interface. Streamlines in Figure 3.13(c) are of the same order of magnitude as the 6 cm/hr case, where there was the formation of two convective cells. An important difference between case #1 and case #2 is that the interaction of the convective cells with the top of the container, occur from the very beginning of solidification for case #2. This interaction seems to alter the bulk liquid concentration distribution by causing radial variations across the cast. Lateral velocities do not appear to be as strong at the solid/liquid interface as in case #1, but the upward flow near the side walls is more pronounced, yielding more obvious plumes in the fraction of liquid (Figure 3.13(a)). As the fluid penetrates the mushy zone, lateral flow occurs at the walls of the ingot, where the flow joins the side channels and is propelled into the bulk liquid.

Figure 3.14 illustrates the segregation after 40 minutes of solidification has been completed. The mushy zone has reduced in width to 0.7cm, and the depression in the center

has grown, while the side channels continue to penetrate the solid to the same depth. The concentration in the solid reveals that a single large depleted zone of copper at 33wt%Cu has formed at the center of the cast with the same bent morphology as that found in case #1. The bulk liquid has now been depleted to 35wt%Cu, which is similar in composition to case #1 after 75% completion of solidification. The channels do not continue to grow vertically, but turn toward the side walls and attempt to join the side channels. This occurs because channels will always follow the strongest path of convective flow. In this case, flow is laterally dominant at the growth front due to the highly unstable nature of thermosolutal convection. Convection itself is easily perturbed by small variations in the concentration field, an effect that is accentuated in liquid metals with small solutal diffusivities and small viscosities. The convective cells near the top of the container are highly influenced by the top boundary condition, although the flow magnitude has not yet dropped due to their interactions. The flow direction indicates diminished central flow, but with strong lateral flow to the side walls. Because the system is unstable, interactions with the top wall have perturbed the convective cells, and thus the convective pattern and perturbations are not symmetric [40]. The upward flow is produced by the buoyancy of the lighter element (Al) which overcomes the effect of the heavier element (Cu).

A plot of the total concentration of the fully solidified cast shows that there is segregation in the channels along the wall and within the interior pocket, with maximum values near 41wt%Cu at the bottom of the cast, and 33wt%Cu near the top of the cast (Figure 3.15). By doubling the solidification speed, longitudinal segregation remains

relatively constant, shown in Figure 3.16, since the same flow patterns and magnitudes are at work. Solidification proceeds within a convection regime that is dominated by the concentration field of the alloying component. The isotherms remain flat and normal to the growth velocity because the thermal diffusivity is larger than the solutal diffusivities, preventing the isotherms from being affected by the convection. For example, the 6 cm/hr case and 11 cm/hr case show horizontal isotherms. However, the plots of concentration show strong irregularities because of the solutal convection.

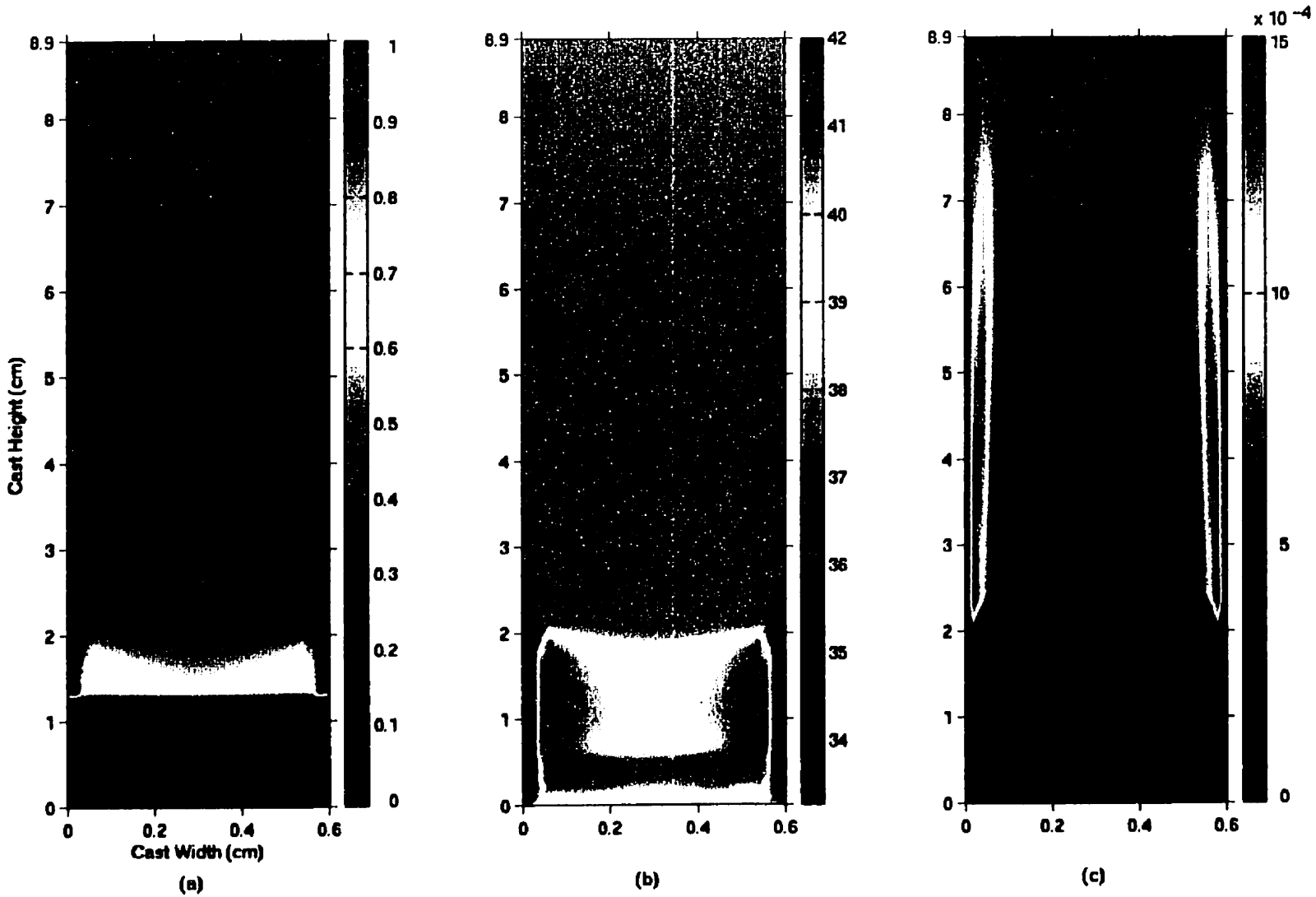

Figure 3.12 Solidificationof the Al-38wt%Cu alloy at R = 11 cm/hr, time = 13 minutes. (a) Fraction liquid. (b) Concentration of mixture(wt%Cu). (c) Velocity vectors overtop streamlines(m/s)

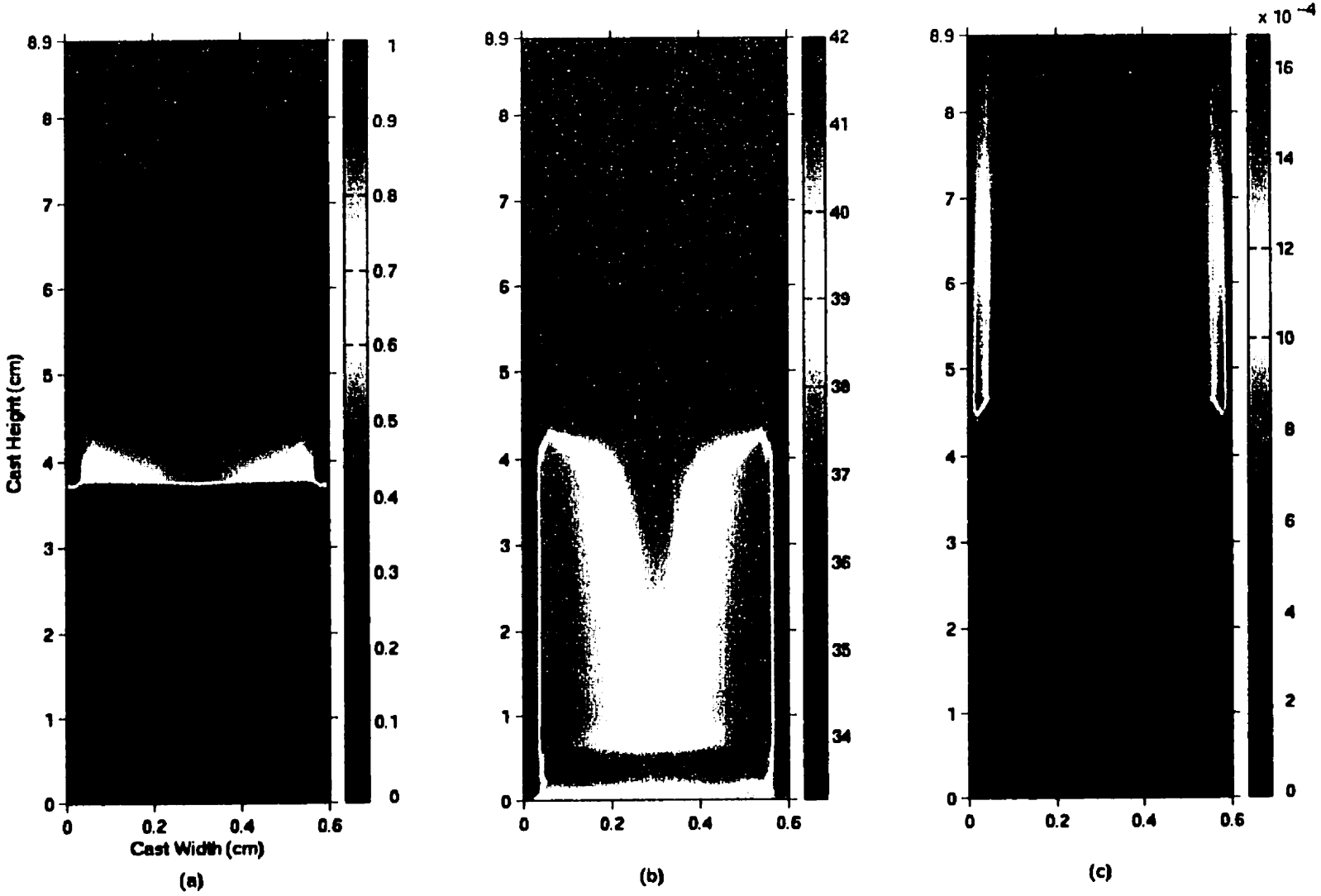

Figure 3.13 Solidification of the Al-38wt%Cu alloy at R = 11 cm/hr, time = 27 minutes. (a) Fraction liquid. (b) Concentration of mixture (wt%Cu). (c) Velocity vectors overtop streamlines (m/s)

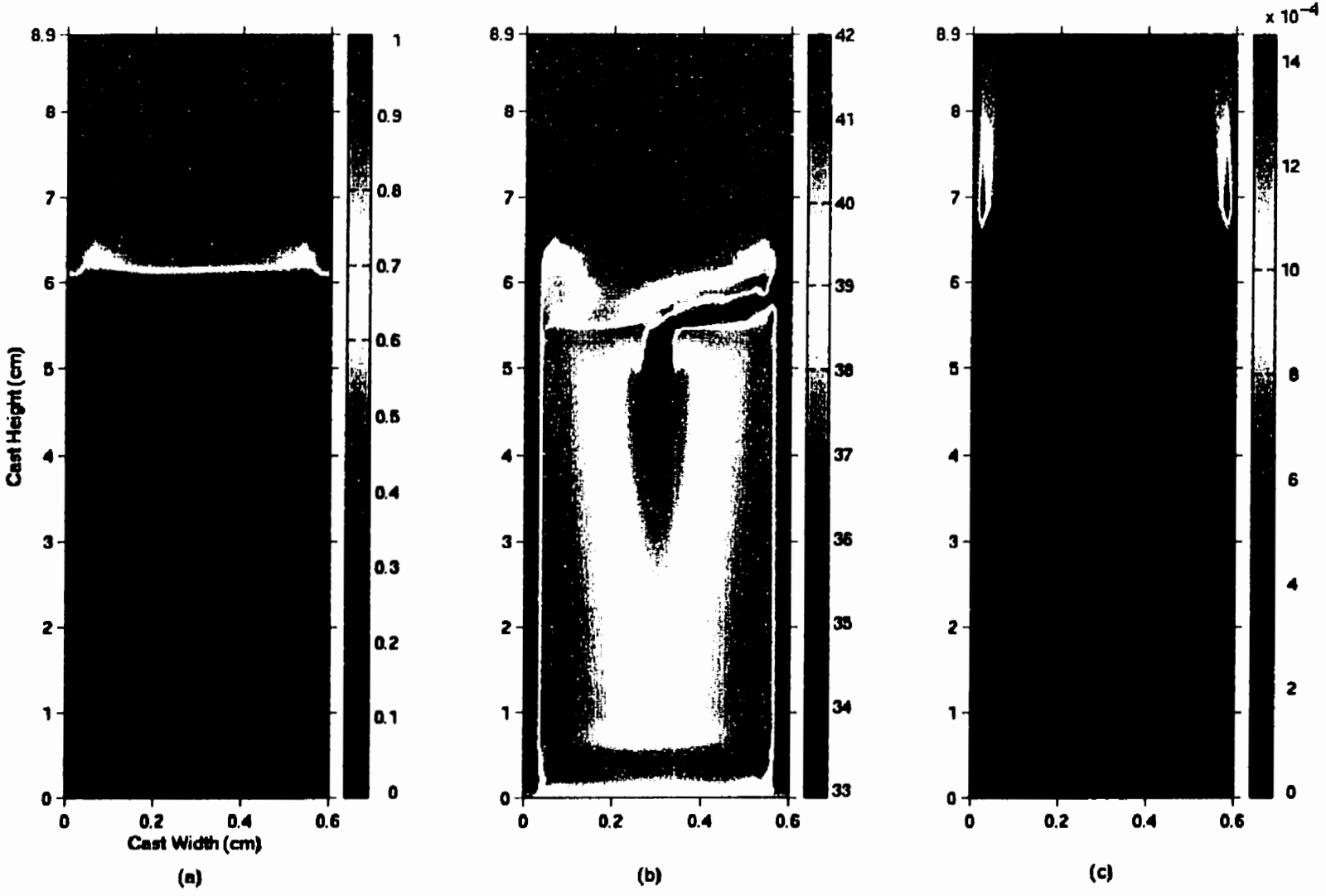

Figure 3.14 Solidification of the Al-38wt%Cu alloy at R = 11 cm/hr, time = 40 minutes. (a) Fraction liquid. (b) Concentration of mixture (wt%Cu). (c) Velocity vectors overtop streamlines (m/s)

Figure 3.15 Fully solidified Al-38wt%Cu alloy at R = 11 cm/hr, concentration of solid (wt%Cu)

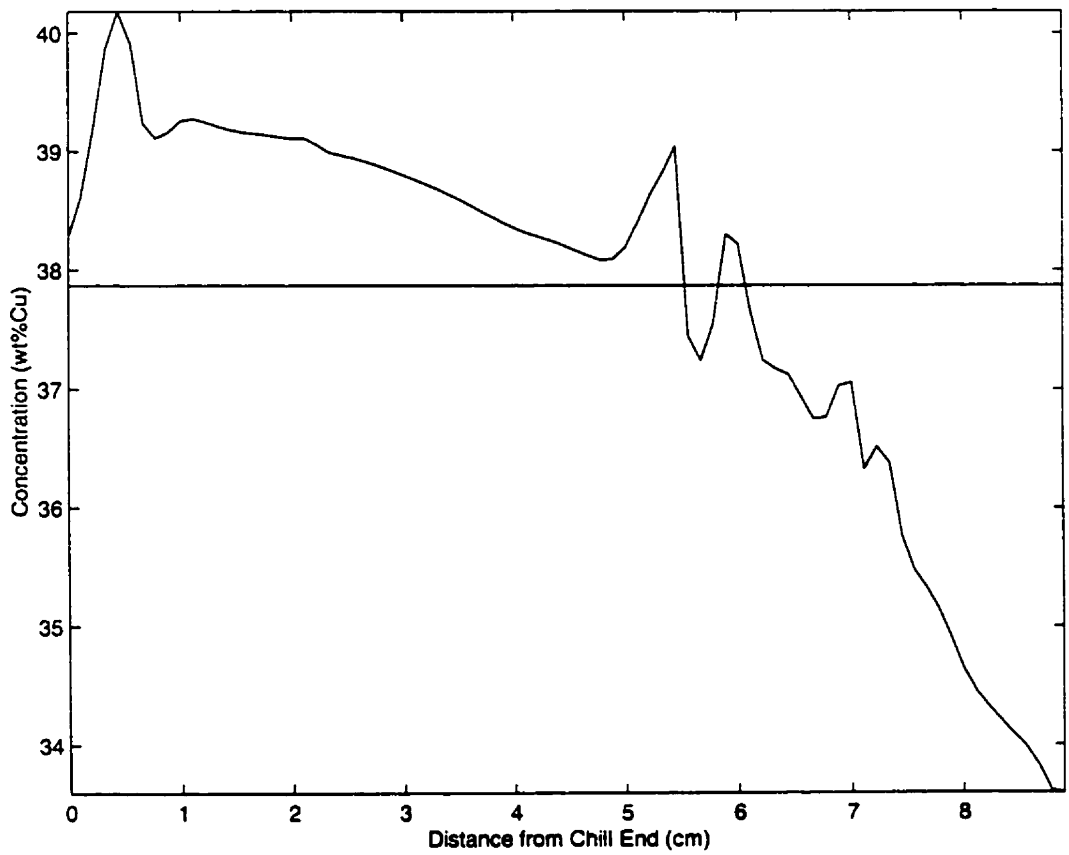

Figure 3.16 Longitudinal segregation of the Al-38wt%Cu alloy solidified at R=11cm/hr

3.8.3 Case #3: R=21 cm/hr

The initial temperature gradient of case #3 has been reduced to 1000 K/m producing an initial growth rate of 21 cm/hr. Figure 3.17(a), (b), and (c) illustrate segregation results after 7 minutes. The fraction of liquid detailed in Figure 3.17(a) reveals that the mushy zone exhibits a different morphology from case #1 and case #2. In this case, the mushy zone is distributed linearly in the vertical direction, with a width of approximately 1.6cm, and there is no evidence of side channel formation, or any internal changes in interface shape. The concentration contour plot (Figure 3.17(b)) indicates that the mushy zone takes on a minuscule difference in concentration compared to the bulk liquid. Since no side channels or internal channels have been set up, there is no evidence of freckle formation at the onset of solidification. The initial temperature gradient was not adequate enough to set up a thermal fluid field in front of the interface. Figure 3.17(c) indicates a single clockwise flow field with a magnitude a few orders less than the previous two cases, with no upward flow occurring at the side walls. Comparing this flow field to case #1 and case#2, stagnation has occurred, and since convective flow drives the rejection of aluminum rich liquid into the bulk region, the bulk concentration has not been altered from its nominal composition. Also, the fluid flow is not strong enough to penetrate the mushy zone and alter the interface shape.

Figure 3.18(a) indicates the case after 15 minutes of solidification has been completed. The mushy zone has advanced half way up the cast and no change in width or

morphology is evident. The concentration of mixture plot (Figure 3.18(b)) reveals minor changes in concentration occurring at the initial transient, with the bulk liquid remaining at the nominal composition. There is no change in local solidification time, and therefore the local freezing temperature is not altered. It is expected that solidification will evolve undisturbed throughout the rest of the simulation. The plot of flow velocity in Figure 3.18(c) shows how the fluid flow remains exclusively lateral in nature, but with magnitudes no greater than $12x10^{-6}$ m/s. Evolution of the fluid circulation involves the compression of separate flow fields as the solid/liquid interface moves up the cast. This is due to the interactions with the top boundary condition. After 75% of the solidification process has been completed (Figure 3.19), the mushy zone has advanced to the top 1/3 portion of the cast, with no change in width, and no significant perturbations. The concentration of solid in the cast also remains at the nominal composition of 38wt%Cu with no significant channel or freckle formations.

As solidification progresses, the fluid field becomes more stagnant. The effect of these velocities on the solid/liquid interface becomes apparent in the interface morphology observed in the previous two cases. Channel formation is highly dependent on the initial thermal conditions. For such a fast solidification condition, Figures 3.17 to 3.19 show that although the mushy zone has increased to approximately 1.6 cm, no significant channels or perturbations penetrate the mushy zone. The flow is not strong enough to overcome the stabilizing temperature gradient, and no solute plumes rising into the overlying liquid were observed. Thus, a non-existent solutal boundary layer is set up in front of the interface, and

there is no density inversion due to perturbation growth. The concentration in the liquid remains near the initial concentration throughout solidification. The final concentration in the solid is shown in Figure 3.20, and indicates no evidence of channel formation or concentration differences of any kind throughout the cast. Hence, Figure 3.21 reveals no longitudinal macrosegregation whatsoever.

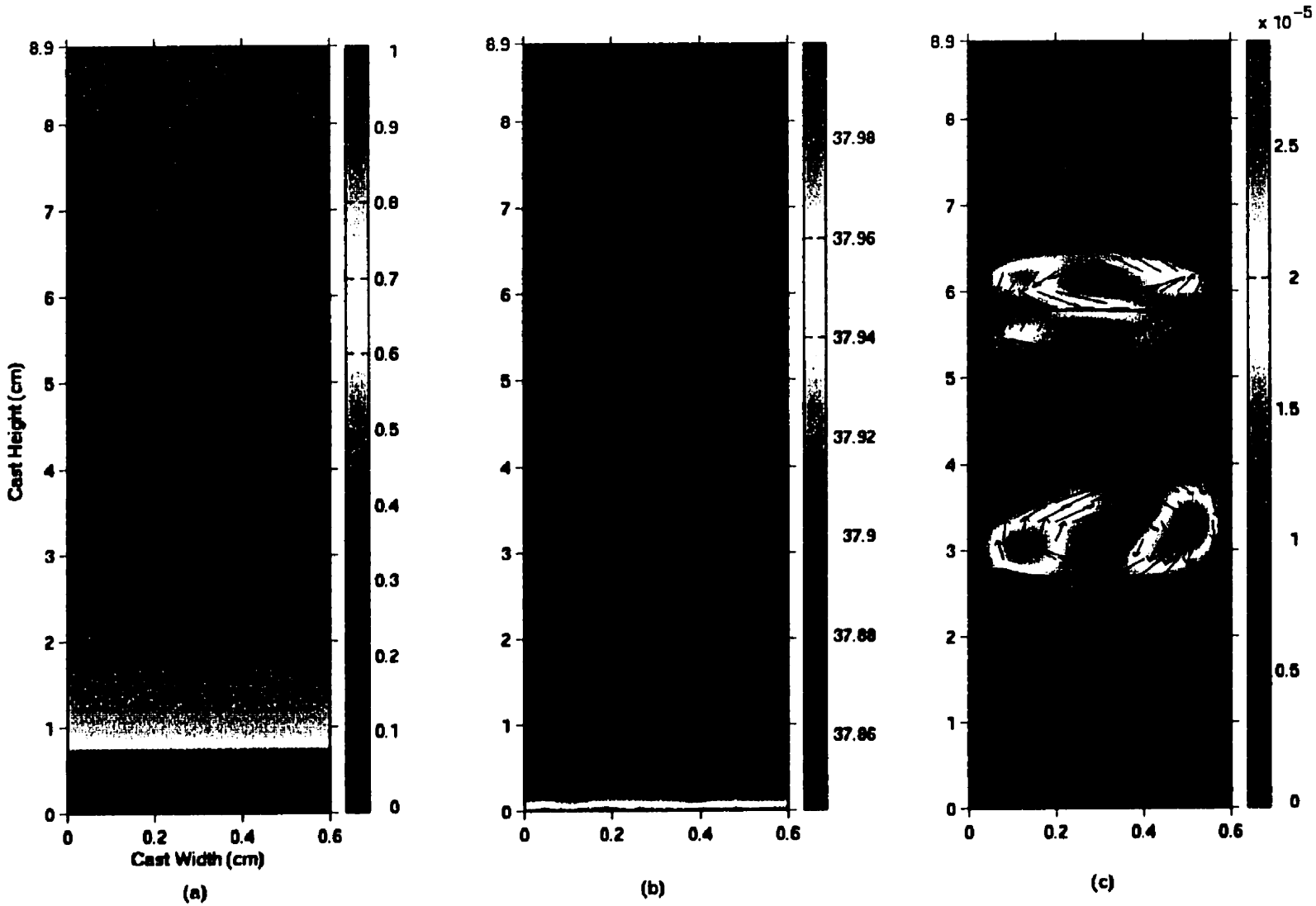

Figure 3.17 Solidification of the Al-38wt%Cu alloy at R = 21 cm/hr, time = 7 minutes. (a) Fraction liquid. (b) Concentration of mixture (wt%Cu). (c) Velocity vectors overtop streamlines (m/s)

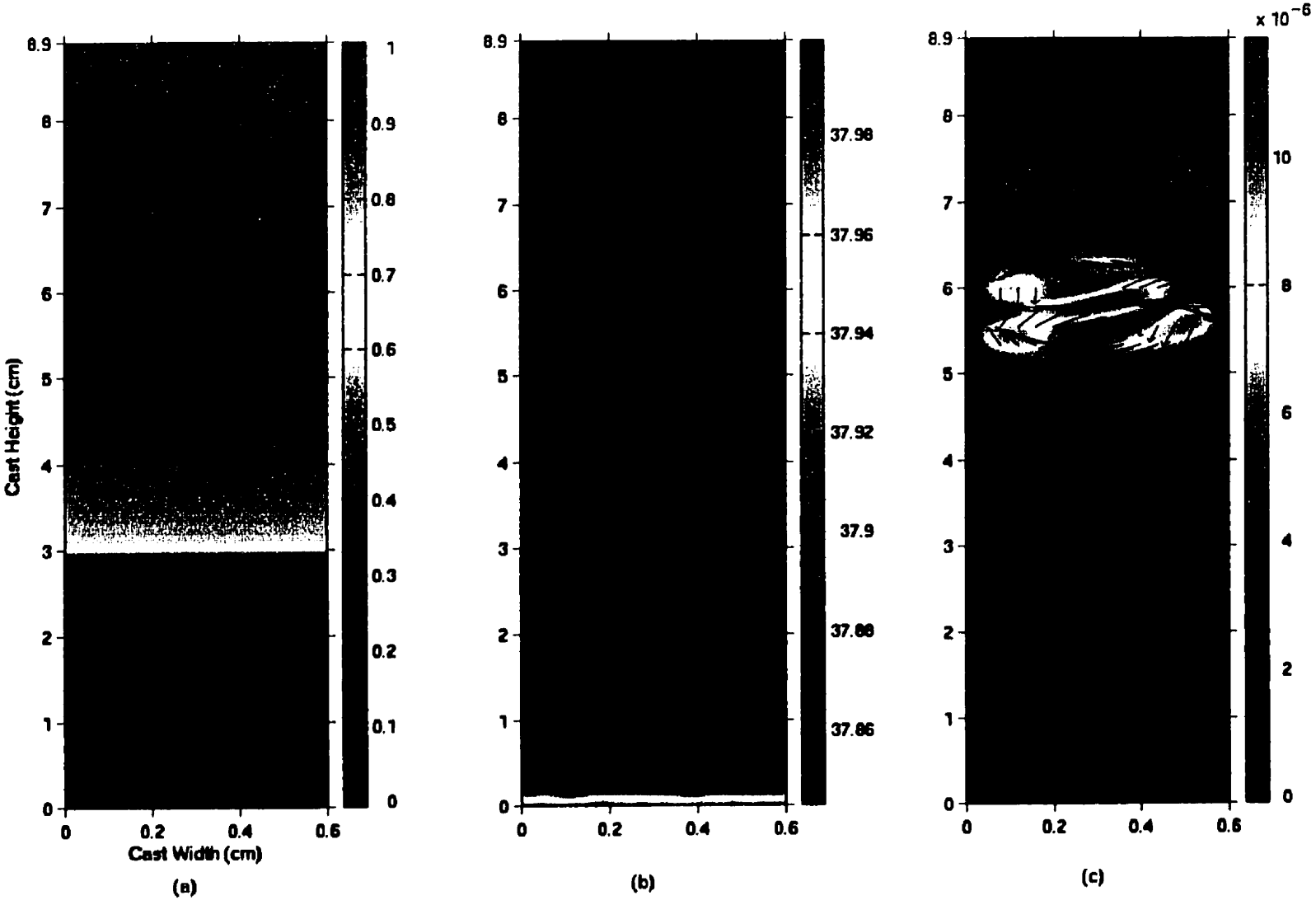

Figure 3.18 Solidification of the Al-38wt%Cu alloy at R = 21 cm/hr, time = 15 minutes. (a) Fraction liquid. (b) Concentration of mixture (wt%Cu). (c) Velocity vectors overtop streamlines (m/s)

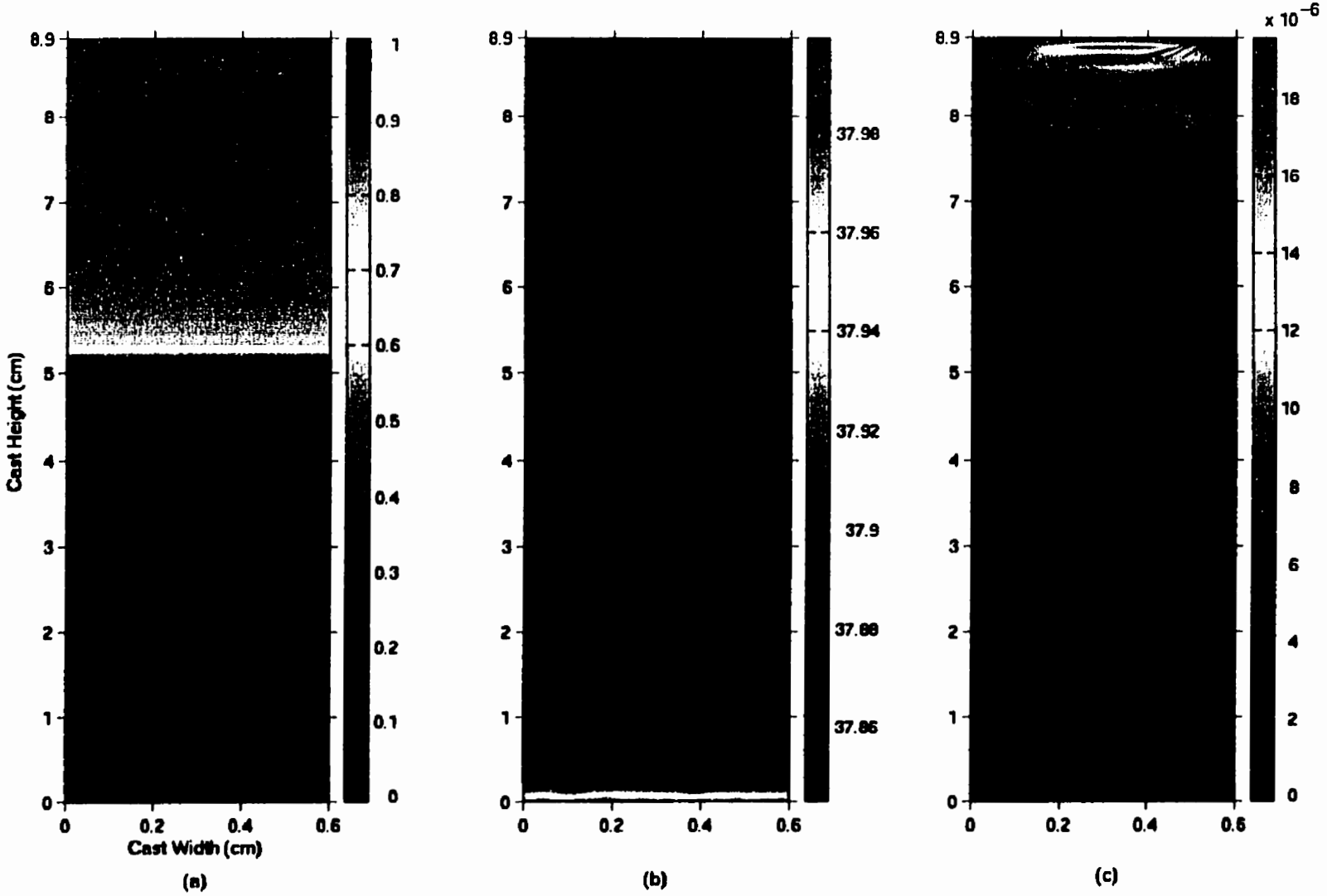

Figure 3.19 Solidification of the Al-38wt%Cu alloy at R = 21 cm/hr, time = 21 minutes. (a) Fraction liquid. (b) Concentration of mixture (wt%Cu). (c) Velocity vectors overtop streamlines (m/s)

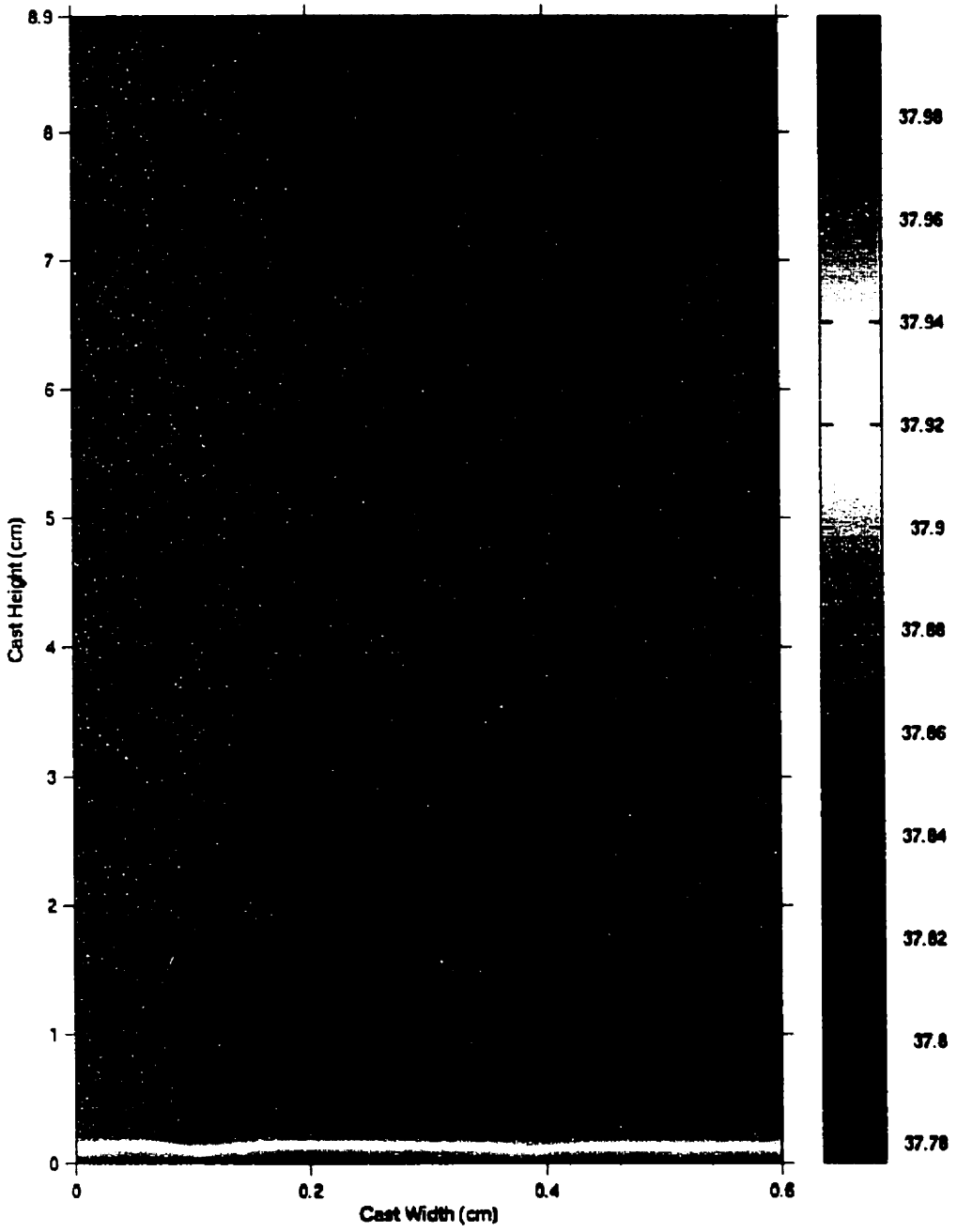

Figure 3.20 Fully solidified Al-38wt%Cu alloy at R = 21 cm/hr, concentration of solid (wt%Cu)

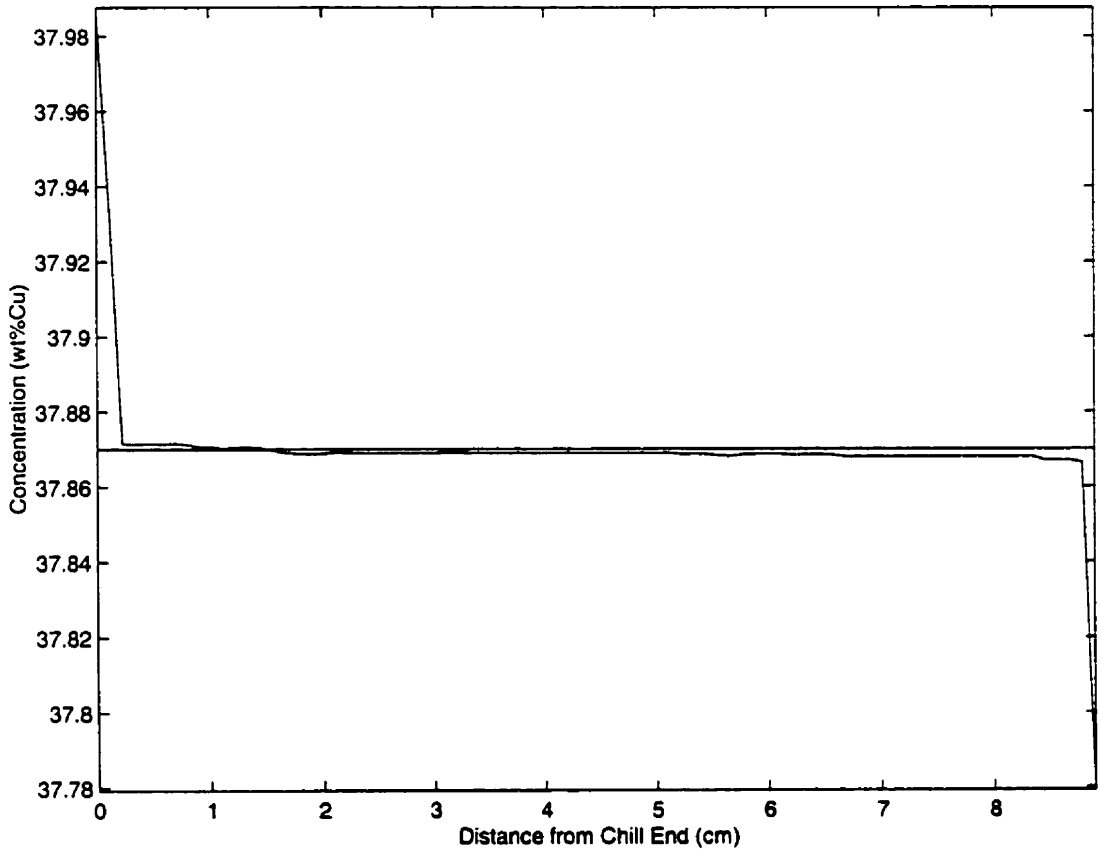

Figure 3.21 Longitudinal segregation of the Al-38wt%Cu alloy solidified at R=21cm/hr

CHAPTER IV

EXPERIMENTAL RESULTS AND DISCUSSION

4.1 Introduction

The validation of the computer code, through the comparison of simulated data with experimental results, is essential for the determination of morphologies and segregation profiles. By having accurate models of solidification processes, predictable simulations will reduce the amount of trial and error practices that are made in the foundry industry today. More insight may be achieved into the mechanisms of convective phenomena.

4.2 Preparation of Alloys

Experimental alloys were prepared by adding the appropriate amount of aluminum (Al-99.99%) and copper (Cu-99.99%). The copper component was cut into 1/16 inch pellets, and washed in a 25% Nitric acid solution before melting to reduce surface oxidation and eliminate as many impurities as possible. The aluminum component was placed in an induction furnace and brought up to 900 °C. Once the aluminum was

molten, the copper pellets were added while continuously mixing the slurry for approximately one minute. The temperature was held constant at 900 °C for 10 minutes to allow the copper to completely dissolve in the aluminum. The temperature was lowered to 800 °C, and the alloy was further mixed by pouring the melt back and forth between crucibles. The alloy was then degassed by bubbling dry argon through the melt for 5 minutes. The top surface slag was skimmed off and the remaining melt was poured into a ceramic/graphite cylindrical mold with dimensions of 6mm in diameter by 89mm in height, and allowed to air cool. Weight measurements indicate that the alloy composition was Al-37.8wt%Cu, which is adequate for comparison to the numerical calculations performed. Three samples were prepared from the same batch to ensure chemical homogeneity. The primary phase morphology, concentration, and fluid velocity parameters outlined in Chapter 3 were examined in each of the three experiments.

4.3 Experimental Apparatus

For the unidirectional solidification experiments performed, a 28 volt DC, three zone gradient-freeze QUESTS furnace was used. The furnace can provide various cooling rates for three different heating/cooling zones. It has significant advantages over other solidification methods because the cooling rate and thermal gradients can be controlled closely, producing a relatively planar isotherm at the position of the interface. A

cross-sectional view of the gradient furnace is shown in Figure 4.1.

The gradient furnace has three individual Kanthal windings along a ceramic winding former. To allow control of each of the windings, a thermocouple is located next to each winding on the inside of the former. Three Omega programmable temperature controllers were wired to the furnaces three zones. (Omega CN-2010 series). The controllers raise, hold, and lower the temperature in each of the zones (running on 120 volts AC). The alloys were placed in a ceramic capsule, fastened at one end with a graphite plug that screwed into the aluminum base plate (heat sink), to allow unidirectional cooling, while the top end contained a graphite plug to contain the sample.

Experiments were conducted by setting all zones to 800 °C, thereby melting the alloy in the capsule. When melting was complete, the furnace and capsule assembly was shaken by hand to eliminate any inhomogeneities which may have resulted from melting. Following agitation, the temperature gradient in the furnace was established by setting the temperatures in the three zones. Once the temperature gradients were established, solidification was initiated.

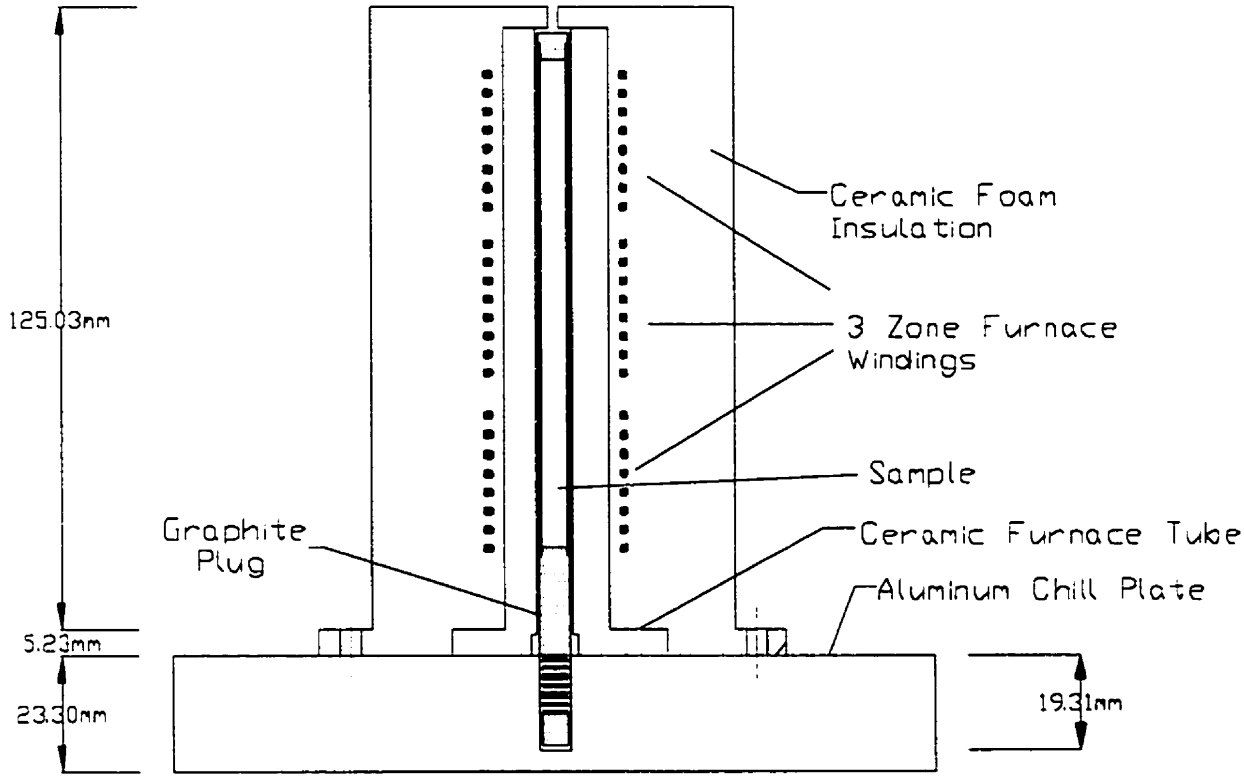

Figure 4.1 Schematic diagram of the QUESTS furnace

4.4 Microstructural Analysis

Following completion of solidification, the specimens were sectioned longitudinally and transversely to allow examinations of the microstructure. All samples were mounted in bakelite, ground on 600 grade SiC paper, followed by an intermittent polishing with a diamond paste of 6 microns, 1 micron, 1/4 micron, and a final polish with colloidal silica of less than .05 microns. Samples were etched by immersing them in Keller s reagent (950ml H20, 35ml HCl, 15ml HF), and dried using ethanol. Visual examinations were performed under a NIKON optical microscope, a JEOL-840 scanning electron microscope, and a JEOL JSM-5900 LV scanning electron microscope.

4.5 Macrosegregation Analysis

Macrosegregation of the solute element (Cu) was determined as a function of the distance from the chill face by using energy dispersive spectrometry (EDS) in the scanning electron microscope. To confirm results, longitudinal and transverse samples were subject to a volume fraction analysis using a LEITZ image analyzer. The volume fraction was determined for the θ phase and eutectic phase, and converted to their respective concentrations using the average densities of each phase.

Longitudinal sections of all samples were polished (without etching) and subjected to an EDS analysis by exposing an area of 1mm x 6mm every 5mm along the sample. All analysis were performed with an accelerating voltage of 20KeV, a constant probe current,

a machine dead time of 25%, and an acquisition time of 120 seconds. Each area was analyzed three times, and the results were averaged. The accuracy of the measurements is given by the maximum difference between the highest and lowest value for a given area The absolute accuracy of the results may only be about ±5% due to the use of pre-defined internal standards associated with the scanning electron microscope. However, only relative concentrations are required to determine the extent of segregation and therefore the samples themselves are in effect standards. In other words, the relative concentration will be accurate to about +/- 0.5 wt%.

4.6 Cooling Characteristics

The temperature recordings from the three experiments obtained from the QUESTS furnace are shown in Figures 4.2-4.4. For experimental and simulated data, cooling rates, and temperature gradients were taken at 6 evenly distributed points throughout the solidification process. Table 4.1 lists the average cooling rates, temperature gradients, and growth velocities obtained through experiment and simulation. Comparing the data in each table, simulated and experimental results are shown to be equivalent. As solidification progresses, the cooling rate, temperature gradient, and growth conditions will change due to concentration differences occurring in the bulk liquid, which alter the melting and freezing temperatures of the alloy. Solidification growth will increase as solidification progresses, and is confirmed in both the simulated

and experimental results in Table 4.1.

Table 4.1(a) Average Experimental vs. Simulated thermal histories for the R=6 cm/hr case.

Zone	Actual Cooling Rate (K/min)	Simulated Cooling Rate (K/min)	Actual Temp. Gradient (K/m)	Simulated Temp. Gradient (K/m)	Actual Growth Velocity (cm/hr)	Simulated Growth Velocity (cm/hr)
Bottom	2.70	3.50	----	----	----	----
Middle	3.50	3.46	3348	3564	6.27	5.83
Top	3.54	3.50	3333	3427	6.37	6.13

Table 4.1(b) Average Experimental vs. Simulated thermal histories for the R=11 cm/hr case.

ZONE	Actual Cooling Rate (K/min)	Simulated Cooling Rate (K/min)	Actual Temp. Gradient (K/m)	Simulated Temp. Gradient (K/m)	Actual Growth Velocity (cm/hr)	Simulated Growth Velocity (cm/hr)
Bottom	3.50	3.50	----	----	----	----
Middle	3.48	3.45	1843	1997	11.33	10.37
Top	3.52	3.50	1835	1808	11.51	11.62

Table 4.1(c) Average Experimental vs. Simulated thermal histories for the R=21 cm/hr case.

ZONE	Actual Cooling Rate (K/min)	Simulated Cooling Rate (K/min)	Actual Temp. Gradient (K/m)	Simulated Temp. Gradient (K/m)	Actual Growth Velocity (cm/hr)	Simulated Growth Velocity (cm/hr)
Bottom	3.58	----	----	----	----	----
Middle	3.50	3.47	1039	1040	20.21	20.02
Top	3.53	3.50	1028	975	20.60	21.54

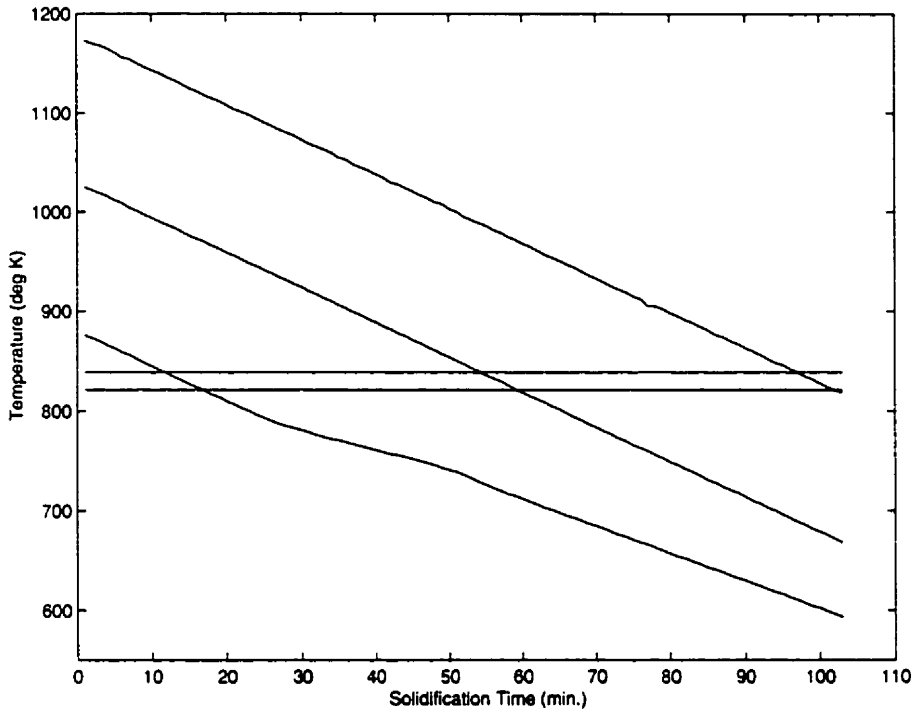

Figure 4. 2 Cooling Curve for Experiment #1, R=6 cm/hr

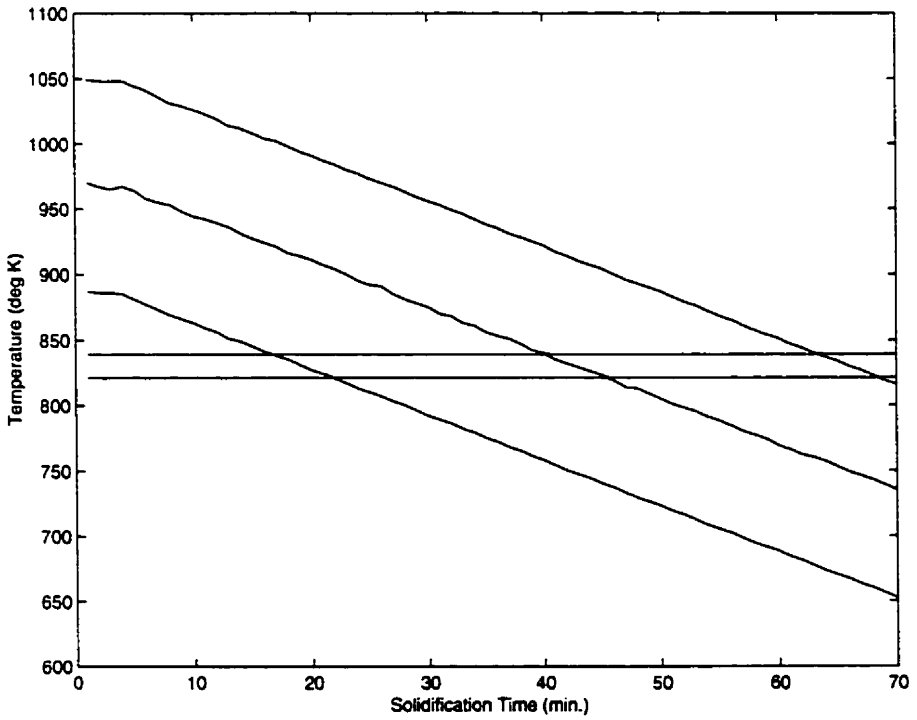

Figure 4. 3 Cooling Curve for Experiment #2, R=11 cm/hr

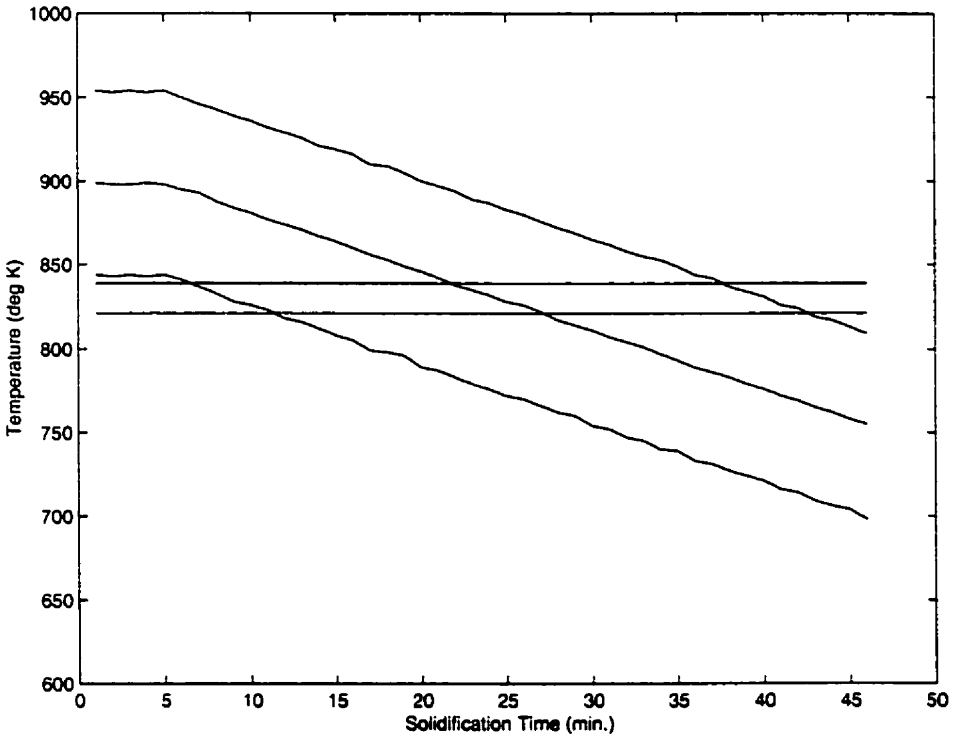

Figure 4. 4 Cooling Curve for Experiment #3, R=21 cm/hr

4.7 Experimental Results

The three samples were sectioned longitudinally to analyze along the direction of solidification. For all three experiments, development of the Al_2Cu primary θ phase was observed in a eutectic matrix, from the very beginning of solidification along the growth direction of the longitudinal sections. Figures 4.6-4.8 exhibit the longitudinal sections of the three experiments performed, and Figures 4.9-4.11 illustrate the transverse sections of the same samples. Most of the θ phase is aligned in a specific direction as a result of the unidirectional solidification process. The direction and size of the thermal gradient was controlled by the QUESTS furnace, and was parallel to the growth direction of the growing phase. Significant differences on the macroscopic level along the casts, as well as differences on the morphological scale were observed when comparing the longitudinal microstructures.

4.7.1 Macrostructure of the Specimens

The eutectic constituent was more dominant in the 6 cm/hr case near the top of the ingot (Figure 4.6c). The amount of eutectic in the final transient stage decreases as the solidification rate increases. Because the growth direction of the faceted phase is determined by specific crystallographic orientations and is not necessarily parallel to the

heat flux, irregular eutectic growth is observed in all three cases. For the 6 cm/hr case and 11 cm/hr case, directionality of the θ phase develops as solidification progresses, indicated by the orientation difference of the θ phase in the bottom and middle sections of Figure 4.6 and Figure 4.7. On the other hand, the 21 cm/hr case exhibits directionality immediately upon solidification, as is evident from all three longitudinal sections in Figure 4.8. Of significance at the macroscopic level is that there is no significant channels present in any of the longitudinal or transverse sections. In some cases, it was noticed that θ phase directionality turned toward the side walls. However, previous experimental research [4, 44] has indicated minimal channel formation for Al-40wt%Cu alloys solidified under similar conditions, where channel formation occurred only near side walls, and without significant length compared to the cast dimensions (see Figure 4.5).

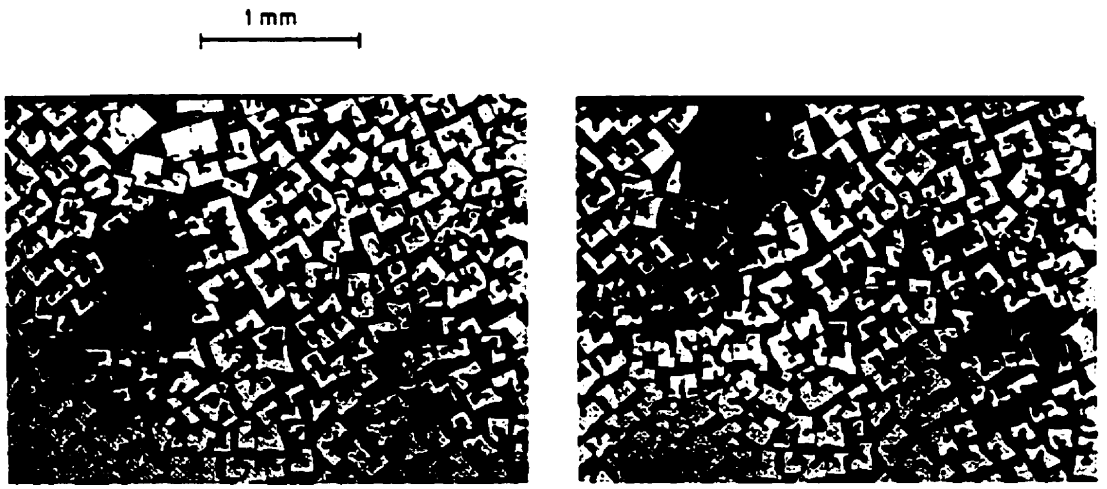

Figure 4.5 Channel segregates observed on cross-sections of the Al-40wt%Cu alloy solidified at R= 4.5 cm/hr. [44]

4.7.2 Morphology of the Specimens

The particles of θ phase become more elongated with increasing distance from the chill face, evident in all three cases by comparing bottom sections (Figure 4.6(a)-4.8(a)) to top section (Figure 4.6(c)-4.8(c)) of the same experiment. Along with an increase in elongation is an increase in facet tendencies as solidification progresses. Figure 4.8(a) exhibits rounded side branches near the bottom (start) of the cast, and fully developed facets at the top. This occurrence is not as prevalent for the 6 cm/hr case and 11 cm/hr case. For the 21 cm/hr case, it was found that dendrite arms were present near the bottom of the cast, but the dendrite arms disappeared with the progression of solidification (Figures 4.8a and 4.11a). The orientations of the primary θ phase near the bottom of the longitudinal samples are more random than those observed near the top of the ingots.

A comparison of the transverse structures, shows that all cases start with more rounded primaries which lead to a smooth faceted structure. The branching of side arms is diminished with advancement up the cast. Previous experiments [4] have compared the effect of solidification velocity on the morphology of hyper-eutectic Al-Cu alloys. It was found that as the growth rate increased, there was a tendency toward a more dendritic microstructure. These properties can also be observed in Figures 4.6-4.11. For instance, there is side branching of the longitudinal bottom sections as the solidification rate increases (Figure 4.6(a) —4.8(a)). The upper sections of Figures 4.9 to 4.11 exhibit progression from faceted to slightly-faceted primaries, while the middle sections reveal no

such trend. In the 21 cm/hr case, the bottom sections all remain rounded with slight side branching. Significant differences were observed regarding the distribution and size of θ phase primaries. With an increase in solidification, the distribution of θ phase becomes more uniform for transverse microstructures (6 cm/hr, and 11cm/hr case).

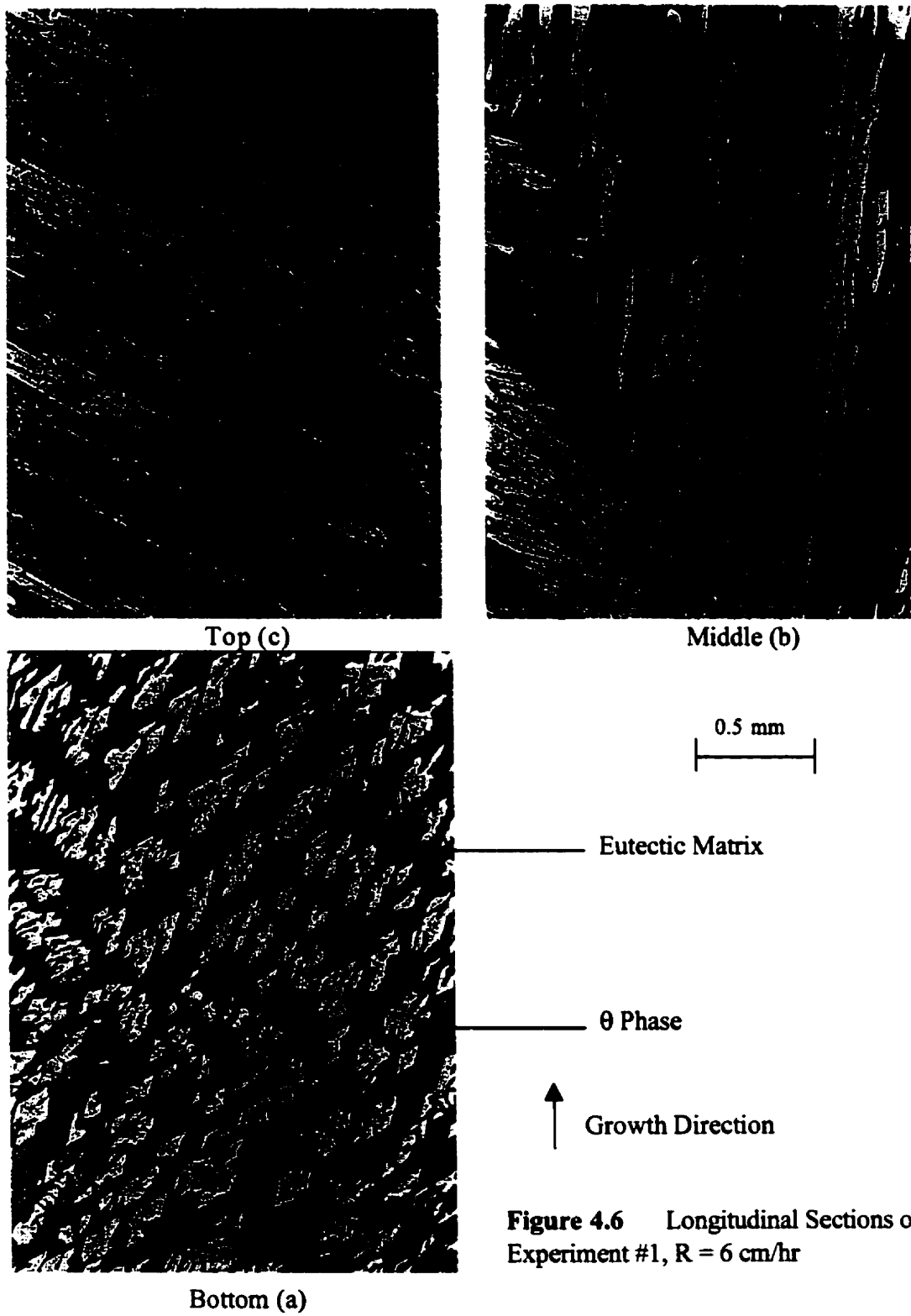

Figure 4.6 Longitudinal Sections of Experiment #1, R = 6 cm/hr

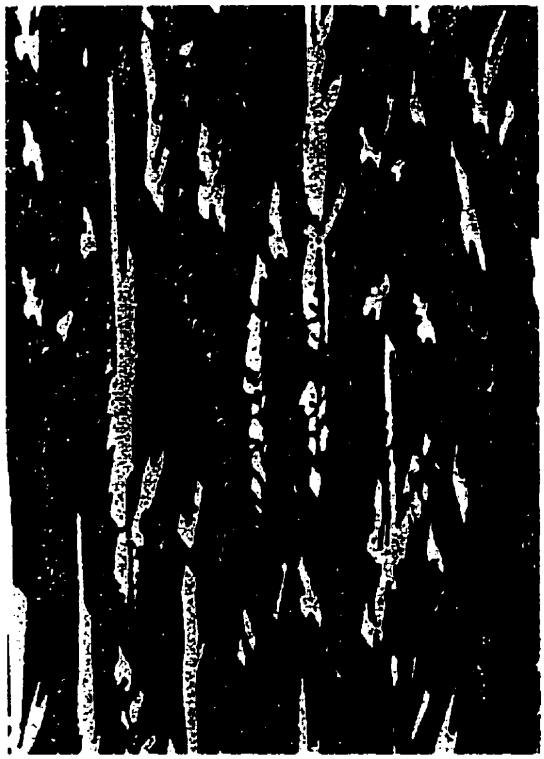

Top (c)

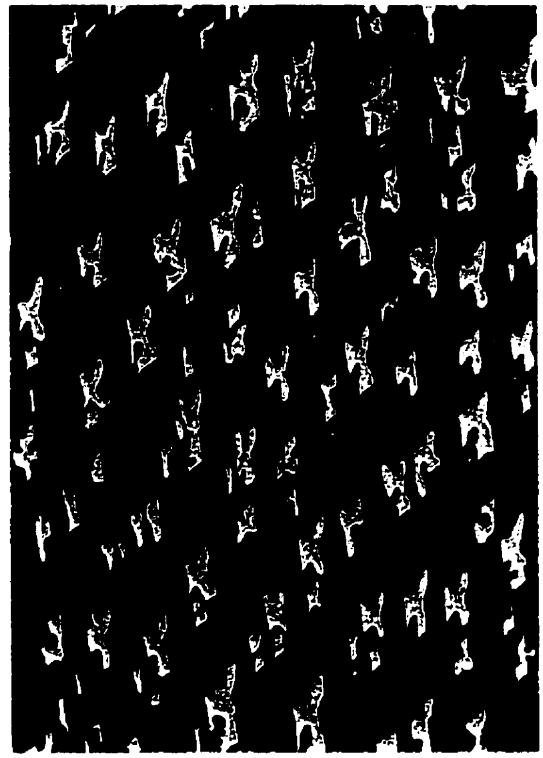

Middle (b)

Bottom (a)

0.5 mm

Growth Direction

Figure 4.7 Longitudinal Sections of Experiment #2, R = 11 cm/hr

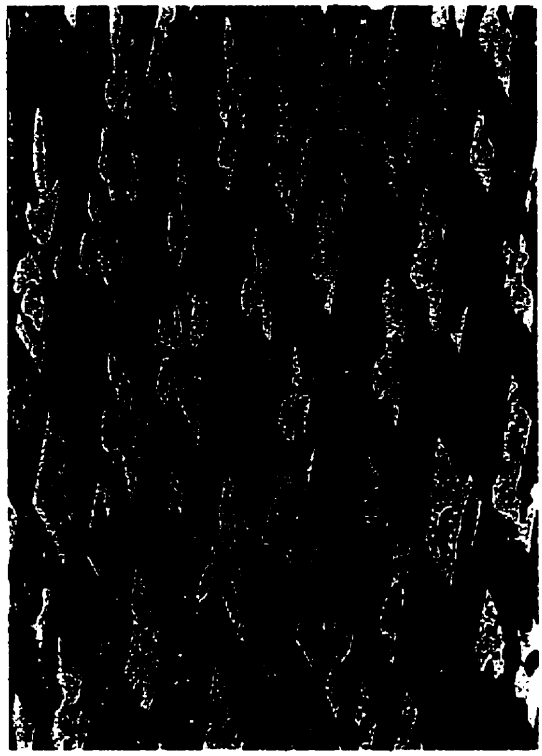

Top (c)

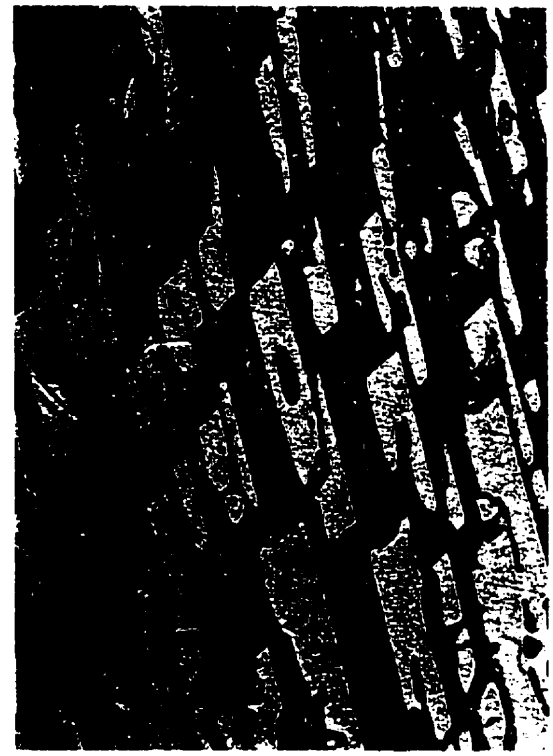

Middle (b)

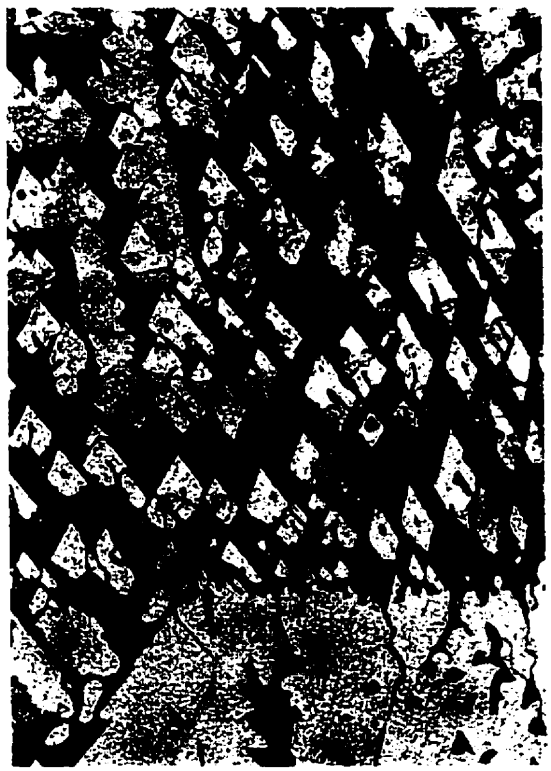

Bottom (a)

0.5 mm

Growth Direction

Figure 4.8 Longitudinal Sections of Experiment #3, R = 21cm/hr

0.5 mm

Top (c)

Middle (b)

Bottom (a)

Figure 4.9 Transverse Microstructures of the R=6cm/hr case

0.5 mm

Top (c)

Middle (b)

Bottom (a)

Figure 4.10 Transverse Microstructures of the R=11cm/hr case

0.5 mm

Top (c)

Middle (b)

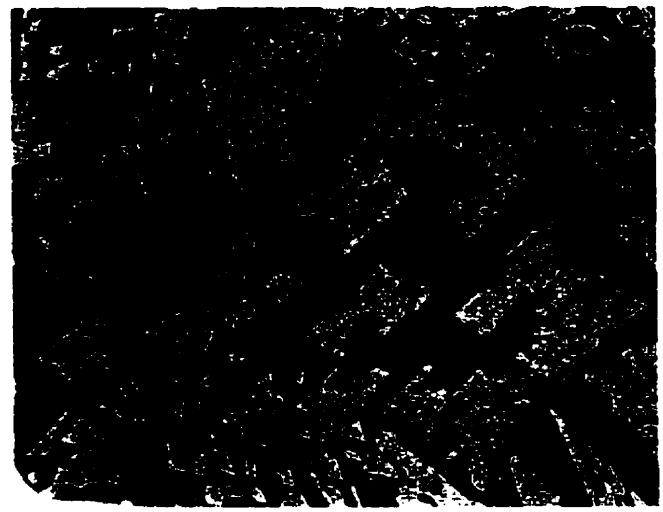

Bottom (a)

Figure 4.11 Transverse Microstructures of the R=21cm/hr case

4.7.3 Macrosegregation of the Specimens and Comparison to Simulations

For the experiments performed in this research, segregation data obtained experimentally and through simulation may be compared directly, as both methods produce segregation results which are easily quantifiable. In terms of the underlying structure of materials, the computer simulations neglect such aspects as grain structure, dendritic versus faceted growth, and the transition between the two. Simulations strictly focus on how fluid flow affects the solid/liquid interface morphology, and the effects leading to channel formation. To compare structures, the differences between composition, or the formation of channels is the only indicator.

4.7.3.1 Case #1: R=6 cm/hr

The macrosegregation data shown in Figure 4.12 illustrates the copper content as a function of the distance from the chill face, obtained by employing EDS analysis for the 6 cm/hr case, along with the simulation data from Chapter 3. Figure 4.13 compares macrosegregation data taken from the LEITZ image analyzer with data taken from EDS analysis. The results indicate that segregation of copper occurred. The solute (Cu) concentration is higher at the chill face and gradually decreases as the sample solidifies further. For the 6 cm/hr case, the copper content begins near 3wt%Cu above nominal, and constantly decreases until the solid/liquid interface advances 5 cm up the cast. At

that point, decreases drastically for the last half of solidification down to the eutectic composition.

The experimental and simulated data correspond very well in terms of the observed trend, except near the initial transient where the simulated data does not show a large increase in composition. Differences can be attributed to the limiting assumptions made by the numerical method in that there are no shrinkage effects taken into account, and all solid formations must remain stationary. As long as convective effects influence the solid/liquid interface, nucleation sites will flow into the bulk liquid altering the distribution of the θ phase throughout the cast. Overall, simulated and experimental results for the 6 cm/hr are in good agreement. Comparing EDS analysis with image analysis techniques in Figure 4.13 reveals that the two methods produce relatively equal results with more than 50% of data points in agreement. Similar trends between the two techniques are observed indicating maximum segregation values of 3.5 wt%Cu

During solidification, Al is rejected from the dendritic array. This causes a higher concentration of copper in regions that solidify earlier, as well as a decrease in bulk concentration. For the hyper-eutectic Al-Cu system, the first solidified θ phase is heavier than the bulk liquid. Gravity pulls the heavier phase down to the chill bottom, increasing the average composition of copper in the lower portions of the ingot. In the hyper-eutectic Al-Cu region, the interdendritic liquid becomes enriched in Al down to the eutectic composition (33.2wt%Cu). The density of the bulk liquid at the interface is

lower than the θ phase. Thus, there is a density inversion throughout the solid/liquid region that causes the less dense liquid to rise. Consequently, buoyancy effects lead to a higher copper content at the lower region of the ingot. Shrinkage effects tend to reverse the above effect, so the predominant cause of segregation depends on the observed phenomena.

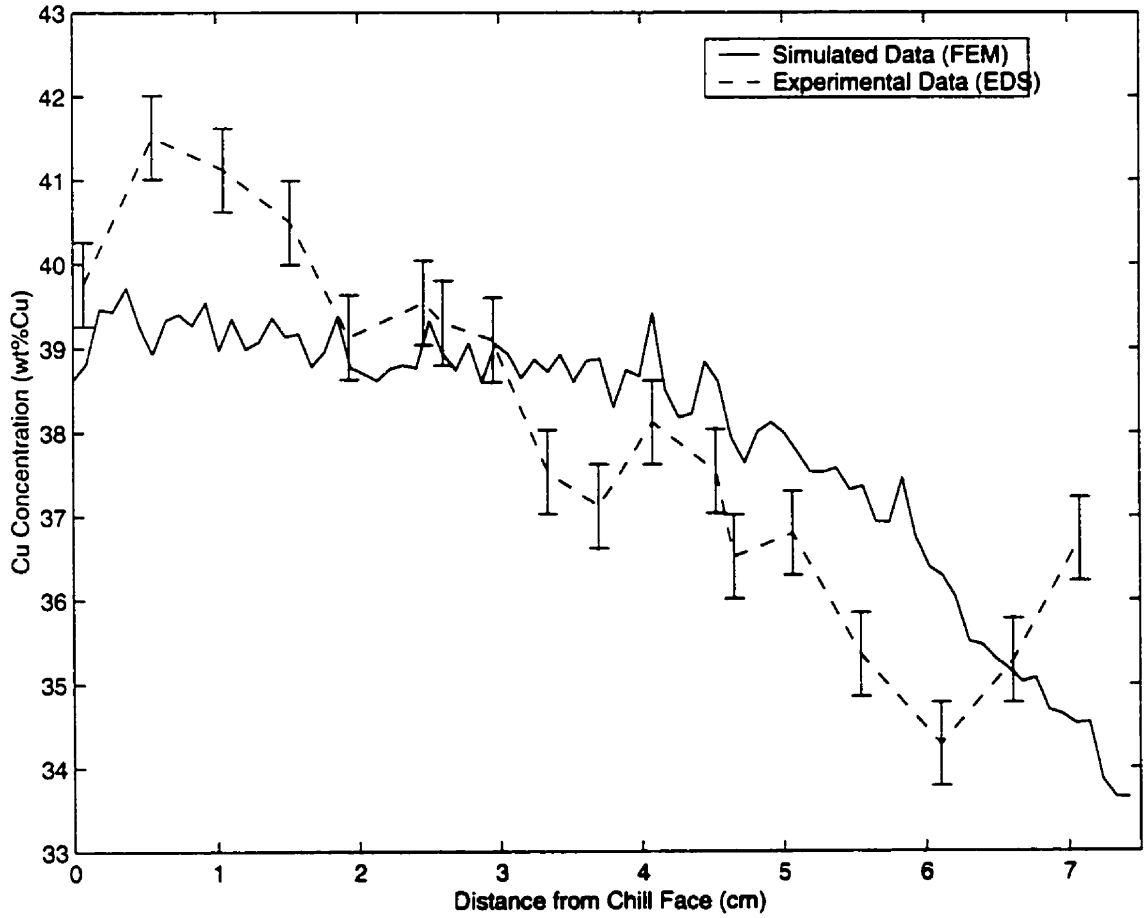

Figure 4.12 Comparison of Longitudinal Segregation between Numerical and Expermental Data, R=6cm/hr.

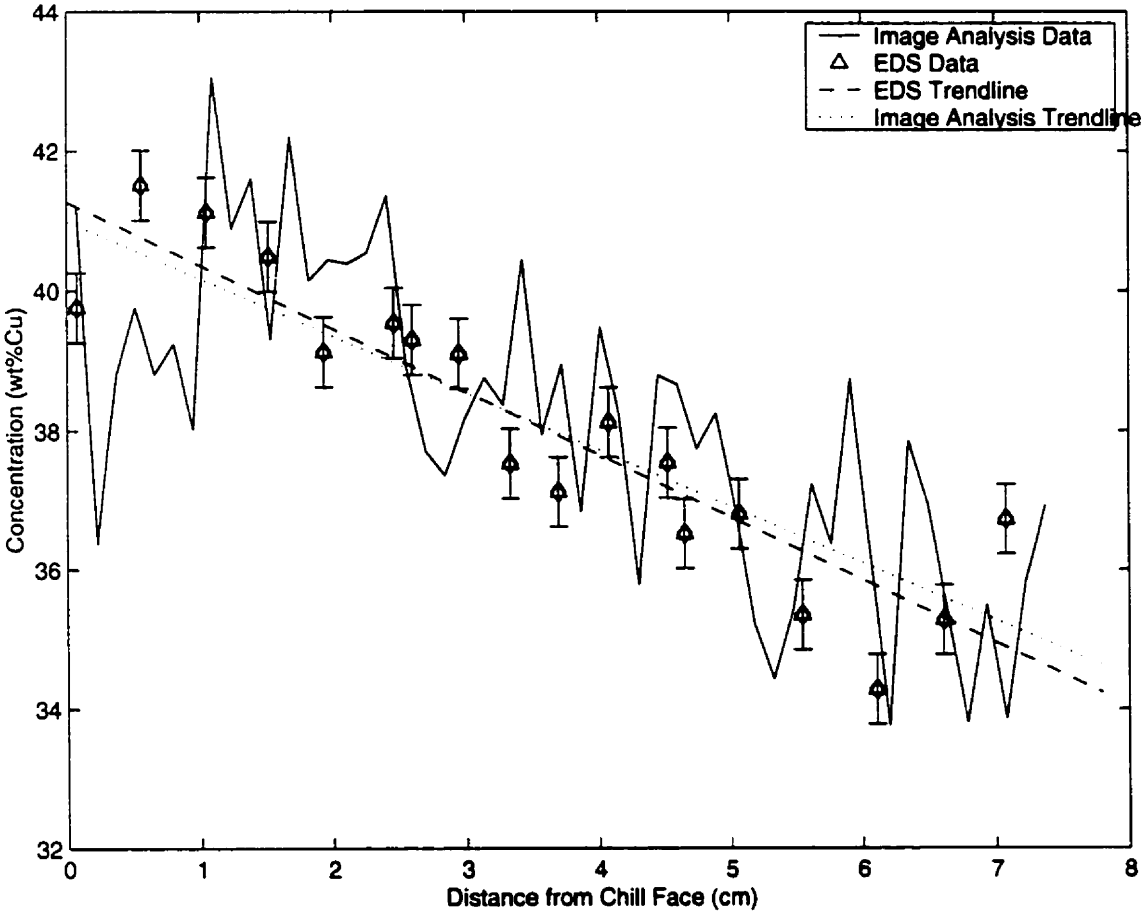

Figure 4.13 Comparison of longitudinal segregation between EDS analysis and image analysis, R = 6 cm/hr.

4.7.3.2 Case #2: R = 11 cm/hr

A comparison of simulated and experimental results for the 11 cm/hr case is shown in Figure 4.14. Figure 4.15 compares macrosegregation data taken from the LEITZ image analyzer with data taken from the EDS analysis. Figure 4.14 indicates maximum segregation values on the order of 3.5 wt%Cu,. As the growth rate increases, the amount of macrosegregation should decreases due to both gravity and buoyancy effects. Specifically, the amount of time available for the flow decreases with an increase in growth rate. The 6 cm/hr case and 11 cm/hr simulations possess similar velocity profiles, indicating that segregation effects due to convection will be of comparable proportions. Shrinkage and nominal composition differences may have played a role in the agreement of results.

The first noticeable difference is between the initial transient compositions. The simulated data reveals an initial transient difference of 2wt%Cu near 0.75 cm from the chill surface, while the experimental results show the exact same trend but further along the cast at 2 cm from the chill face. Another noticeable difference is the overall composition difference between the experimental and simulated data. The experimental values are generally lower by 0.5 —1.0wt%Cu. This may be due to a slightly lower nominal composition. In general, the data is comparable, especially near the end of solidification. Figure 4.15 reveals that more than 80% of data points are in agreement

between the EDS analysis and image analysis methods.

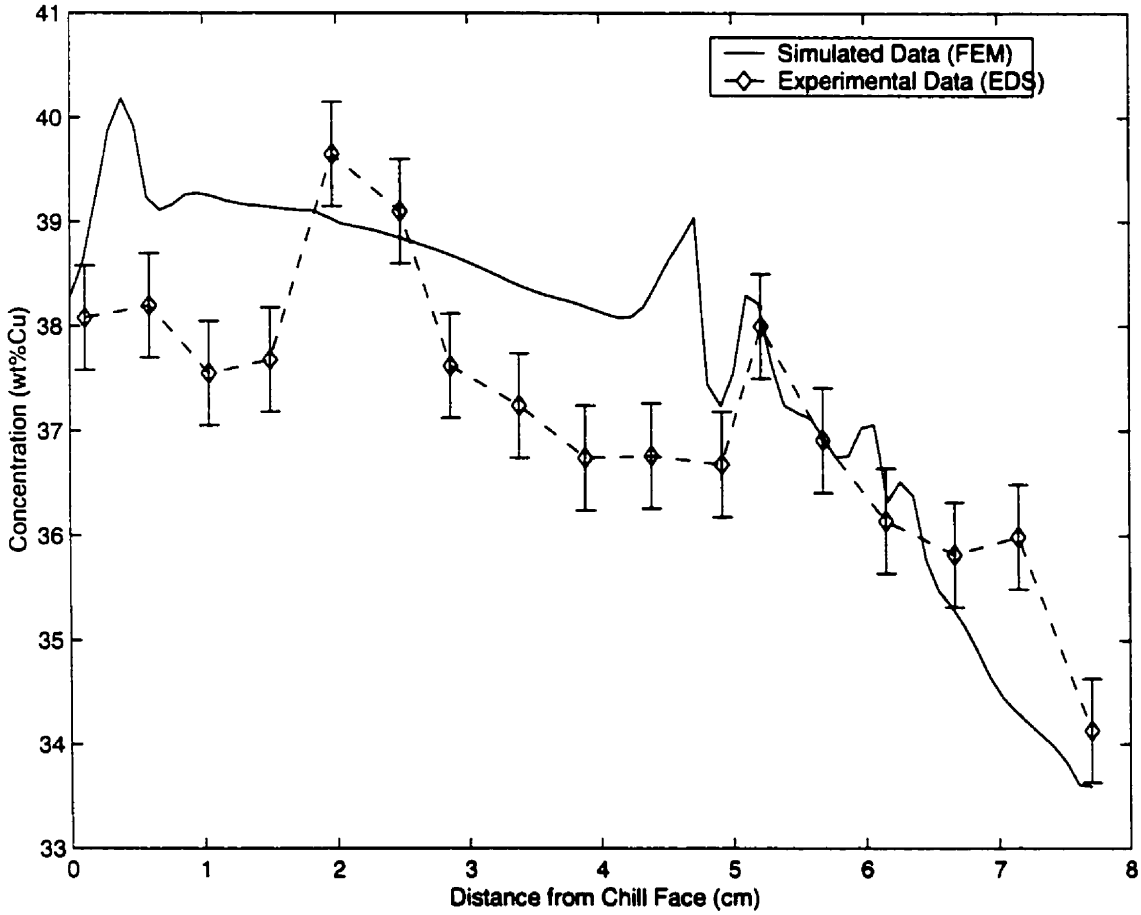

Figure 4.14 Comparison of Longitudinal Segregation between Numerical and Expermental Data, R=11cm/hr.

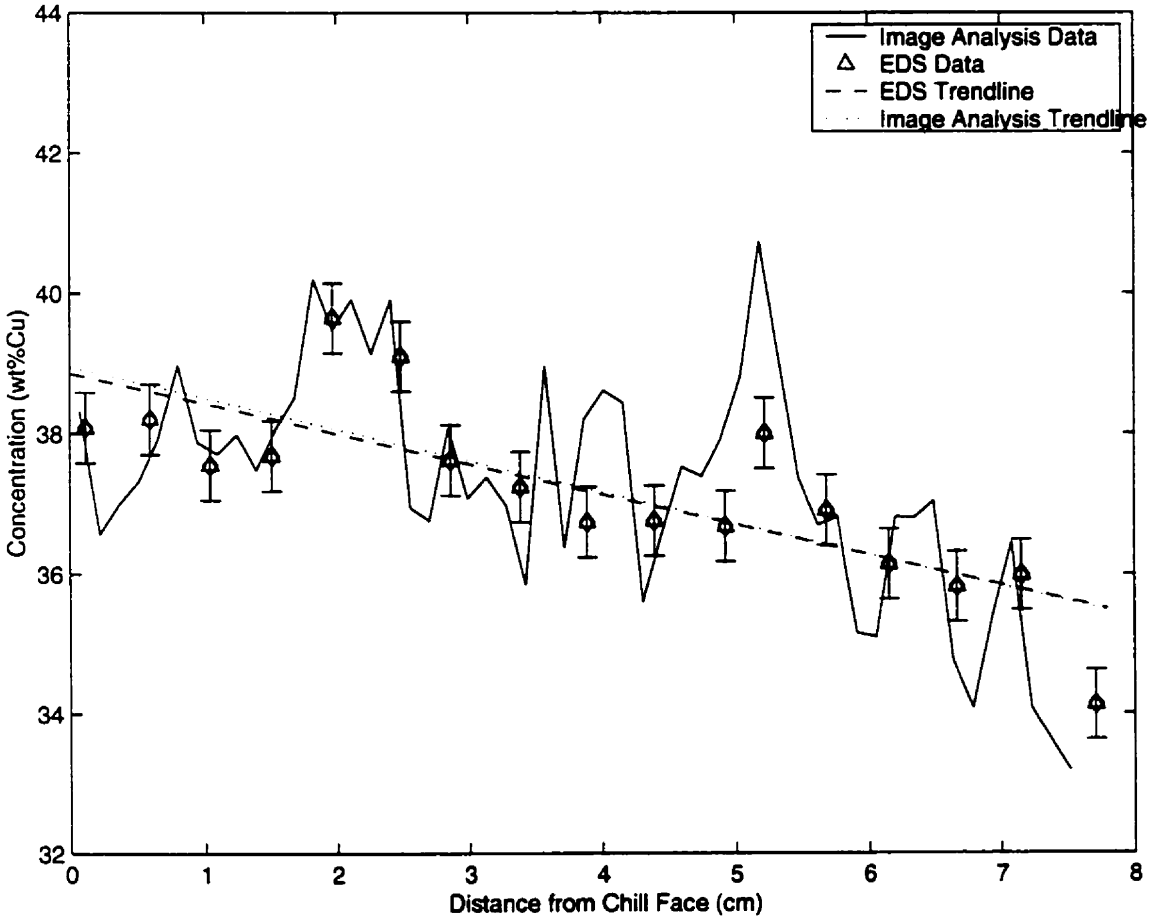

Figure 4.15 Comparison of longitudinal segregation between EDS analysis and image analysis techniques, R=11 cm/hr.

4.7.3.3 Case #3: R = 21 cm/hr

An increase in growth rate, of 21 cm/hr could have a pronounced effect on the longitudinal segregation. Figure 4.16 indicates the longitudinal segregation for experiment #3 along with simulated results from Chapter 3. Figure 4.17 compares macrosegregation data taken from the LEITZ image analyzer with data taken from the EDS analysis. Longitudinal segregation values fluctuate a great deal for the EDS plot, with compositions ranging between 34wt%Cu and 41wt%Cu, and no significant trend from the chill end to the top of the cast. A linear trendline comparison between the data indicates that the resulting longitudinal segregation is on the order of 1wt%Cu, a decrease over the other experiments, but within experimental error of the simulated data. Figure 4.17 shows good agreement between EDS analysis and image analysis techniques with more than 67% of data points falling within experimental error. Depending on the strength of convection and the amount of time for nucleation and growth of the θ phase, small nucleation sites may have moved into the bulk liquid by convection currents. This would result in a more even distribution of nucleation sites, and a lack of channel growth. As fluid flow becomes less prominent, the lack of convective cells allows larger dendrites to grow. The resulting change in growth morphology influenced the longitudinal segregation results along the ingot.

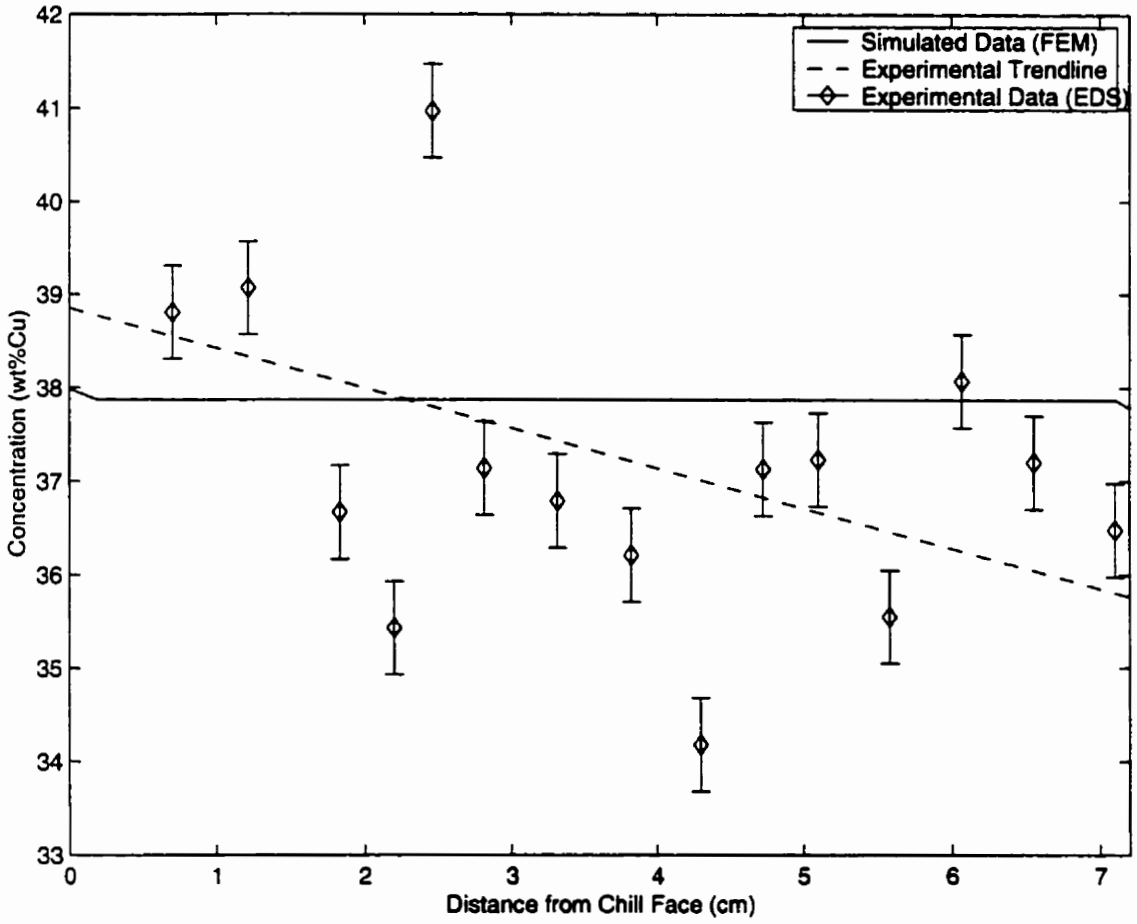

Figure 4.16 Comparison of Longitudinal Segregation between Numerical and Expermental Data, R=21cm/hr.

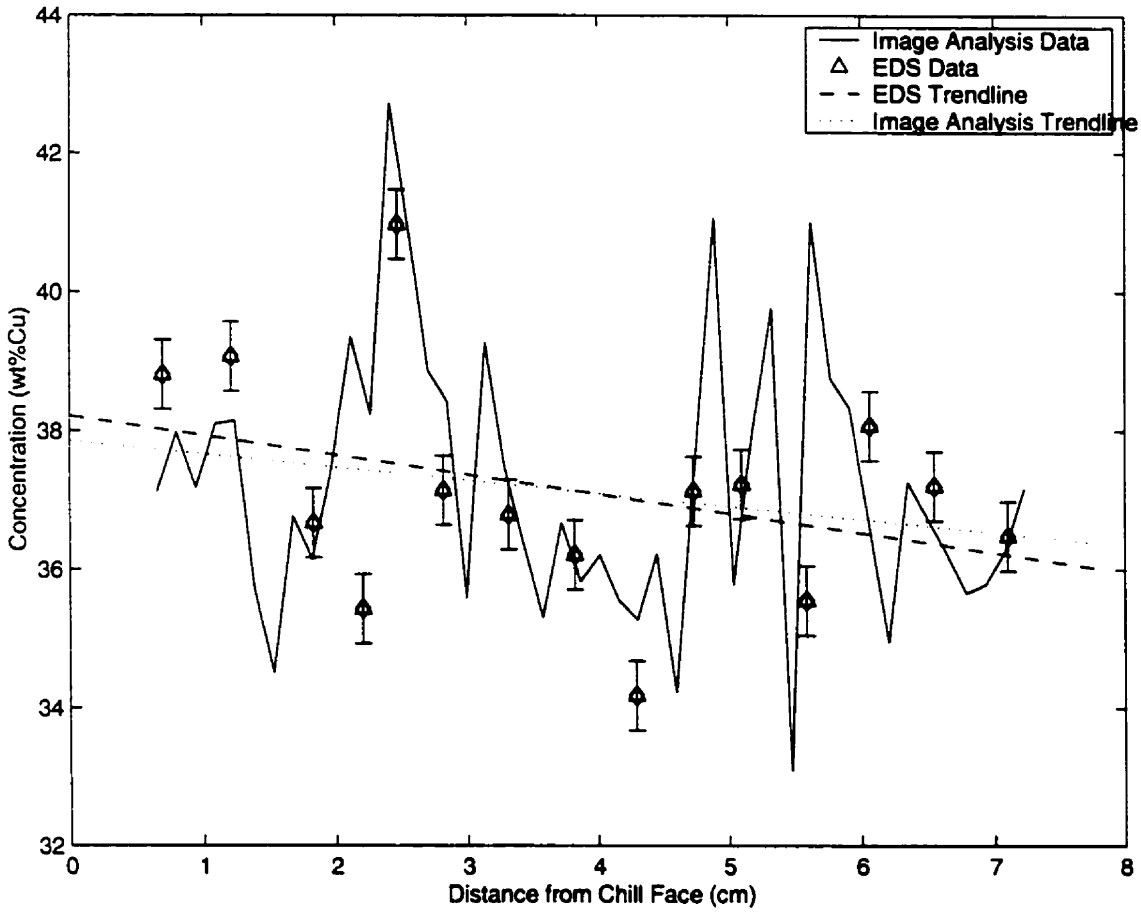

Figure 4.17 Comparison of longitudinal segregation between EDS analysis and image analysis techniques, R=21 cm/hr.

The maximum segregations for the experimental ingots solidified at rates of 6, 11, and 21 cm/hr are compared with the values calculated by computer simulation in Figure 4.18. The experimental results show a decrease in segregation between solidification rates of 11 and 21 cm/hr which generally agree with the simulation results. However, the experimental results indicate that for the 21 cm/hr ingot the maximum segregation remains at 1.5 wt%Cu while the simulated results for the same solidification rate indicates near 0wt% segregation. The simulation results do not consider the possibility of a lateral temperature gradient that, as demonstrated in the following section, can have a significant effect on the longitudinal concentration distribution.

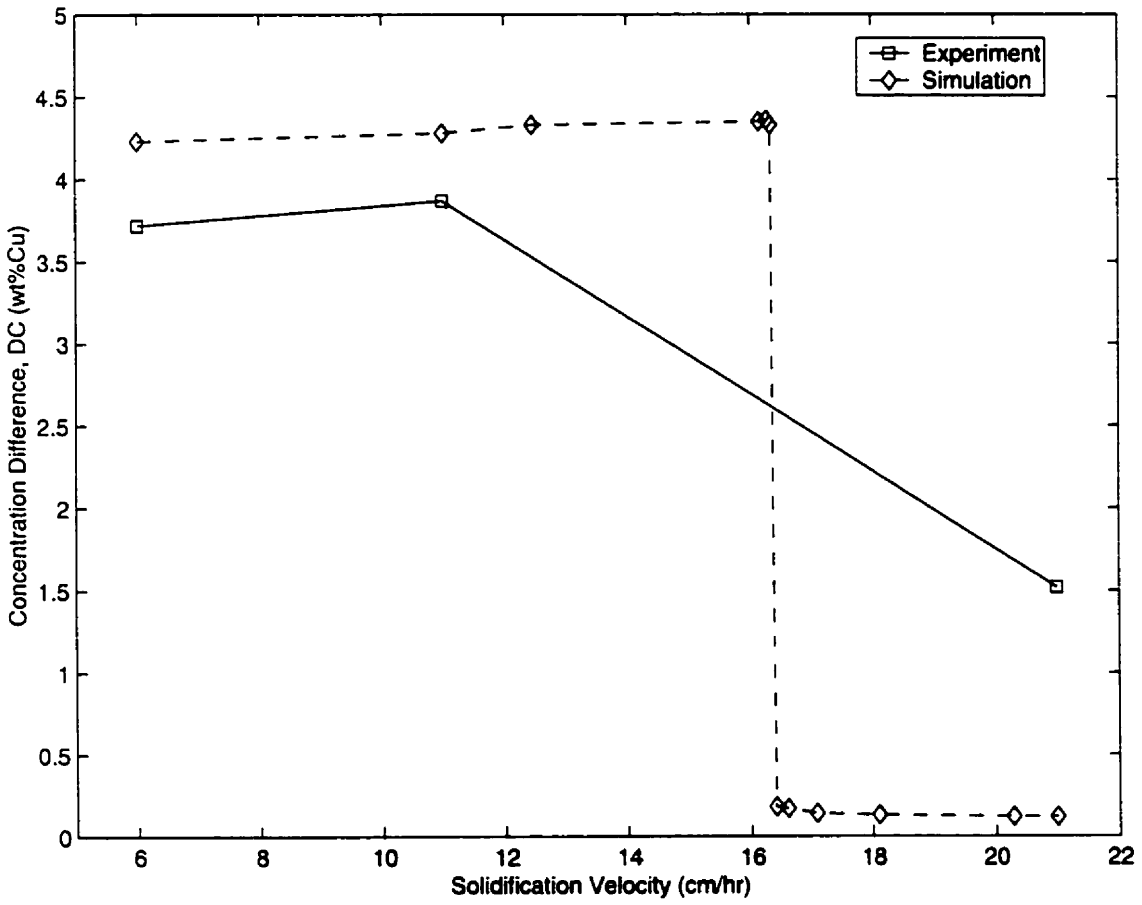

Figure 4.18 Maximum concentration difference between experimental and simulated results without a lateral temperature gradient applied.

4.7.3.4 Effect of Lateral Heat Flow

The effect of heat flow between the casting and the furnace is studied in the next examples. During actual solidification experiments, it is difficult to maintain perfectly insulated side walls. An arbitrary temperature gradient of 100 K/m was imposed at the side walls to simulate heat extraction from the mold. For all three simulations, the mushy zone adopts a convex shape towards the bulk liquid. An effect that may inhibit channel formation, and promote faceting. Side channel formation is delayed until further up the cast, and interior pockets are less pronounced than with the perfectly insulated cases. Comparing longitudinal segregation results with experimental data reveals that the segregation profile for the 6 cm/hr case remains relatively the same (Figure 4.19), while the 11 cm/hr case shows better correlation between results (Figure 4.20). Specifically, the initial transient of both experiment and simulation are of equal magnitude, while the slight shift in position may be due to shrinkage effects not taken into account by the simulation. The largest departure from previous simulation occurs with the 21 cm/hr case (Figure 4.21). The perfectly insulated case revealed no significant segregation or channel formation. Lateral heat flow effects have caused side wall channel formation in the upper portion of the cast, along with minor freckle formation in the interior of the mold. Lateral temperature gradients have a pronounced effect on the mushy zone of the 21 cm/hr case due to its large width compared to the 6 cm/hr and 11 cm/hr case. The 100 k/m temperature gradient may be overstated for the 21 cm/hr case since the faster

solidification rate may not allow such significant heat extraction to occur in such a short period of time.

Further simulations were performed to determine the effect of varying lateral temperature gradients on the final segregation profile for the 21 cm/hr case. Figure 4.22 compares maximum segregation versus increasing lateral temperature gradients. For applied lateral temperature gradients between 0 and 25 K/m, there is nearly no difference in longitudinal segregation compared to initial simulations where the effect of lateral temperature gradients were ignored. Between 25 K/m and 75 K/m, a significant increase in segregation is observed up to 2.5 wt%Cu. As the lateral temperature gradient is further increased beyond 100 K/m, maximum segregation gradually decreases. It is possible that the 21cm/hr experiment experienced a lateral temperature gradient near 50 K/m (only 0.5 K/cm) since EDS analysis techniques indicate maximum segregation values near 1.5 wt%Cu. Lateral temperature gradients near 200 K/m also produced longitudinal segregation values near 1.5 wt%Cu, but it seems unrealistic that such a significant gradient would occur during a well insulated, short duration experiment.

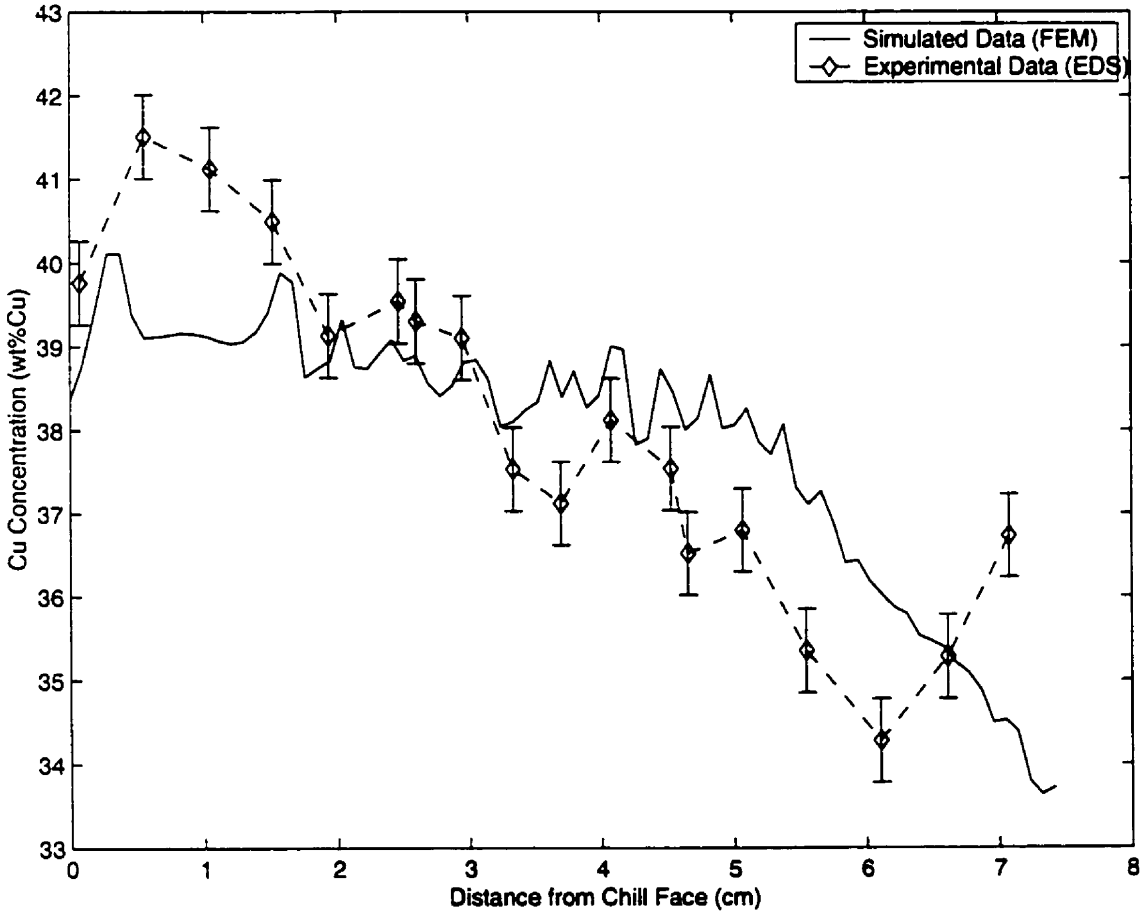

Figure 4.19 Comparison of longitudinal segregation between EDS analysis and modified simulation experiments with a lateral temperature gradient imposed on the side walls of 100 K/m, R=6 cm/hr.

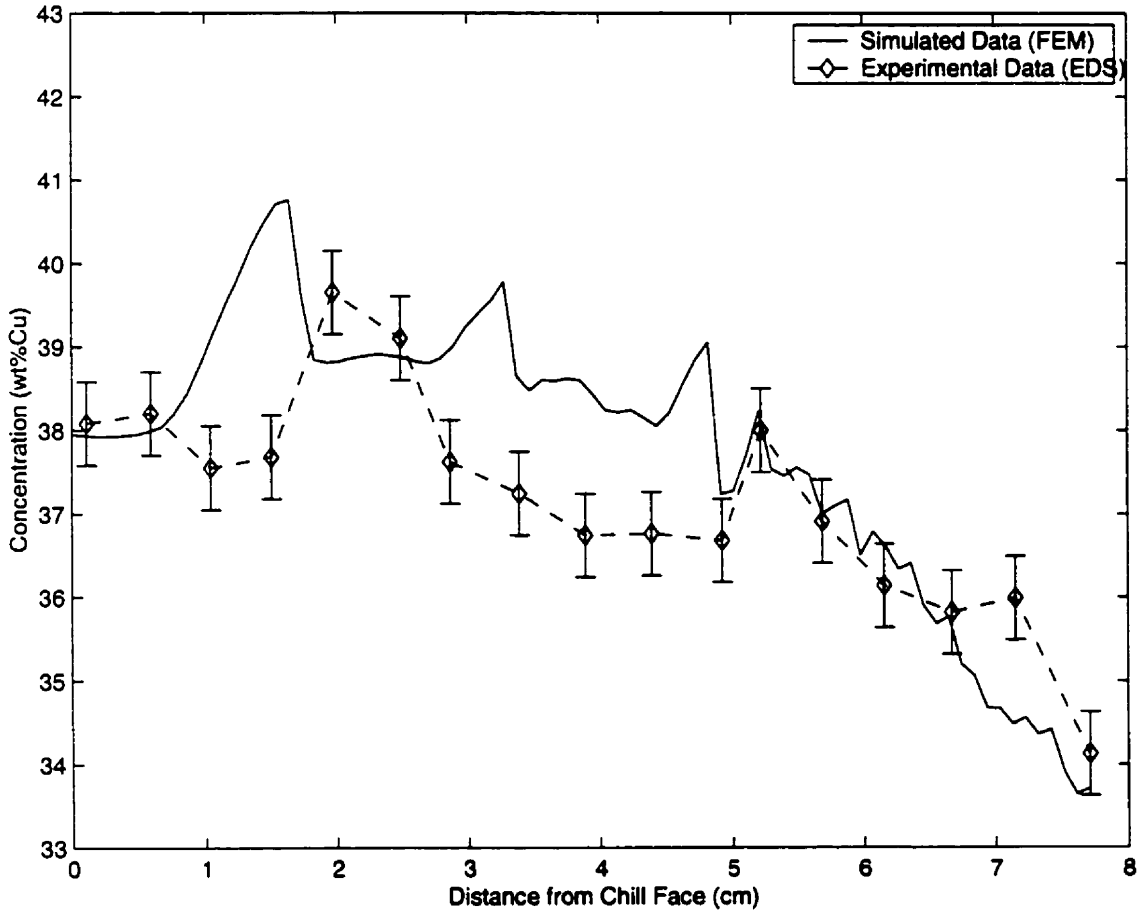

Figure 4.20 Comparison of longitudinal segregation between EDS analysis and modified simulation experiments with a lateral temperature gradient imposed on the side walls of 100 K/m, R=11 cm/hr.

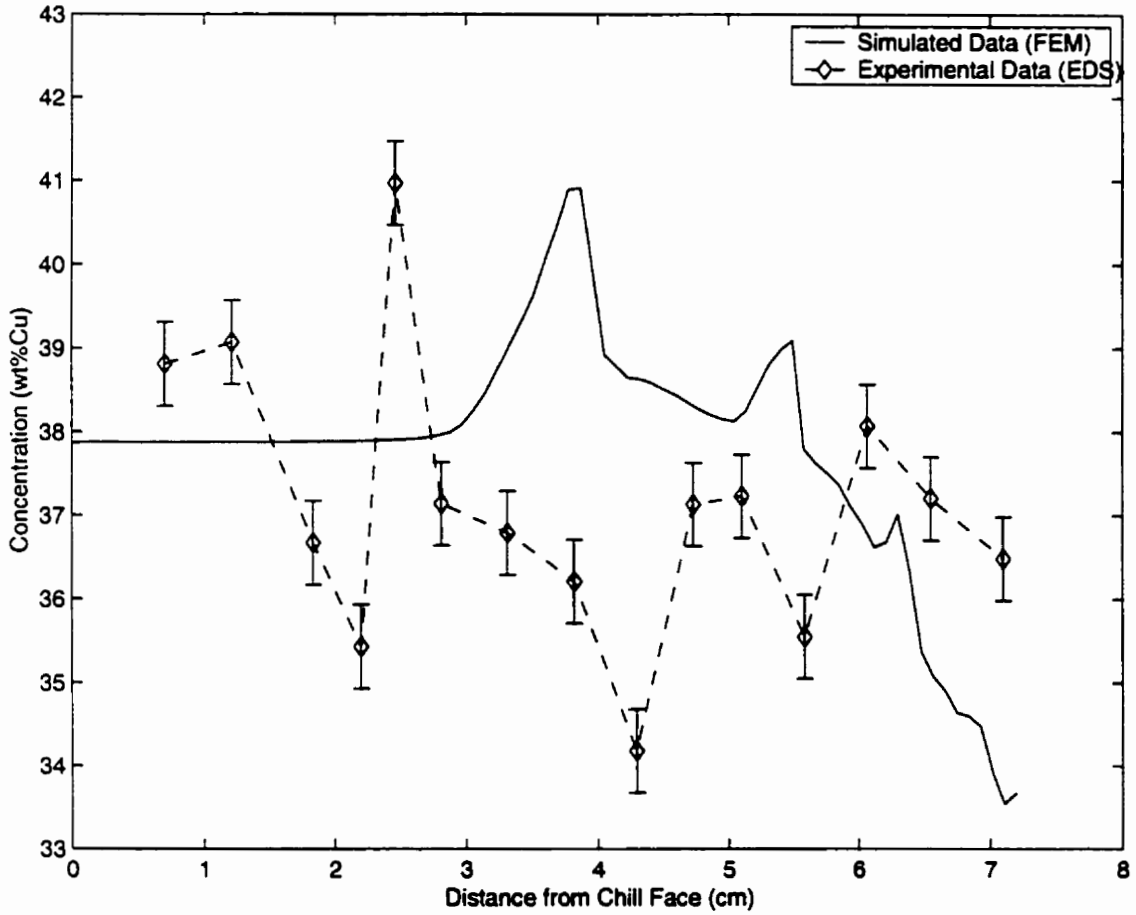

Figure 4.21 Comparison of longitudinal segregation between EDS analysis and modified simulation experiments with a lateral temperature gradient imposed on the side walls of 100 K/m, R=21 cm/hr.

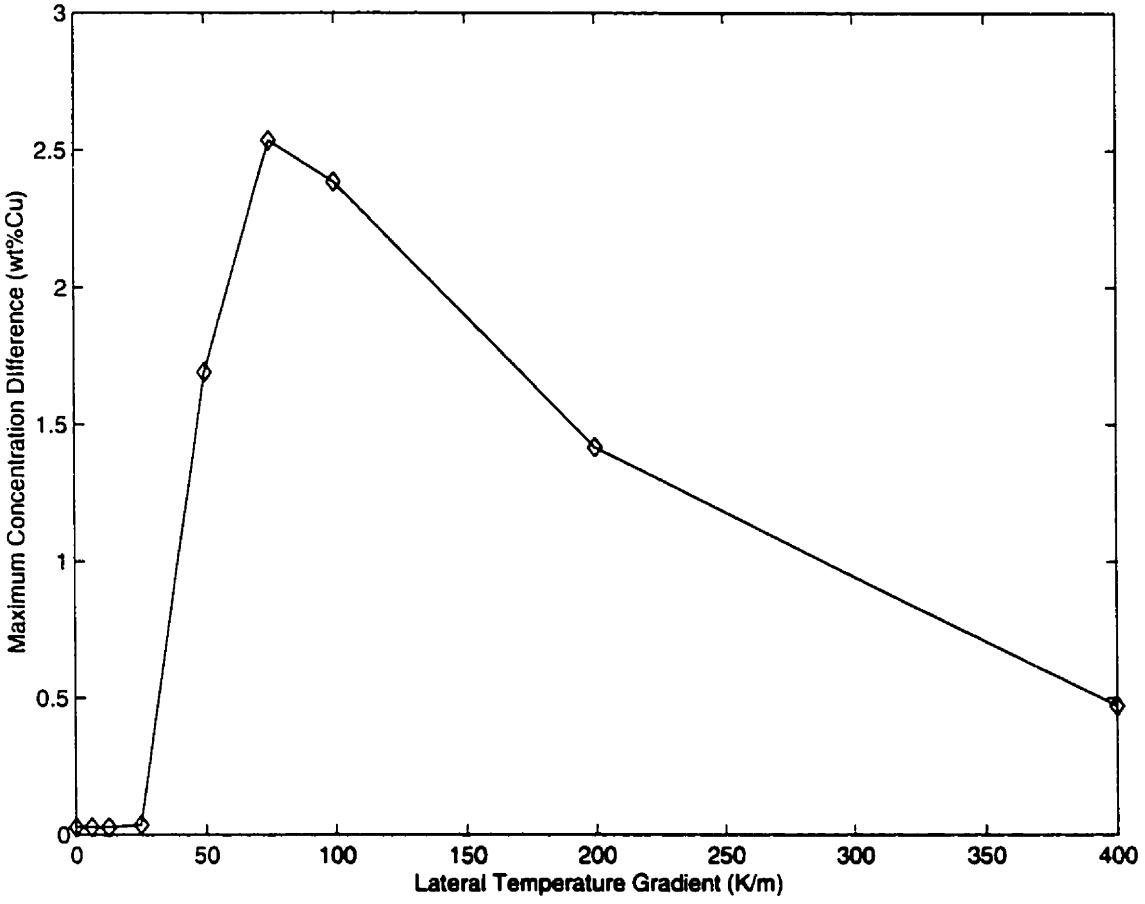

Figure 4.22 Maximum longitudinal segregation versus increasing lateral temperature gradient for the R= 21 cm/hr simulation.

4.7.3.5 Critical Velocity Determination

With an increase in the solidification velocity, the overall longitudinal segregation decreases, a trend observed in all three cases. Figure 4.23 shows the maximum segregation values established from both experimental and simulated results. The 6 cm/hr experiment exhibited maximum segregation values of 3.5wt%Cu, agreeing well with the simulated data. The 11 cm/hr experiment showed maximum segregation values on the order of 3.5wt%Cu, agreeing well with simulated results. Analysis of the 21 cm/hr experiment revealed maximum segregation values on the order of 1.5wt%Cu, while simulated segregation data revealed less than 0.5wt%Cu. This decrease can be attributed to altered gravity and buoyancy effects caused by an increase in growth rate. Although individual values fluctuated greatly, there was only a slight solute gradient along the cast. By employing a lateral temperature gradient of 50 K/m, the longitudinal segregation results for the 21 cm/hr case are in better agreement, with a significant increase in observed segregation. The overall results show that actual segregation trends do not decrease as drastically as the simulated data indicated. Future KC-135 research flights would benefit from experiments at thermal conditions between 11 cm/hr and 16 cm/hr.

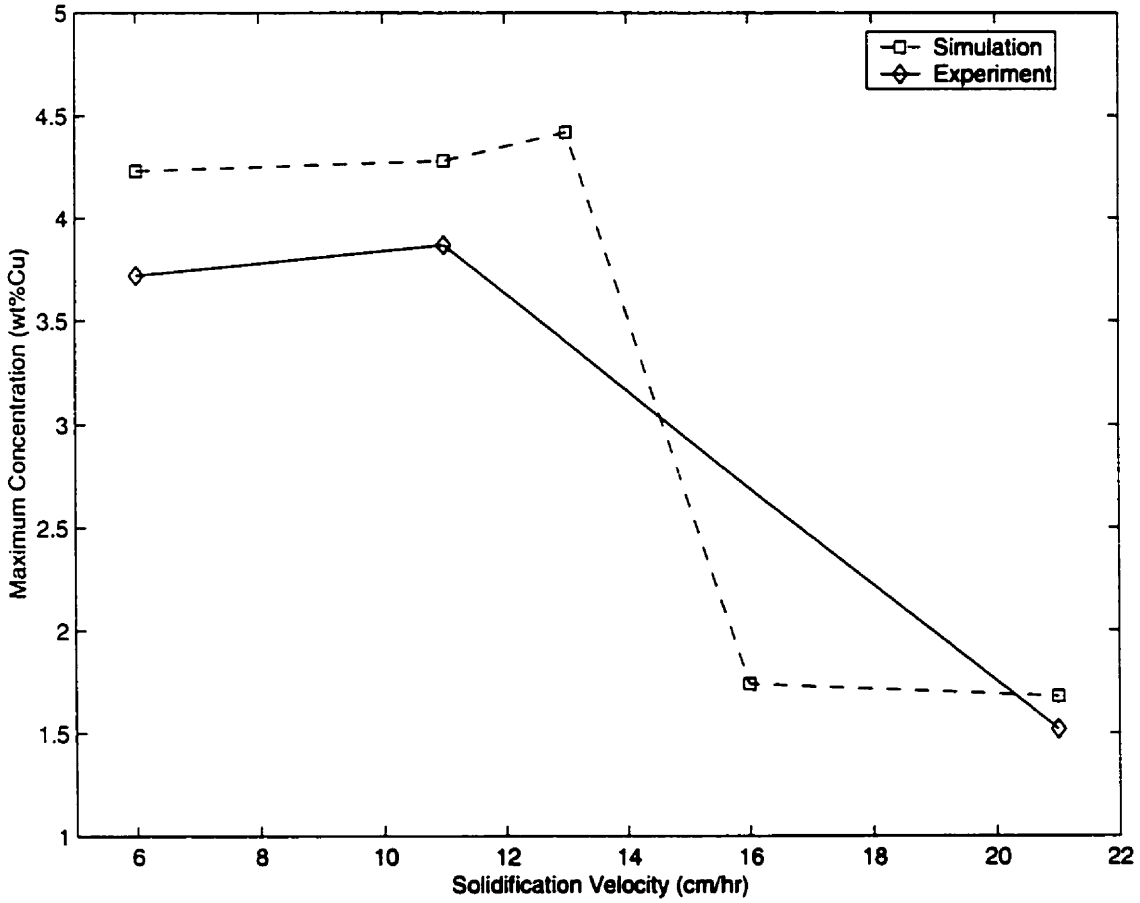

Figure 4.23 Maximum segregation vs. growth velocity for the simulated data (with lateral temperature gradient) as compared to the experimental results.

4.8 Forces Resulting from Fluid Flow

It has been suggested [48] that convective mixing in ground based experiments tend to break off the dendrite arms of the θ phase, and distribute them throughout the melt to provide nuclei for the growth of more θ phase particles. Convection induced shear flow was compared with the strength of the material by assuming that the force required to break the dendrites is comparable to that produced by the shear flow at the solid/liquid interface. Previous analysis have shown that calculated flow velocities of 1.0 x 10^{-4} m/s are insufficient to cause breakage of dendrite arms, and are far too weak to disrupt the bonding process during solidification [37]. Flow velocities used in the above analysis were approximated by,

$$V = \frac{\nu}{L}\left(\frac{Gr}{Sc}\right)^{1/2} \tag{4.1}$$

In equation (4.1), Sc is the Schmidt number given by [37],

$$Sc = \frac{\nu}{D_L} \tag{4.2}$$

and Gr of (4.1) is the Grashof number given by,

$$Gr = \frac{L^3 g \Delta\rho}{\rho \nu^2} \tag{4.3}$$

In equation (4.3) L is the characteristic system size taken as the primary dendrite arm spacing. Simulated data from Chapter 3 and experimental data from Chapter 4 show similar trends in segregation curves. Since actual flow velocities are difficult to calculate during solidification of liquid metals, the simulated flow data will be used to determine if dendrite detachment is possible for Al-Cu alloys under the solidification conditions presented here.

For upward vertical solidification in unit gravity, the solute rejected into the liquid from the Al_2Cu dendrites will reduce the density of the interface liquid and result in significant convective flows. For the simulated data, these flow patterns were observed at lower solidification rates (6 cm/hr and 11 cm/hr). The stress acting on a cylindrical dendrite arm of radius r and length, l=4r is given by [37],

$$\sigma_c = \frac{F_d r(l/2)}{\pi r^4/4} = \frac{122\nu\rho V}{r} \tag{4.4}$$

where F_d is the force acting on a cylindrical dendrite arm due to fluid flow.

By determining the shear flow at the solid/liquid interface for the three experiments in Chapter 3, an insight into the morphology and segregation results may be realized. All maximum velocity values occurred within 1 to 5 rows of the solid liquid interface; hence these velocities have a direct influence on the shape of the solid/liquid interface. The exact maximum velocity values along with the solidification times, and bending stress values as a function of dendrite radius are given in Table 4.2.

Table 4.2 Bending Stresses found using Maximum flow velocities from simulated experiments.

Solidification Rate, V [cm/hr]	Maximum Flow Velocity [m/s]	Bending Stress, σ [Pa]
6.0	3.75×10^{-3}	2200
11.0	3.59×10^{-3}	2100
21.0	8.77×10^{-5}	50

Even for dendrite arms with very small radius on the order of microns, this bending stress reaches only 2000 Pa, which is much less than the expected strength for Al_2Cu of about 50 MPa at high temperatures near the melting point [37]. Maximum velocity values are greater than previously calculated results by a factor of 10 for the 6 cm/hr and 11 cm/hr case. This difference proves to be insignificant since very small radii are still needed to produce significant bending stresses. Thus, hydrodynamic forces are insufficient to cause breakage of dendrite arms under the present solidification conditions. Convective mixing promoted the dilution of the melt at the interface and increased the instability. Since the growth of the θ phase is diffusion controlled, increased convective mixing favors the formation of a faceted morphology.

CHAPTER V

CONCLUSIONS

The solidification behavior of hyper-eutectic Al-38wt%Cu alloy was experimentally examined under various solidification conditions. Concurrently, numerical calculations were performed using a mathematical model of dendritic solidification of alloys subjected to thermosolutal convection. The following conclusions have been drawn from simulation results:

(a). Channels form during the growth of the mushy zone under solidification conditions with growth rates less than 16 cm/hr. The shape of the channels varies from small pockets of interdendritic liquid near the center of castings, to long penetrations at the cast walls.

(b). Channels are suppressed near the bottom of castings when lateral temperature gradients are applied to the cast; due in part to the convex solid/liquid interface morphology relative to the bulk liquid.

(c). The liquid within the channels is depleted in solute, resulting in considerable segregation after complete solidification.

(d). The convection is driven mainly by the solute field (as opposed to the thermal field), where solute accumulation produces potential channels of upward flow.

Experimental results revealed the following:

(e). The morphology of the Al_2Cu primaries showed a transition from non-faceted to faceted crystals with decreasing growth rate.

(f). The presence of convective mixing at lower growth rates increased instability of the solid/liquid interface, promoting the faceted θ phase morphology.

(g). The movement of nucleation sites due to natural convection may account for the lack of channels observed in experiments as compared to simulation.

(h). Longitudinal macrosegregation decreased with increasing growth rate due to gravity, phase change effects, and buoyancy effects. Segregation results for both experiment and simulation are in agreement on a macroscopic level at lower growth rates.

In the future, development of the numerical model should be expanded to include a number of effects including shrinkage, nucleation site distribution into the melt, and the

effect of faceted structures. A three-dimensional model has been developed in an attempt to quantify freckle size and channel dimensions, but is restricted to domain sizes much smaller than in this study. Determining experimental conditions where channel growth in Al-38wt%Cu is dominant would highly benefit comparisons with simulation. Segregation studies would benefit from future KC-135 research flights to compare solidification parameters in the "transition zone" between 11 cm/hr and 16 cm/hr. A better understanding of gravity effects could be included in the numerical model.

REFERENCES

1. S.D. Felicelli, J.C. Heinrich, and D.R. Poirier, *Numerical Heat Transfer, Part B*, 23, (1993), pp. 461-481.

2. S.D. Felicelli, D.R. Poirier, A.F. Giamei, and J.C. Heinrich, *JOM*, 49 no. 3, (1997), pp. 21-25.

3. S.D. Felicelli, D.R. Poirier, and J.C. Heinrich, *Metall. Trans B*, 29B, (1998), pp. 847-855.

4. H. Yu: *Master's Thesis*, University of Manitoba, Winnipeg, MB, Canada, (1993).

5. W. Kurz, and D.J. Fisher, *Fundamentals of Solidification*, 4th Ed. Trans Tech Pub., Switzerland, (1998).

6. R. Elliot, *Eutectic Solidification Processing*, Butterworths & Co, Toronto, Canada., (1983).

7. M.B. Thaddeus, Ed., *Binary Alloy Phase Diagrams*, vol. 1, Metals Park, Ohio, USA, (1986), p.106.

8. M.C. Flemings, *Solidification Processing*, McGraw-Hill, New York, NY, (1974).

9. G. Horvay, and J.W. Cahn, *Acta. Metallurgica*, 9, (1961), p.695.

10. G.E. Nash, and M.E. Glicksman, *Acta. Metallurgica.*, 22, (1974), p.1283.

11. J.D. Hunt, and S-Z Lu, *Metall. and Mater. Trans. A*, 27A, (1996), p.611.

12. R. Trivedi, *Metall. and Mater. Trans. A*, 15A, (1984), p.977.

13. D. Bouchard, and J.S. Kirkaldy, *Metall. and Mater. Trans. B*, 28B, no. 4, (1997), pp. 651-663.

14. T.Z. Kattamis, and M.C. Flemings, *Trans. Metall Soc.*, AIME, 233, (1965), p.

992,

15. H.D. Keith, and F.J. Padden, *Journal Appl. Phys.*, 31, (1963), p.1165.

16. K.A. Jackson, *Liquid Metals and Solidification*, ASM International, Cleveland, USA, (1958), p.174.

17. J.W. Cahn, *Acta. Metallurgica.*, 8, (1960), p. 554.

18. Temkin, D.E., in *Molecular roughness of the crystal melt boundary crystallization process*, eds N.N. Sirota, F.K. Gorski and V.M. Varikash, Consultants Bureau, New York (1966)

19. Camel, D., Lesault, G. and Eustathopoulous, N., *J. Crystal Growth*, 53, (1981), p.327.

20. K.A. Jackson, and J.D. Hunt, *Trans. AIME*, 236, (1966), p. 1129.

21. W.J. Boettinger, *in Metals Handbook 9th Ed.*, Vol. 9, ASM International, Metals Park, Ohio, (1985), pp. 611-617.

22. T.F. Bower, H.D. Brody, and M.C. Flemings, *Trans. AIME*, 236, (1966), p. 624.

23. R. Trivedi, and W. Kurz, *in Metals Handbook, 9th Ed.*, Vol. 15, ASM International, Metals Park, Ohio, (1985), pp. 114-136.

24. T.W. Clyne, and W. Kurz, *Metall. Trans. A*, 12A, (1981), p. 965.

25. S. Kobayashi, *Trans. of the Iron and Steel Institute of Japan*, 28, (1988), p. 728.

26. I. Ohnaka, *in Metals Handbook, 9th Ed.*, Vol. 15, ASM International, Metals Park, Ohio, (1985), pp. 136-141.

27. E. Scheil, *Metallforschung*, 2, (1947), p.69.

28. J.S. Kirkaldy, and W.V. Youdelis, *Trans. TMS-AIME*, 212, (1958), p.833.

29. M.C. Flemings, and G.E. Nereo, *Trans. TMS-AIME* ,239, (1967), p. 1449.

30. M.C. Flemings, R. Mehrabian, and G.E. Nereo, *Trans. TMS-AIME* , 242, (1968), p. 41.

31. M.C. Flemings, and G.E. Nereo, *Trans. TMS-AIME* , 242, (1968)p.50, (1968).

32. J.R. Cahoon, *Mat. Sci. and Eng.*, A188, (1994), pp.211-217.

33. A.V. Reddy, and C. Beckermann, *Metall. and Mater. Trans. B*, 28B, no. 3, (1997), pp.479-489.

34. S. Chang, and D.M. Stefanescu, *Acta. Mater.*, 44, no.6, (1996), pp.2227-2235.

35. H. Kato and J.R. Cahoon, *Metall. and Mater. Trans. A*, 16A, (1985), p.579.

36. M.D. DuPouy, D. Camel, and J.J. Favier, *Acta. Metallurgica*, 37, no. 4, (1989), pp.1143-1157.

37. Y. Hong, K.N. Tandon, and J.R. Cahoon, *Metall. and Mater. Trans. A*, 28A, (1997), p.1245.

38. J.R. Cahoon, M.C. Chaturvedi, and K.N. Tandon, *Metall. and Mater. Trans. A*, 29A, (1998), p.1101.

39. S.N. Ojha, G. Ding, Y. Lu, J. Reye, and S.N. Tewari, *Metall. and Mater. Trans. A*, 30A, (1999), p.2167.

40. S.D Felicelli: *Ph.D. Thesis*, University of Arizona, Tuscon, AZ, USA, (1991), p. 72.

41. J.R. Sarazin and A. Hellawell, *Metall. Trans A*, 19A, (1988), pp. 1861-71.

42. C.Y. Wang, and C. Beckermann, *Metall. Trans A*, 27A, (1996), pp. 2765-2783.

43. S. Chang, and D.M. Stefanescu, *Metall. Trans. A*, 27A, (1996), pp. 2708-2721.

44. DuPouy, D. Camel, and J.J. Favier, *Acta Metallurgica.*, 37(4), (1989), pp.1143-1157.

45. S. Ganesan, R. Speiser, and D.R. Poirier, *Metall. Trans. B*, 18B, (1987), pp.421-424.

46. H.W. Huang, J.C. Heinrich, and D.R. Poirier, *Numerical Heat Transfer: Part A*, 29, (1996), pp.639-644.

47. G.B. McFadden, R.G. Rehm, S.R. Coriell, W. Chuck, and K.A. Morrish, *Metall. Trans A.*, 15A, (1984), pp. 2125-2137.

48. W.A. Tiller and S.O. O'Hara, *The Solidification of Metals*, Iron and Steel Institute, London, (1967), p.27.

APPENDIX A

ANALYTICAL MICROSEGREGATION SOLUTION

The following analytical solution has been proposed by Kobayashi [28] as an exact solution to the microsegregation problem,

$$C_s = kC_0\xi^n\left\{1+U\left[\frac{1}{2}\left(\frac{1}{\xi^2}-1\right)-2\left(\frac{1}{\xi}-1\right)-\ln\xi\right]\right\} \tag{A.1}$$

where the parameters ξ, β, γ, η and U are defined as follows,

$$\xi = 1-(1-\beta k)f_s$$

$$\beta = \frac{2\gamma}{(1+2\gamma)}$$

$$\gamma = \frac{8D_L t_f}{\lambda^2}$$

$$\eta = \frac{(k-1)}{(1-\beta k)}$$

$$U = \frac{\beta^3 k(k-1)\left[(1+\beta)k-2\right]}{4\gamma(1-\beta k)^3}$$

APPENDIX B

GOVERNING EQUATIONS USED BY THE FINITE ELEMENT PROGRAM

X-momentum equation

$$Pr\frac{\partial u}{\partial t} + \frac{1}{\phi}\left(u\frac{\partial u}{\partial x} + w\frac{\partial u}{\partial z}\right) = -\phi\frac{\partial p}{\partial x} + Pr\left(\frac{\partial^2 u}{\partial x^2} + \frac{\partial^2 u}{\partial z^2}\right) - \phi\frac{Pr}{Da_x}u - \phi\cos\theta\, Pr\left[R_T T + \frac{R_S}{Sc}(C_l - 1)\right] \quad \text{(B.1)}$$

Z-momentum equation

$$Pr\frac{\partial w}{\partial t} + \frac{1}{\phi}\left(u\frac{\partial w}{\partial x} + w\frac{\partial w}{\partial z}\right) = -\phi\frac{\partial p}{\partial z} + Pr\left(\frac{\partial^2 w}{\partial x^2} + \frac{\partial^2 w}{\partial z^2}\right) - \phi\frac{Pr}{Da_z}w - \phi\sin\theta\, Pr\left[R_T T + \frac{R_S}{Sc}(C_l - 1)\right] \quad \text{(B.2)}$$

Continuity equation

$$Pr\frac{\partial T}{\partial t} + u\frac{\partial T}{\partial x} + w\frac{\partial T}{\partial z} = \frac{\partial^2 T}{\partial x^2} + \frac{\partial^2 T}{\partial z^2} - \overline{L}\frac{\partial \phi}{\partial t} \quad \text{(B.3)}$$

Energy equation

$$\frac{\partial u}{\partial x} + \frac{\partial w}{\partial z} = 0 \quad \text{(B.4)}$$

Solute concentration

$$Pr\frac{\partial \overline{C}}{\partial t} + u\frac{\partial C_l}{\partial x} + w\frac{\partial C_l}{\partial z} = \frac{Pr}{Sc}\left(\frac{\partial}{\partial x}\phi\frac{\partial C_l}{\partial x} + \frac{\partial}{\partial z}\phi\frac{\partial C_l}{\partial z}\right) \quad \text{(B.5)}$$

Latent Heat

$$\hat{L} = \frac{L}{m\,\hat{c}\,C_0} \quad \textit{and} \quad \overline{L} = \frac{L}{\hat{c}G_R\,H} \tag{B.6}$$

APPENDIX C

LONGITUDINAL SEGREGATION PROFILES FROM FEM ANALYSIS

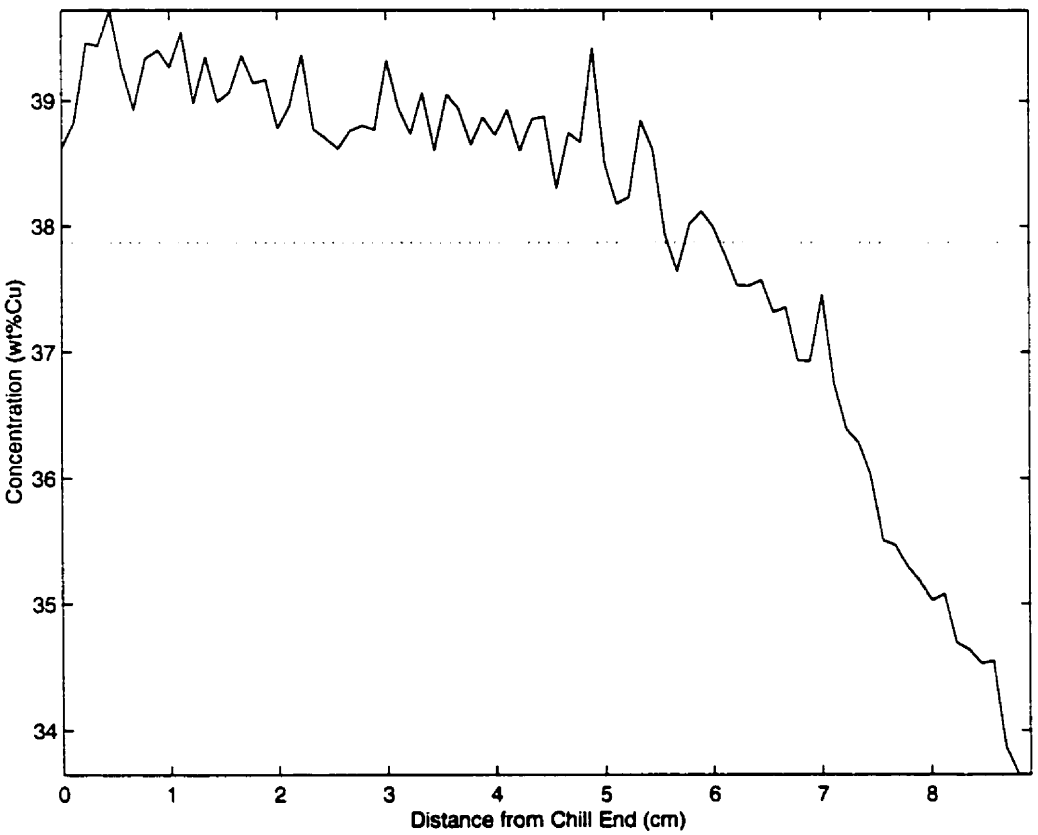

Figure C.1 Longitudinal segregation of the Al-38wt%Cu alloy solidified at R=6cm/hr.

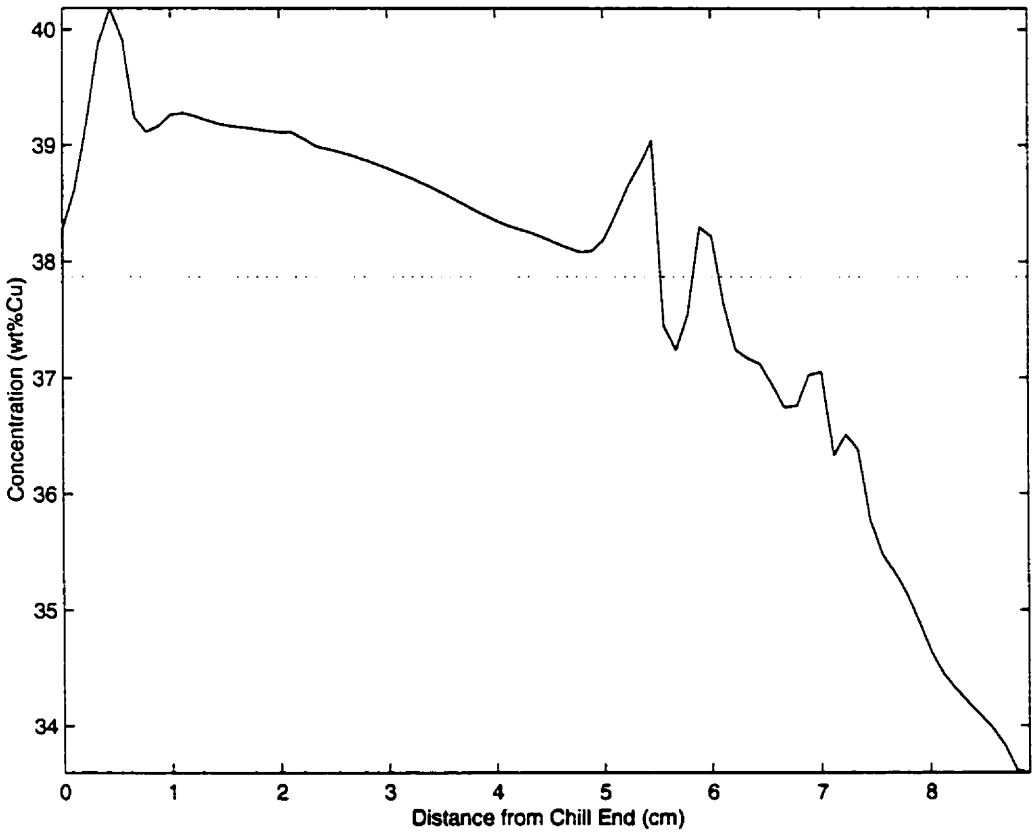

Figure C.2 Longitudinal segregation of the Al-38wt%Cu alloy solidified at R=11cm/hr.

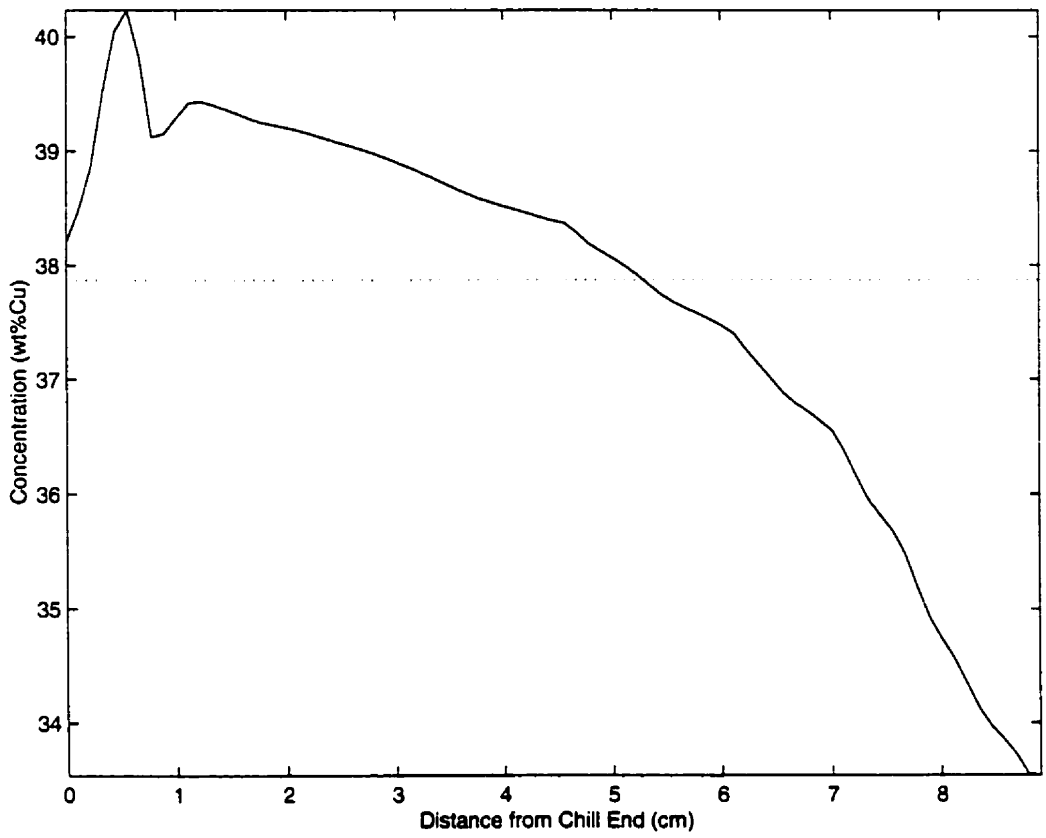

Figure C.3 Longitudinal segregation of the Al-38wt%Cu alloy solidified at R=12.46 cm/hr.

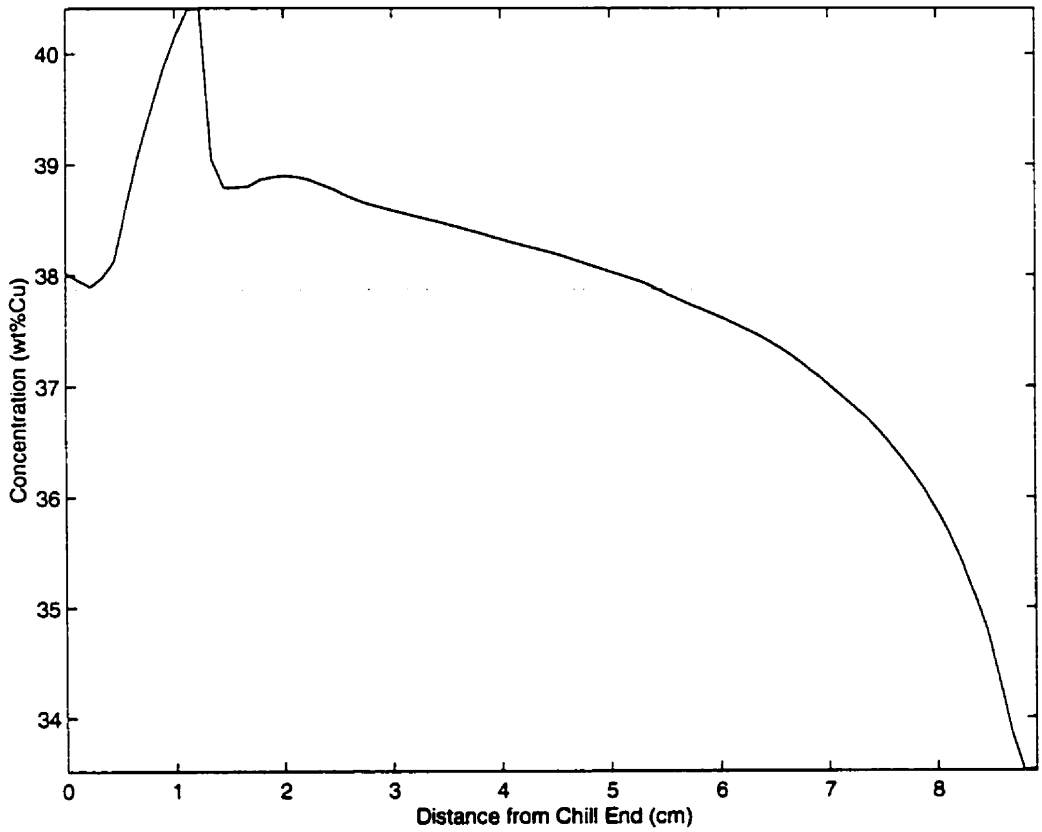

Figure C.4 Longitudinal segregation of the Al-38wt%Cu alloy solidified at R= 16.15 cm/hr.

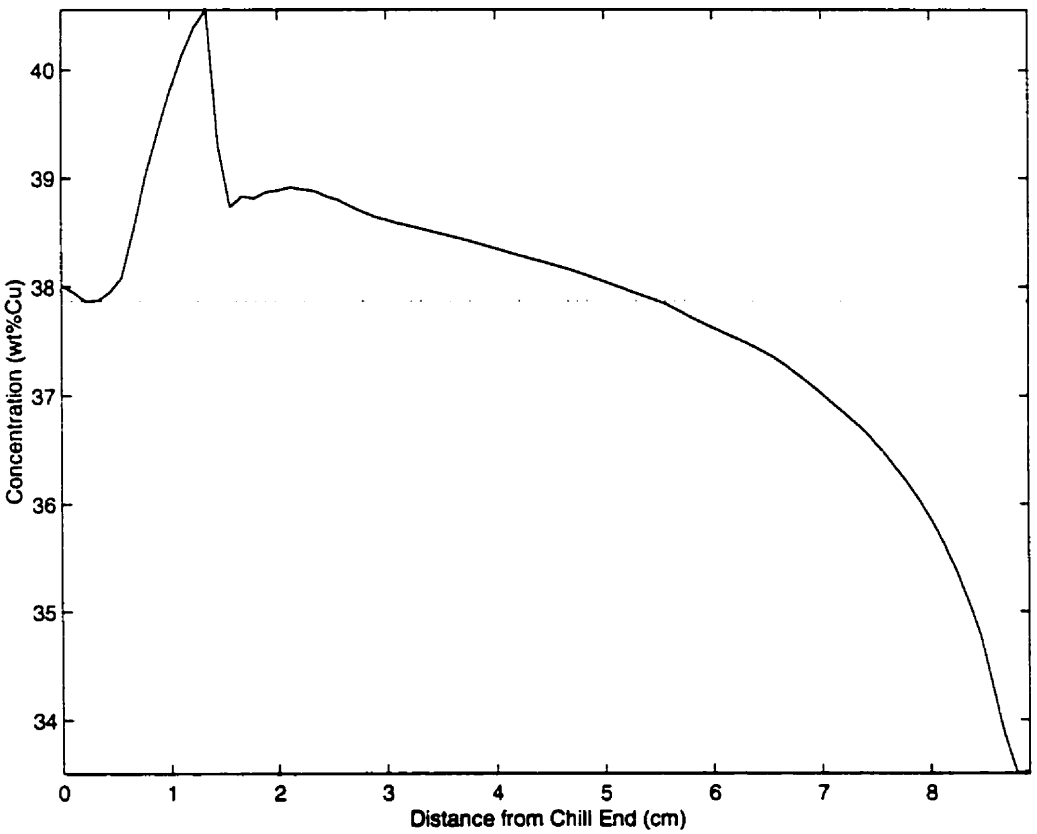

Figure C.5 Longitudinal segregation of the Al-38wt%Cu alloy solidified at R=16.28 cm/hr.

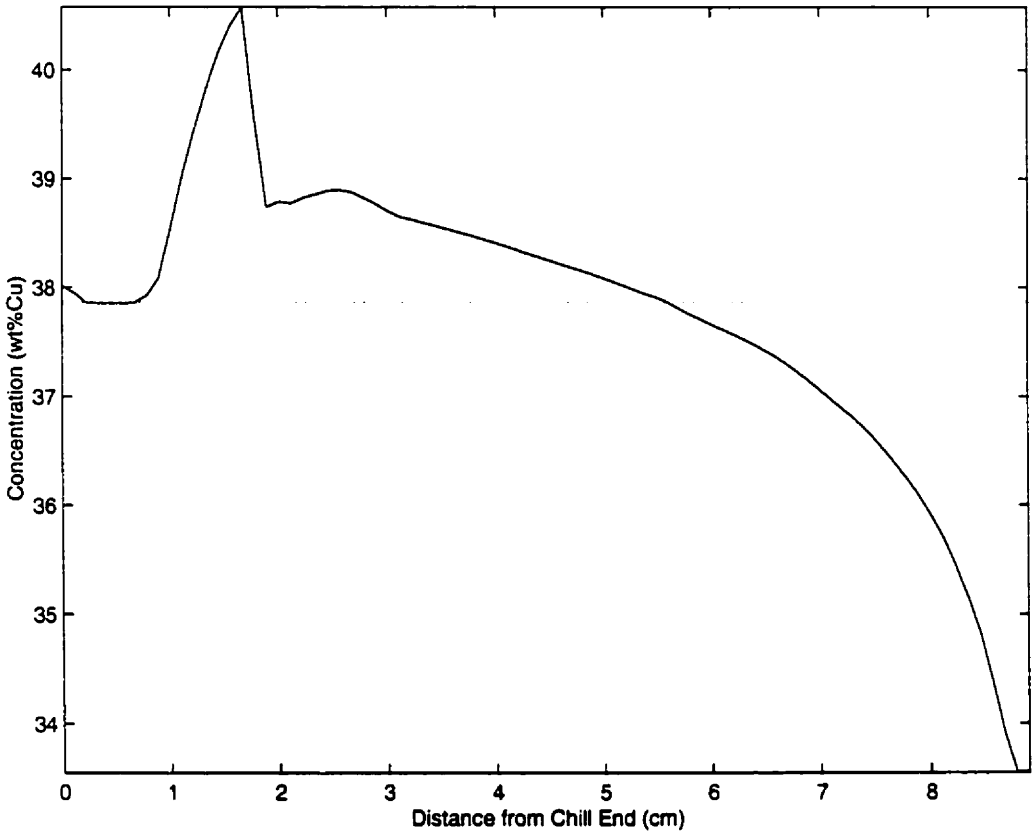

Figure C.6 Longitudinal segregation of the Al-38wt%Cu alloy solidified at R=16.34 cm/hr.

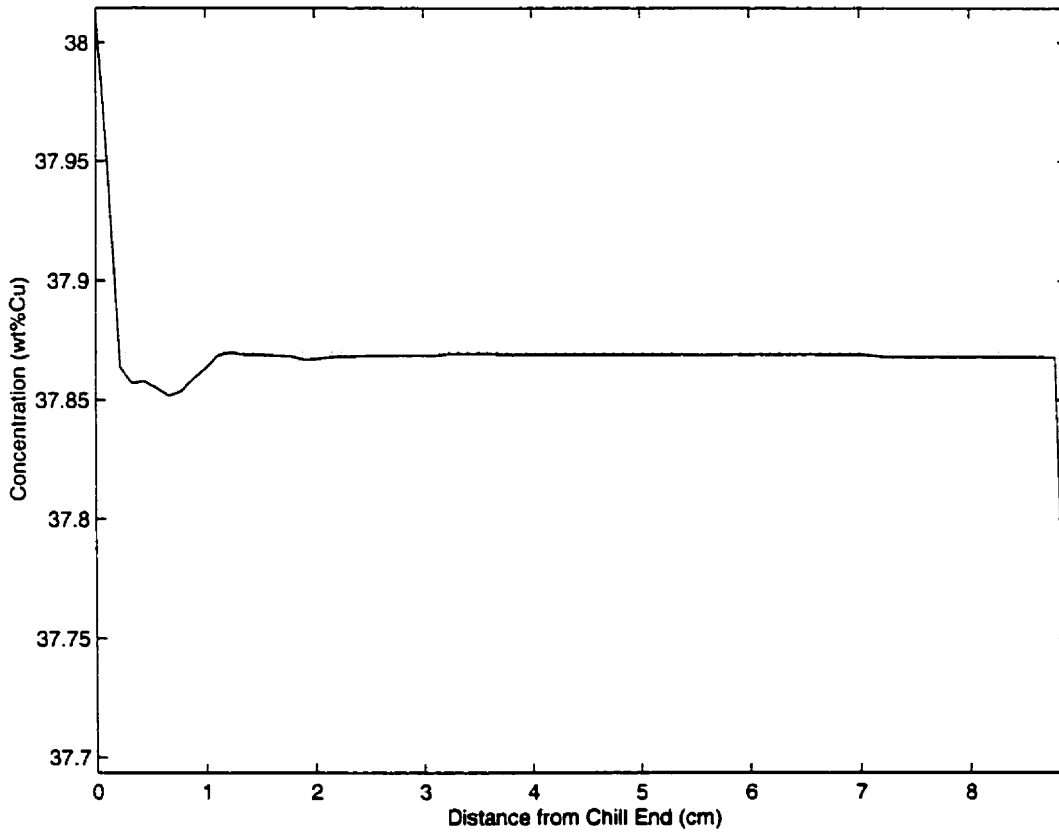

Figure C.7 Longitudinal segregation of the Al-38wt%Cu alloy solidified at R=16.41 cm/hr.

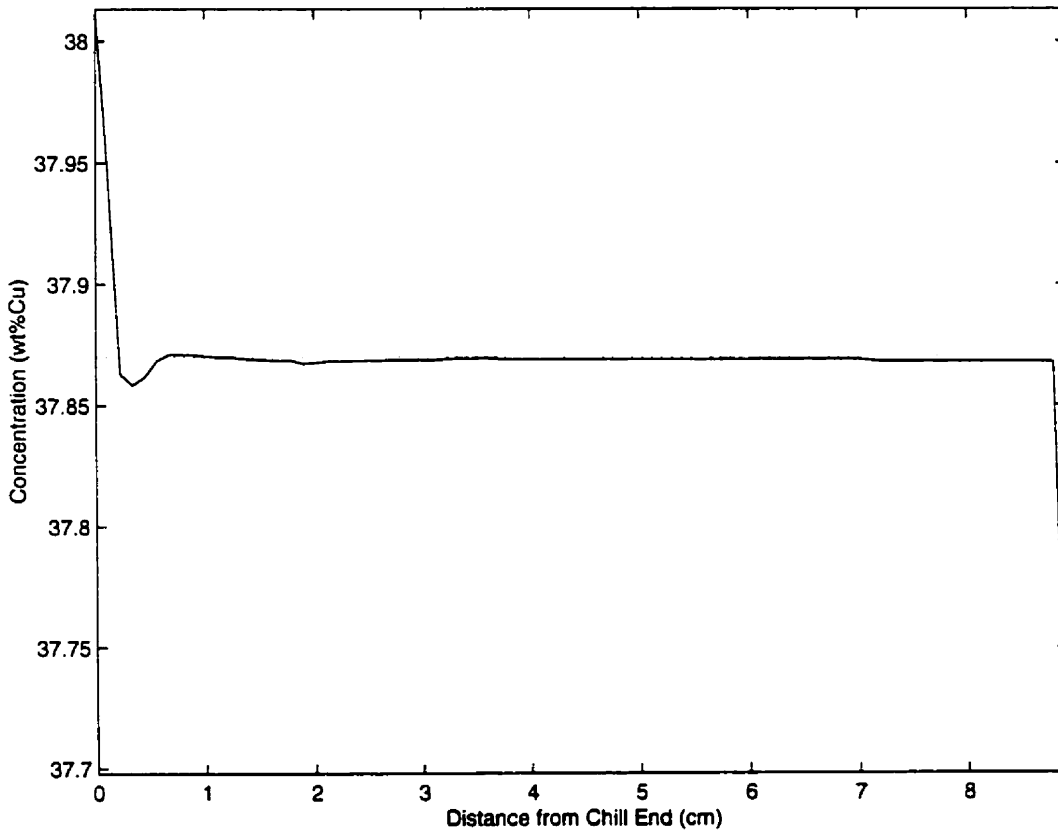

Figure C.8 Longitudinal segregation of the Al-38wt%Cu alloy solidified at R=16.6 cm/hr.

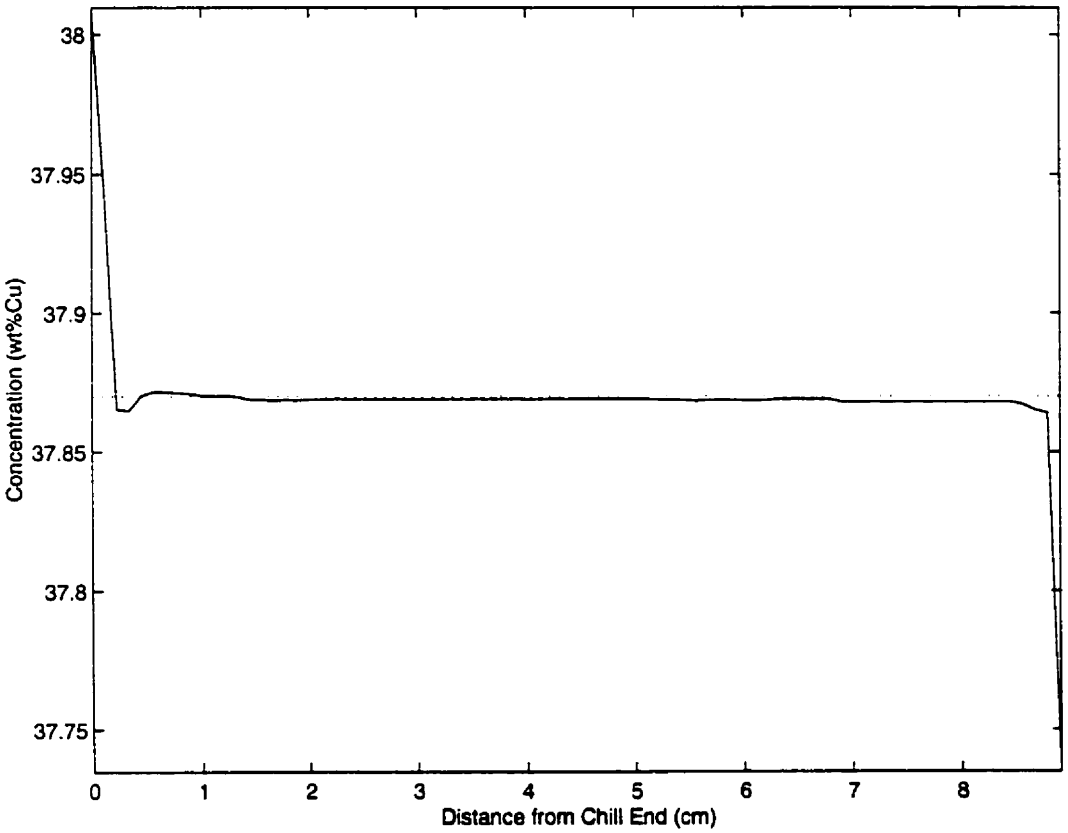

Figure C.9 Longitudinal segregation of the Al-38wt%Cu alloy solidified at R= 17.07 cm/hr.

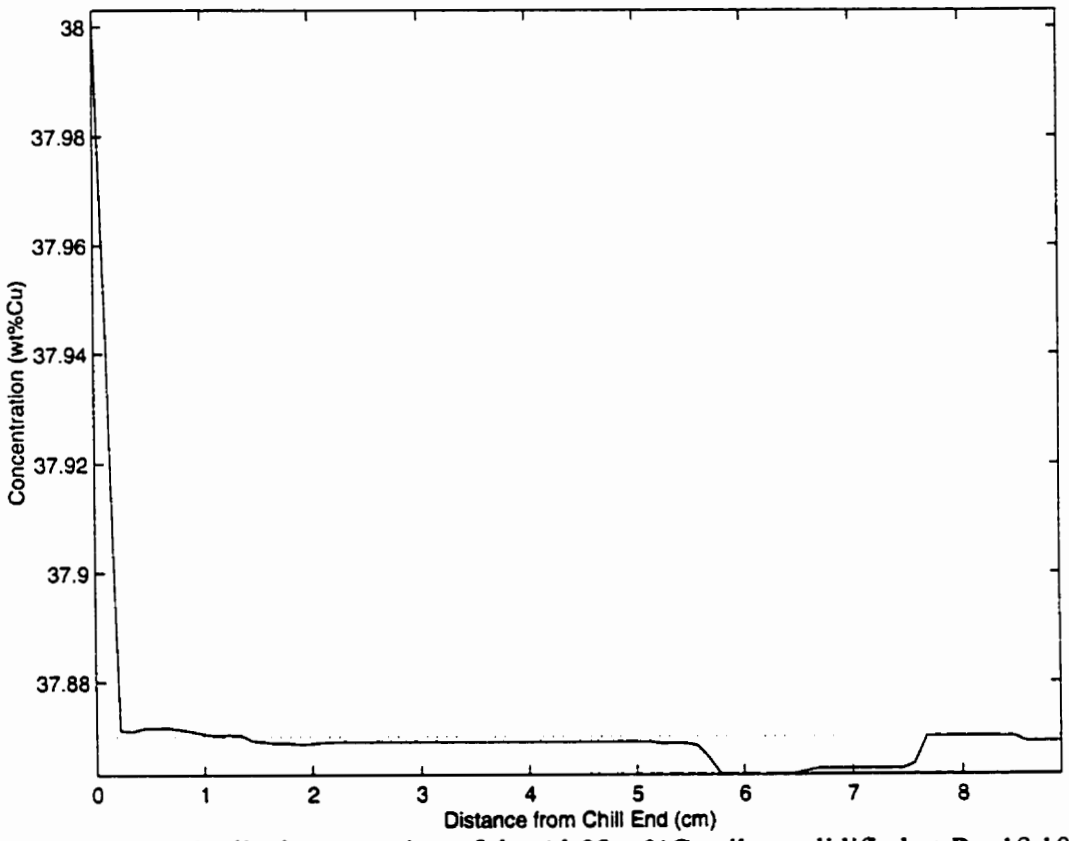

Figure C.10 Longitudinal segregation of the Al-38wt%Cu alloy solidified at R= 18.10 cm/hr.

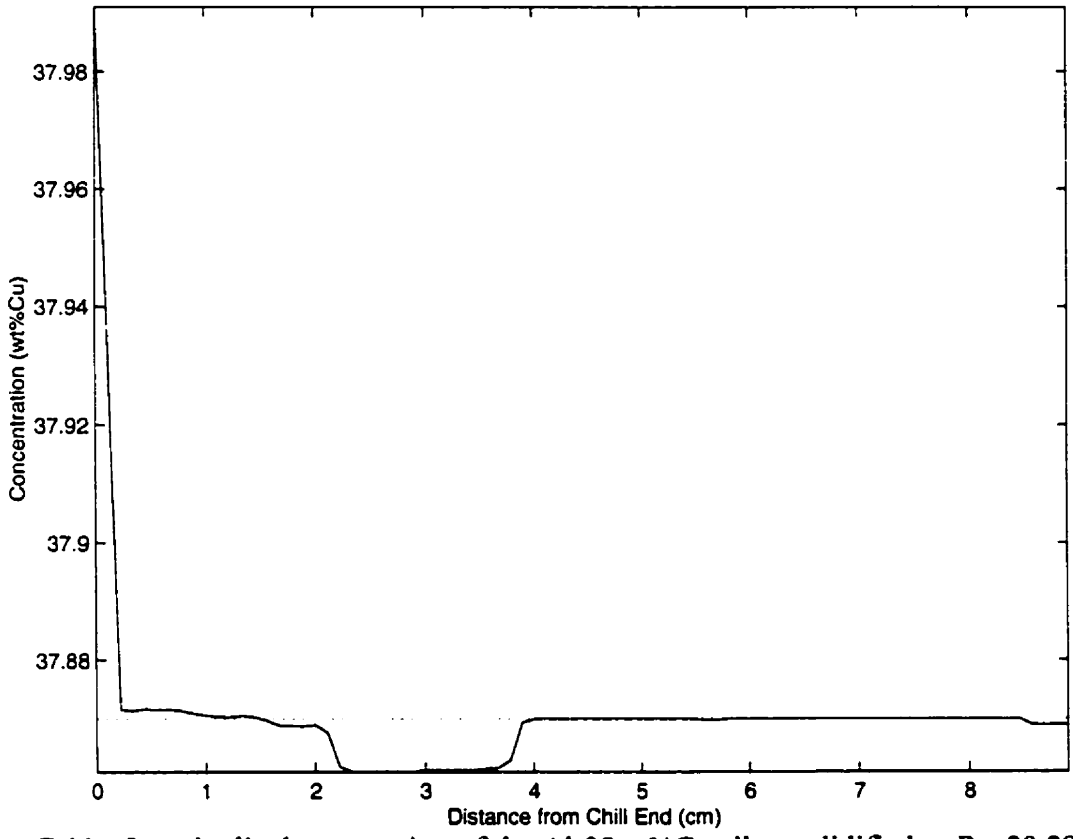

Figure C.11 Longitudinal segregation of the Al-38wt%Cu alloy solidified at R= 20.29 cm/hr.

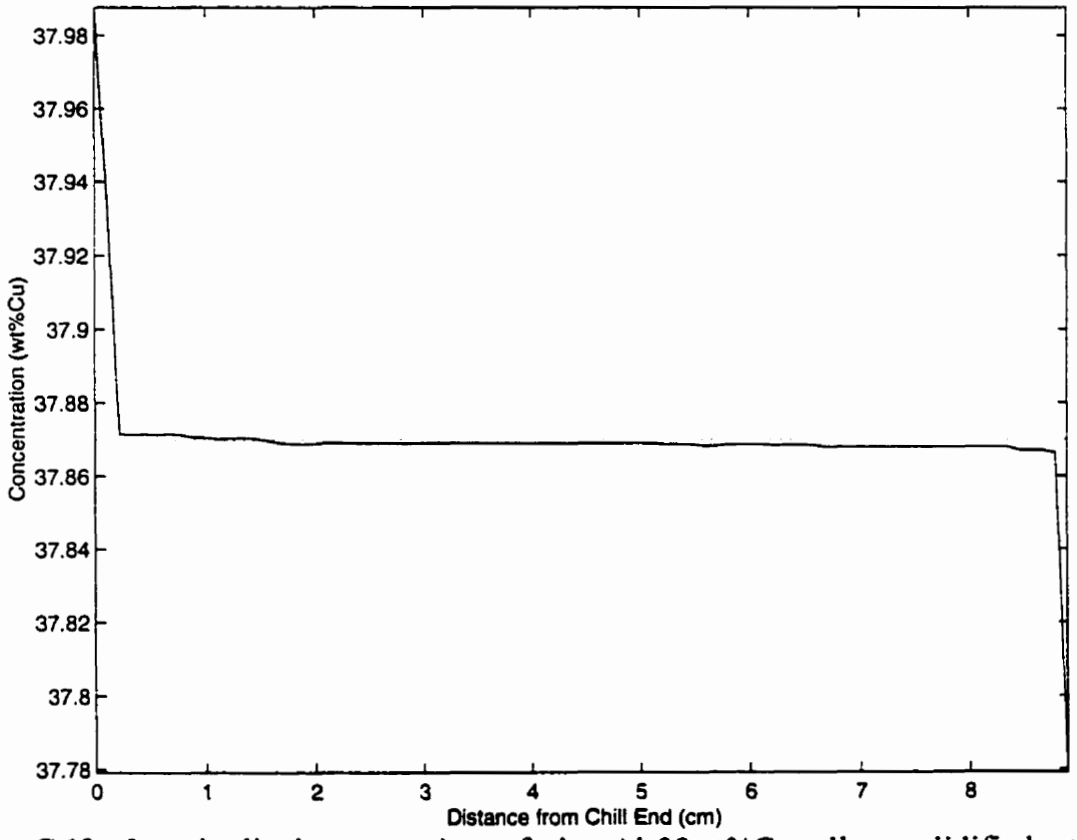

Figure C.12 Longitudinal segregation of the Al-38wt%Cu alloy solidified at R=21cm/hr.